THE ELASTIC SCATTERING OF DEUTERONS BY BERYLLIUM

Thesis by

James H. Renken

In Partial Fulfillment of the Requirements

For the Degree of

Doctor of Philosophy

California Institute of Technology

Pasadena, California

1963

ACKNOWLEDGMENTS

The author wishes to thank the staff and personnel of the Kellogg Radiation Laboratory for the advice and assistance which he received during the course of this investigation. He especially acknowledges his debt to Professor W. A. Fowler, who suggested this experiment, and Professor C. A. Barnes, whose suggestions and criticisms were instrumental in its successful completion. In addition, discussions with Dr. T. A. Tombrello have been of great benefit. The assistance of Mrs. Barbara Zimmerman in performing the computer calculations also is gratefully acknowledged.

The preparation of this thesis has been facilitated by the editing assistance of the author's wife Linda and his sister June Picciano.

Finally, the author wishes to acknowledge the receipt of fellowships from the Hughes Aircraft Company and the National Science Foundation which provided financial support during the course of his graduate training.

ABSTRACT

The differential cross section for the elastic scattering of deuterons by beryllium-9 has been measured for bombarding energies from 0.4 Mev to 1.8 Mev at the center-of-mass angles of 90°, $125^{\circ}16'$, and $163^{\circ}30'$. The cross sections were found to be slowly-increasing functions of the bombarding energy and are compatible with the assumption that the scattering nuclei may be represented by nearly-impenetrable charged spheres. No resonance structure was observed. These results are in disagreement with earlier observations of Be^{9} (d,d)Be^{9} scattering from which the existence of two levels in B^{11}, having excitation energies of 16.766 Mev and 16.912 Mev, respectively, was inferred. The results of this experiment indicate that the previously-observed elastic scattering anomalies were due to some shortcoming in the procedure of the earlier experiment.

TABLE OF CONTENTS

I. INTRODUCTION

The major task in low-energy experimental nuclear-structure physics is the determination of characteristic properties of the energy levels of various nuclei. These properties include the excitation energy, spin, isotopic spin, parity, lifetime, and branching ratios for various decay modes. One of the most fruitful techniques for studying these level parameters is the observation of various radiations from the nuclear system which follow charged-particle bombardment of an appropriate target. In particular, determining the number and angular distribution of elastically scattered projectiles often yields unambiguous values for many of the level parameters of interest.

Many compound-nucleus states resulting from the bombardment of light nuclei with protons or alpha particles have been studied by observing the elastically-scattered particles. Much less elastic scattering work has been done with deuterons as projectiles. There are perhaps three reasons: First, in contrast to the proton and alpha particle, the deuteron is a relatively weakly bound system with large spatial extent. What may be pictured classically as the noncoincidence of the deuteron's center-of-mass and center-of-charge produces a diffuse distribution of the deuteron's charge. Such a distribution, as well as any spatial polarization of it by the electric field of the scatterer, conceivably can have an observable effect on the scattering cross section. Second, because of the small binding energy of the deuteron, the compound systems formed by the target and projectile nuclei have relatively high excitation energies. Since the obvious course of action was to investigate low-lying states first, very little

incentive to use deuterons as scattering projectiles existed. Now as theoretical techniques attain more sophistication, it becomes desirable to investigate level parameters for states with high excitation energies. Third, the fact that the deuteron has unit spin somewhat complicates the analysis of experimental data. This is a practical difficulty and not a conceptual one. However, this difficulty places stringent limits on the permissible error in the experimental data and often requires that information about the associated reactions be available. A recently-completed measurement by Ford[1] of the Li^7 (d,d)Li^7 scattering cross section showed several broad anamolies. Unfortunately, the variation of the cross section with energy was sufficiently complicated to prevent the unambiguous determination of any level parameters.

Both direct-type reactions and the formation of B^{11} as a compound nucleus result from the bombardment of Be^9 by deuterons. (See Fig. 1 for the B^{11} energy level diagram.) For deuterons having energies between 0.400 Mev and 1.800 Mev, the excitation of the B^{11} nucleus will be between 16.15 Mev and 17.29 Mev. In this region, two levels, lying at 16.77 Mev and 16.93 Mev respectively, have been inferred primarily from anomalies in the deuteron elastic-scattering cross section.[2] In addition, the results of an investigation of the reaction Be^9(d,n)B^{10} indicated the presence of a level near 16.77 Mev.[3] A later investigation of this same reaction, however, indicated a smooth variation with energy of the neutron-production cross section, and, therefore, no resonant compound-nucleus states.[4]

Some information about other reactions induced by deuteron

bombardment of beryllium also exists. Unfortunately, the quantity and quality of these data make it impossible to say with certainty whether or not there are well-defined excited states at 16.77 Mev and 16.93 Mev in B^{11}.

An examination of the B^{11} level diagram will reveal that reactions of the types

$$Be^{9}(d,p)Be^{10}$$
$$Be^{9}(d,t)Be^{8}$$
$$Be^{9}(d,\alpha)Li^{7}$$
$$Be^{9}(d,n)B^{10}$$

are all energetically possible. Since the residual nuclei are left in various states of excitation, there are several groups of emerging particles for each type of reaction. There are, in fact, five positive-Q channels which yield neutrons and eight positive-Q channels which result in the emission of a charged particle other than a deuteron. The task of separating these various particle groups in order to measure the desired cross section is by no means trivial. As will be discussed later, the combination of a magnetic spectrometer and high-resolution solid-state detector provides a suitable means for distinguishing various reaction products.

Clearly, the experimental information concerning the two previously-mentioned excited states of B^{11} was unsatisfactory. This fact led to the investigation described in this thesis.

II. EXPERIMENTAL EQUIPMENT

1. General Description

The layout of the experimental equipment is shown schematically in Fig. 2. The beam of accelerated deuterons is provided by a 1.8 million-volt Van de Graaff generator.[5], [6] The beam of particles which emerges from the generator is a mixture of the ionic types H^+, D^+, HD^+, and DD^+. The magnetic field created by a crossfield magnet separates these beam components so that the unwanted ones may be stopped by a slit system. The desired beam component then enters a one-meter radius, 80-degree, electrostatic analyzer, the energy resolution of which is determined by the width of the entrance and exit slits. For this experiment, the slits were set so that the spread in energy of the transmitted particles, δE, gave an energy resolution, $E/\delta E$, of about 1200. Horizontal and vertical slits placed between the electrostatic analyzer and the target chamber provide additional collimation. Difference signals from these slits supply corrective information to systems which control the accelerating voltage and the current for the crossfield magnet.

After the incoming particles are scattered by the target, they are analyzed by a double-focusing magnetic spectrometer.[7] The arrangement of the target chamber and magnetic spectrometer is such that the particle beams entering and leaving the target chamber are inclined, respectively, 10 degrees above and below the horizontal plane. (See Fig. 3) This permits continuous rotation of the spectrometer about a vertical axis through nearly 180 degrees, thus providing laboratory scattering angles from 0 to 160 degrees. The magnetic

spectrometer analyzes particles according to their momenta, and the spread in momentum, δP, which the particles emerging from the spectrometer possess is determined by the width of the exit slit. For this experiment, an exit slit 0.125 inches wide produced a momentum resolution, $P/\delta P$, of 302.

A silicon p-n junction solid-state detector was used to count the analyzed particles.[8] The output of this detector was then processed by a charge-collecting preamplifier, amplifier, and appropriate counting circuits.

The amount of charge delivered to the target by the beam, and hence, the number of incident particles, is determined by a current integrator. This instrument collects a known amount of charge by using the beam current to discharge a capacitor which previously was charged to a known voltage. When this capacitor is completely discharged, a series of relays is activated which gates off the counting circuits, turns off a timer, and energizes a small magnet that deflects the beam off the target to minimize unnecessary deterioration of the target.

In order to insure that the current which discharges the capacitor is a true measure of the number of incident particles, two precautions are taken: First, the target is raised to a potential of 300 volts with respect to the walls of the target chamber. This minimizes the effect of secondary electrons emitted when the beam strikes the target. Second, a screen with a negative potential of 300 volts is placed at the entrance to the target chamber. This prevents electrons produced at the slits from reaching the target.

2. The Electrostatic Analyzer Energy Calibration

The energy of the particles which pass through the electrostatic analyzer is determined by the potential difference between its plates. If a particle having rest energy Mc^2 and charge Ze passes through the analyzer, then the kinetic energy of the particle is given to sufficient accuracy by

$$E_e = k_e Z V_e \left(1 + \frac{E_e}{2Mc^2}\right) \qquad (1)$$

where k_e is a constant and V_e is a certain fraction of the voltage across the analyzer plates. In practice V_e is measured with a potentiometer, and the particle energy is calculated using an appropriate value of k_e in Eq. (1).

The constant k_e is determined by observing the gamma rays from the 873-Kev resonance in the reaction $F^{19}(p,\alpha\gamma)O^{16}$. Assuming a resonance energy of 872.7 ± 0.4 Kev for the incident proton, Brown[9] measured k_e to be

$$k_e = 1.0047 \pm 0.0006 \text{ Mev/decivolt}$$

3. The Magnetic Spectrometer Energy Calibration

The momentum of a particle following a circular orbit in the presence of a magnetic field is proportional to the product of the magnetic induction and the orbital radius. The geometry of the spectrometer defines the radius; therefore the momentum of a particle passing through the instrument is proportional to the spectrometer magnetic field. The measurement of this magnetic field consists in balancing the torque that it produces on a small, current-carrying coil against the torsion produced in a quartz fiber to which the coil is attached. When

the coil is in the equilibrium position under the influence of opposing torques, an optical lever system provides error signals which regulate the field-producing current in the magnet.

Suppose the current passing through the small coil is determined by measuring the voltage drop V_m which it produces across a precision resistor. Then, the kinetic energy of a particle which has rest energy Mc^2, charge Ze, and passes through the spectrometer is given to sufficient accuracy by

$$E_m = \frac{k_m Z^2 M_p}{V_m^2 M} \left(1 - \frac{E_m}{2Mc^2} \right) \qquad (2)$$

where M_p is the proton rest mass and k_m is a constant of the spectrometer.

The value of k_m is determined as follows: Protons are scattered from a thick copper target prepared by evaporating the metal in a vacuum and allowing it to condense on a glass microscope slide. Fig. 4 shows a typical target "profile." This illustrates how the observed number of scattered particles varies as a function of V_m for a fixed incident-proton energy. The energy of the scattered particles can be calculated from the kinematics of the reaction. Then, by assuming that V_m at the midpoint of the profile rise corresponds to the energy of particles scattered from the surface layer of the target, Eq. (2) may be solved for k_m. The value of k_m determined from many measurements is

$$k_m = 381200 \pm 922 \text{ Mev} - mv^2$$

In order to relate the observed number of scattered particles and the differential scattering cross section, it is necessary to know the acceptance solid angle of the spectrometer. The discussion of

this solid angle will be postponed until the general procedure for determining the differential scattering cross section from the observed yield is considered.

4. The Semiconductor Detector

An important component of the apparatus used in this experiment was the junction silicon-diode detector, which was purchased from the Hughes Aircraft Company. Fig. 5 shows its essential features. The junction is formed by diffusing phosphorus into one side of a high resistivity p-type silicon wafer. By applying a reverse bias to the junction, a depletion, or space-charge, region is formed. The thicknesses X_p and X_n of the depletion regions in the two types of silicon depend on properties of the materials and the bias voltage; a typical value for X_p/X_n is 1000. The maximum electric field present in the depletion region is of the order of 10^4 volts/cm.

A particle to be detected strikes the n-type layer and penetrates into the depletion region. Here it creates hole-electron pairs that are promptly swept apart by the strong electric field which is present. This produces a current across the junction and results in a negative voltage pulse whose height is proportional to the energy of the incident particle. Optimum results in terms of linearity and resolution are obtained when the incident particle loses all of its energy in the depletion layer and the depth of this layer nearly equals the thickness of the silicon wafer.

A mount was fashioned which held the detector in place and acted as a spectrometer exit slit. Fig. 6 shows its general features.

III. EXPERIMENTAL PROCEDURE

1. The Determination of Cross Sections from Experimental Yields

The cross section for a nuclear reaction is defined to be

$$\sigma = \frac{Y}{n_d t} \tag{3}$$

where Y is the reaction yield per incident particle, n_d is the number of disintegrable target nuclei per unit volume, and t is the target thickness. Similarly, the differential cross section per unit solid angle in the laboratory system is defined to be

$$\left(\frac{d\sigma}{d\Omega}\right)_L = \frac{dY}{n_d t\, d\Omega} \tag{4}$$

where dY is the portion of the reaction yield per incident particle which is emitted into an element of solid angle $d\Omega$ at the laboratory angle Θ.

In the present experiment, deuterons were incident on a thick target and the magnetic spectrometer selected the particles scattered by a particular lamina within the target. The only symbol in Eq. (4) which cannot be easily identified with some experimental quantity is the effective target thickness t. In order to express this thickness in terms of suitable quantities, consider the nuclear reaction shown in Fig. 7. The energy of the incoming particle as it leaves the electrostatic analyzer is E_e. Because of the electron-suppression voltage on the target, the energy of this particle at the face of the target is $E_{1B} = E_e - Z_1 eV_T$. The existence of a contaminant layer on the surface can further degrade the particle energy, so the energy of the

particle at the surface of the reacting material is E_{10}.

At a certain normal depth s in the target, the incident particle with energy E_1 reacts. The emitted particle has energy E_2 and reaches the surface of the target with energy E_{20}; the contaminant layer further degrades the energy to E_{2R}. Finally, the energy of the particle which traverses the magnetic spectrometer is $E_m = E_{2R} + Z_2 eV_T$.

In practice, the electron-suppression voltage and thickness of the contaminant layer are kept small enough so that their effects on the particle energies are usually negligible. When these conditions exist, $E_e = E_{10} = E_{1B}$ and $E_m = E_{2R} = E_{20}$. This is assumed in what follows.

The directions of the incoming and outgoing particles relative to the target normal are specified by Θ_1 and Θ_2, respectively; these angles are related to the laboratory angle of observation by

$$\pi - \Theta = \Theta_1 + \Theta_2 \tag{5}$$

By considering the kinematics of a reaction with particle 1 incident on particle 0 and producing particles 2 and 3 and energy Q, it can be shown that

$$E_2 = \alpha(E_1, Q, \Theta)E_1 \tag{6}$$

where

$$\alpha^{\frac{1}{2}} = \frac{(m_1 m_2)^{\frac{1}{2}} \cos\Theta}{m_2+m_3} \pm \left[\frac{m_3 Q}{(m_2+m_3)E_1} + \frac{m_3-m_1}{(m_2+m_3)} + \frac{m_1 m_2 \cos^2\Theta}{(m_2+m_3)^2} \right]^{\frac{1}{2}} \tag{7}$$

We assume that the energy degradation which the particles suffer in moving through the target may be found from the expression

$$\frac{dE}{dx} = - n_s \epsilon(E) \tag{8}$$

where n_s is the density of stopping atoms and $\epsilon(E)$ is the atomic stopping cross section. For the case of a target having uniform composition, the variables in Eq. (8) may be separated and the result integrated to give

$$\int_{E_{1B}}^{E_1} \frac{dE}{n_s \epsilon_1(E)} = - \frac{s}{\cos \Theta_1} \tag{9a}$$

$$\int_{E_2}^{E_{20}} \frac{dE}{n_s \epsilon_2(E)} = - \frac{s}{\cos \Theta_2} \tag{9b}$$

where ϵ_1 and ϵ_2 apply to the incident and emitted particles respectively.

It can be seen from Fig. 7 that the thickness of the target layer along the direction of the incident beam is given by $t = \delta s/\cos \Theta_1$. We want to relate t to the spread in energy of the particles transmitted by the magnetic spectrometer; therefore in first approximation we have

$$\delta s = (\partial s/\partial E_{20}) \ \delta E_{20}$$

This gives

$$t = \left(\frac{\partial s}{\partial E_{20}}\right)_\Theta \frac{\delta E_{20}}{\cos \Theta_1} \tag{10}$$

for the relation between the target-lamina thickness and the acceptance-energy spread of the spectrometer.

We now differentiate Eqs. (9) with respect to E_{20} while holding Θ constant. This gives

$$\left(\frac{\partial s}{\partial E_{20}}\right)_{\Theta} = \frac{-\cos\Theta_1}{n_s\,\epsilon_1(E_1)}\left(\frac{\partial E_1}{\partial E_{20}}\right)_{\Theta} \tag{11}$$

and

$$\left(\frac{\partial s}{\partial E_{20}}\right)_{\Theta} = \frac{-\cos\Theta_2}{n_s}\left[\frac{1}{\epsilon_2(E_{20})} - \frac{1}{\epsilon_2(E_2)}\left(\frac{\partial E_2}{\partial E_{20}}\right)_{\Theta}\right] \tag{12}$$

Because of Eq. (6) we can write

$$\left(\frac{\partial E_2}{\partial E_{20}}\right)_{\Theta} = \left(\frac{\partial E_2}{\partial E_1}\right)_{\Theta}\left(\frac{\partial E_1}{\partial E_{20}}\right)_{\Theta} \tag{13}$$

By combining Eqs. (11), (12), and (13) we obtain

$$\left(\frac{\partial E_1}{\partial E_{20}}\right)_{\Theta} = \left[\frac{\epsilon_2(E_{20})}{\epsilon_2(E_2)}\left(\frac{\partial E_2}{\partial E_1}\right)_{\Theta} + \frac{\epsilon_2(E_{20})}{\epsilon_1(E_1)}\,\frac{\cos\Theta_1}{\cos\Theta_2}\right]^{-1} \tag{14}$$

Substituting this into Eq. (11) gives

$$\left(\frac{\partial s}{\partial E_{20}}\right)_{\Theta} = \frac{-\cos\Theta_1}{n_s\,\epsilon_2(E_{20})}\left[\frac{\cos\Theta_1}{\cos\Theta_2} + \frac{\epsilon_1(E_1)}{\epsilon_2(E_2)}\left(\frac{\partial E_2}{\partial E_1}\right)_{\Theta}\right]^{-1} \tag{15}$$

Using this in Eq. (10) yields

$$t = \frac{\delta E_{20}}{n_s\,\epsilon_2(E_{20})}\left[\frac{\cos\Theta_1}{\cos\Theta_2} + \frac{\epsilon_1(E_1)}{\epsilon_2(E_2)}\left(\frac{\partial E_2}{\partial E_1}\right)_{\Theta}\right]^{-1} \tag{16}$$

where the sign in Eq. (15) is unimportant and has been dropped.

We can now relate all the quantities in Eq. (4) to experimental observables. Let the difference between the number of detected particles at a point on the top of a thick-target profile and the number at the foot of the profile be called the resultant number of reaction products N_R. The total number of incident particles which produces

N_R is

$$N_i = \frac{CV}{Ze} \tag{17}$$

where C is the capacitance of the current-integrator condenser that is charged to voltage V and then discharged by the incident beam, and Ze is the charge on each incident particle. By definition

$$dY = \frac{N_R}{N_i} = \frac{Ze\ N_R}{CV} \tag{18}$$

The energy spread of the particles passed by the magnetic spectrometer is related to its resolution by

$$\frac{E_m}{\delta E_m} = \frac{1}{2}\ \frac{P}{\delta P} = \frac{1}{2} R \approx \frac{E_{20}}{\delta E_{20}} \tag{19}$$

According to theoretical predictions of the spectrometer performance, the resolution is determined by the width of the exit slit. The relation between these quantities is

$$R = 2(1 + m)\ \frac{r_o}{\delta r} \tag{20}$$

where m is the magnification, r_o the equilibrium radius, and δr is the width of the exit slit. Finally, if we identify the element of solid angle appearing in Eq. (4) with the acceptance solid angle of the spectrometer Ω_L, Eqs. (16), (18), and (19) may be combined to yield*

$$\left(\frac{d\sigma}{d\Omega}\right)_L = \frac{Ze\ N_R}{2V\ E_{20}}\ \frac{n_s}{n_d}\ \frac{R}{C\Omega_L}\ \epsilon_2(E_{20})\ \left[\frac{\cos\Theta_1}{\cos\Theta_2} + \frac{\epsilon_1(E_1)}{\epsilon_2(E_2)}\ \left(\frac{\partial E_2}{\partial E_1}\right)_\Theta\right] \tag{21}$$

To use Eq. (21), it is necessary to know the energies E_1 and E_2. If suitable stopping cross section data are available, in principle,

*This expression has been obtained by a procedure similar to that used by Bardin in reference 30 and agrees with what can be derived from his results.

these energies may be found by using Eqs. (6) and (9). For work in which cross sections are determined from yields measured near the target-profile rise (i.e., the reactions producing the yield occur in the lamina near the surface of the target), a useful approximation for E_1 may be derived from Eq. (14). For small s we assume $\epsilon_1(E_1) = \epsilon_1(E_{1B})$, $\epsilon_2(E_2) = \epsilon_2(E_{20})$, and $(\partial E_2/\partial E_1)$ remains constant. Then Eq. (14) may be integrated to give

$$E_1 = \frac{\dfrac{\epsilon_2(E_{20})\cos\Theta_1}{\epsilon_1(E_{1B})\cos\Theta_2}E_{1B} + E_{20} + \left(\dfrac{\partial E_1}{\partial E_2}\right)_\Theta E_{1B} - E_{2B}}{\left(\dfrac{\partial E_2}{\partial E_1}\right)_\Theta + \dfrac{\epsilon_2(E_{20})\cos\Theta_1}{\epsilon_1(E_{1B})\cos\Theta_2}} \tag{22}$$

where E_{2B} is the energy of a particle produced by a reaction at the surface of the target. This expression is identical with that obtained by Brown et.al.[10] Equation (7) shows that for elastic scattering reactions

$$\left(\frac{\partial E_2}{\partial E_1}\right)_\Theta = \alpha(\Theta) \tag{23}$$

This simplifies the use of Eqs. (21) and (22). Knowing E_1, E_2 may be found with Eq. (6).

In order to facilitate the examination of the scattering data, the well-understood variations of the cross section with energy and angle characteristic of Rutherford scattering were eliminated by dividing the measured cross sections by the appropriate Rutherford cross section. This cross section in the center-of-mass system is easily shown to be

$$\left(\frac{d\sigma}{d\Omega}\right)_C = 1.296 \left[\frac{Z_1 Z_0}{E_1}\left(\frac{M_0 + M_1}{M_0}\right)\csc^2\frac{\Theta_C}{2}\right]^2 \quad \frac{\text{millibarns}}{\text{steradian}} \qquad (24)$$

where E_1 expressed in Mev, is the laboratory energy of the incoming particle, Z_1 and M_1 are the charge number and mass of the incoming particle, and Z_0 and M_0 are the same quantities for the target.

Before comparing Eqs. (21) and (24), however, both cross sections must refer to the same coordinate system. To convert a laboratory cross section to the equivalent center-of-mass value, the former must be multiplied by

$$\frac{d\Omega_L}{d\Omega_C} = \frac{1 + X\cos\Theta_C}{\left(X^2 + 2X\cos\Theta_C + 1\right)^{3/2}} \qquad (25a)$$

$$= \frac{\left(1 - X^2\sin^2\Theta_L\right)^{\frac{1}{2}}}{\left[\left(1 - X^2\sin^2\Theta_L\right)^{\frac{1}{2}} + X\cos\Theta_L\right]^2} \qquad (25b)$$

where Θ_L and Θ_C are the laboratory and center-of-mass angles, respectively, and

$$X^2 = \frac{M_1 M_2}{M_0 M_3}\left[1 + \frac{(M_0 + M_1)}{M_0}\frac{Q}{E_1}\right]^{-1} \qquad (26)$$

The angles Θ_L and Θ_C are related by

$$\cot\Theta_L = \cot\Theta_C + X\csc\Theta_C \qquad (27a)$$

or

$$\sin(\Theta_C - \Theta_L) = X\sin\Theta_L \qquad (27b)$$

2. The Magnetic Spectrometer Acceptance Solid Angle

By using Eq. (21) it is possible to determine absolute cross sections providing that all quantities on the right-hand side can be measured. It would be possible to calculate a value of R using Eq. (20) and C could be measured; however the determination of Ω_L from the geometry of the spectrometer would be difficult.

Instead of attempting to determine Ω_L in this way, the following method was used. Protons were scattered from a copper target, and the scattering cross section was assumed to be Rutherford. Then the yield at the top of the resulting thick-target profile was used in Eq. (21) to calculate $R/C\Omega_L$. Using the nominal value of C and a value of R = 302 calculated with Eq. (20), the solid angle was found to be 1.47×10^{-3} steradians. This value was obtained from measurements performed at several energies and angles; Table I summarizes these measurements. The uncertainties listed are standard deviations calculated from repeated observations at each combination of energy and angle. This uncertainty does not include the effect of the uncertainty in the atomic stopping cross section of copper.

It may be argued that the cross sections calculated with Ω_L determined in the aforementioned fashion are not absolute. Strictly speaking this is true because the calculated cross sections are really expressed as a fraction of the Cu(p,p)Cu cross section. Obviously any difference between the true absolute cross sections for $Be^9(d,d)Be^9$ and the values quoted will depend on how much the Cu(p,p)Cu scattering deviates from the Rutherford law. The results in Table I lend confidence to the assumption of Rutherford scattering by copper.

3. The Scattering Target

The target used in this experiment was a small slab of beryllium whose dimensions were 1 1/2" × 1/4" × 1/16". The holder used for this target is illustrated in Fig. 8. The target is positioned in the target chamber by attaching the holder to the end of a rod which is coaxial with the center axis of the target chamber. By using O-ring seals, this rod is extended through the top of the target chamber so the vertical position and the angular orientation of the target may be varied at any time.

In addition to provision for holding the beryllium target, the target holder was built to hold a copper-on-glass target as well. By a simple vertical movement of the target rod, either the beryllium or copper target could be exposed to the beam.

Mozer[11] has shown that fine scratches on the surface of a scattering target can reduce the observed yield. Although his work indicates that fine scratches should not be important at the laboratory scattering angles used in this experiment, some effort was expended in trying to obtain a target whose surface was as mirror-like as possible.

Preliminary attempts to polish the target surface by rubbing it with fine grades of polishing paper and then iron-oxide rouge impregnated in a kerosene-soaked rag were unsatisfactory. This method not only removed scratches very slowly, but new scratches were created during the polishing process by single pieces of extraneous grit which became embedded in the rag.

It was finally decided to have the target polished by a commercial firm which specialized in polishing metallic surfaces. This

firm's method involved using a high-speed buffing wheel; the results were surprisingly good. A microscopic examination of the target surface did reveal a series of tiny parallel scratches. However, as suggested by Mozer's work, the effect of these scratches was minimized by holding the target during polishing so that the scratches would be approximately in the scattering plane when the target was positioned in the target chamber.

Once the target surface was prepared, the deposits of carbon contaminant which built up on the surface of the target during bombardment were periodically removed by lightly rubbing it with a rag containing iron-oxide rouge. After each such polishing, the target was successively washed with kerosene, acetone, and distilled water.

A target profile was taken to check the cleanliness of the target surface and to see if any impurities were present within the target. This is shown in Fig. 9. By kinematics the two peaks in front of the beryllium elastic-scattering yield can be attributed to elastic scattering by layers of carbon atoms and oxygen atoms, respectively, on the surface of the target. The small, symmetrical peak at $V_m = 580$ is due to a very thin surface layer of some scatterer having a mass number of about 100. The constant background plateau which begins at $V_m = 592$ is probably due to the presence of some impurity distributed within the target. Judging from the value of V_m where this background begins, it seems likely that this impurity is either iron, cobalt or nickel. The background yield indicates that the ratio of the number of beryllium atoms to the number of impurity atoms is 2200:1. Such an impurity concentration results in an effective stopping cross section

for the target which differs from that of pure beryllium by less than one-third of one percent.

4. Data-Taking Procedure

(a) Separation of the Reaction Products

The number of possible breakup channels available to the Be^9 + d system is large. Consequently the detection of elastically-scattered deuterons was complicated by the presence of protons, tritons, and singly- and doubly-charged alpha particles which were produced by the competing reactions. The magnetic spectrometer alone could not discriminate these different particle groups because the reaction products from the many layers in a thick target had a continuum of momenta. Although the singly-charged particles transmitted by the magnetic spectrometer all had the same momentum, it is easy to show that their energies were not equal. If the energy of the protons transmitted by the spectrometer is taken as the unit, then the energies of the other particles transmitted at the same spectrometer setting are given by

$$E_d = 1/2\ E_p$$
$$E_t = 1/3\ E_p$$
$$E_{\alpha+} = 1/4\ E_p$$
$$E_{\alpha++} = E_p$$

where the subscript meanings are obvious. Thus the use of a detector possessing good energy-resolving properties provided the necessary means for distinguishing the various particles which passed through the spectrometer.

The p-n junction detector used in this experiment has an energy

resolution of about 10 percent in the energy range where it was used. As can be seen from Fig. 10, this detector afforded the necessary separation between different particle groups. During the experiment the number of elastically-scattered deuterons was determined by setting the window of a single-channel pulse-height analyzer so that the deuteron pulses would be passed while the others would not.

As the energy of the incident deuterons was lowered, the height of the detector pulses produced by the scattered particles also decreased. Finally the output-pulse height became comparable to the level of the electronics noise. When this condition existed, the entire detector-output spectrum was recorded by using a multichannel analyzer. Typical spectra obtained with this instrument are shown in Figs. 11 and 12. With records such as these, any necessary noise subtractions could be made and the yield of scattered deuterons obtained by summing the number of counts in the appropriate analyzer channels.

It was necessary to be certain that the particle group being observed really was the elastically-scattered deuterons. This was verified in two ways: First, the observed positions of the scattering-profile rises agreed with the positions calculated from kinematics. Second, the observed pulse height for deuterons from Cu(d,d)Cu (there being no question here that the observed particles were deuterons because of the intensity of the scattered particles) was compared with the pulse height of the particles thought to be deuterons from $Be^9(d,d)Be^9$. The ratio of these observed pulse heights agreed with the calculated ratio of deuteron energies for the two scattering processes. Thus there can be little doubt that the observed particles

were really deuterons.

(b) The Determination of N_R

Values of N_R corresponding to various incident energies and scattering angles may be obtained from the appropriate scattering yield profiles. Figs. 13 to 20 show some typical profiles obtained under the noted conditions.

It is unnecessary to obtain a complete profile at each point where the cross section is to be measured. Since N_R is determined from the difference in number of counts before and after the profile rise, it is sufficient to measure the number of counts at these two positions without being concerned with the detailed shape of the profile.

The data-taking procedure consisted of the following: The number of scattered particles was determined for two values of V_m on the profile rise. This verified the location of the rise. Then V_m was increased to a value corresponding to the peak of the profile and the number of scattered particles was noted. The scattering yield was again recorded after making one or two additional small increases in V_m; the scattering energy E_1 was determined from the average of the values of V_m for which yields at the profile peak were measured. This permitted verification that the yield was being measured at the profile peak and provided several yield measurements which could be averaged. Finally, V_m was set at a value below the profile rise and the background yield was measured.

5. Corrections to the Experimental Yields

(a) Charge Neutralization

When a scattered particle emerges from a solid target, its effective charge, which depends upon the number of electrons attached

to it, may, in general, be one of several values. The magnetic spectrometer can pass only the particles of interest with a particular effective charge. To correct the yield for the particles of interest which have other effective charges, the fraction of the emerging particles in each charge state must be known. These fractions, or charge equilibrium ratios, have been measured by Phillips[12] and found to depend upon the energy of the particle and the type of atoms in the last few atomic layers at the surface of the solid. The results quoted by Phillips are directly applicable to cases where the emerging particles are protons. By making the assumption that the probability of electron attachment to a moving ion is only a function of the ion's velocity and the number of other electrons already attached to it, it is easy to show that an emergent beam of deuterons with energy E will have the same charge equilibrium ratios as a beam of protons with energy 1/2 E.

Phillips' experimental apparatus was such that he was able to maintain the cleanliness of the surface from which the ions emerged. This enabled him to detect small differences in the charge equilibrium ratios for particles emerging from different surfaces. The charge-equilibrium-ratio measurements which seem most consistent with the conditions in this scattering experiment are those for a surface which Phillips called "dirt." For this measurement Phillips did nothing to overcome the buildup of foreign matter on the surface from which the ion beam emerged. Although it is uncertain that Phillips' "dirt" and the surface contaminant present in this experiment had the same composition, such an assumption seems more reasonable than that the charge equilibrium ratios were determined by a clean beryllium surface.

The fraction of the total number of deuterons which emerges

from a "dirt" surface as singly-charged ions is shown in Fig. 21. Several points at the high-energy end of this curve are from Mozer's work.[11] He obtained these data by assuming the measured cross section for Cu(p,p)Cu deviated from the Rutherford value at low energies because of a reduction in the observed yield due to the formation of neutral and negatively-charged ions at the target surface. For comparison, Fig. 21 also shows the fraction of singly-charged deuterons emerging from a clean beryllium surface. Since the magnetic spectrometer was set to pass singly-charged deuterons, Fig. 21 provides correction factors for eliminating the effect of electron attachment.

(b) Scaler Dead Time

Because of the finite amount of time required for the detection equipment to process the signal generated by each detected particle, the equipment is "dead" during a certain fraction of the counting period. This gives an observed yield which is less than the true yield. A correction to the observed yield for the equipment dead time may be derived in the following way: The fraction of the counting period for which the counting equipment is dead is given by $N\tau/t$ where N is the number of counts observed during a period t and τ is the dead time per count; the number of potential counts available during this dead period is $N\tau M/t$ where M is the true number of counts appropriate for the period t. Thus M must be given by $M = N + (N\tau/t)M$ or

$$M = \frac{N}{1 - N\tau/t} \approx N(1 + N\tau/t) \qquad (28)$$

A convenient form for expressing the magnitude of this correction is

$$\frac{\Delta M}{M} = \frac{M - N}{M} \approx \frac{N\tau}{t} \qquad (29)$$

Using a value of $\tau = 10^{-5}$ seconds as characteristic of the scalers employed to count the number of detected particles, the $Be^9(d,d)Be^9$ counting rates were such that $\Delta M/M$ was never greater than 0.3 percent. For these data the dead time was neglected. When it was necessary to record the scattering data with a multichannel analyzer, the percentage of dead time was calculated to be of the order of one percent. The most important dead-time corrections were made to the Cu(p,p)Cu yield data taken for the solid-angle calibration. Corrections in this case were typically between one and three percent.

(c) Scattering by the Detector Dead Layer

It is conceivable that the number of particles observed by the p-n junction detector could be less than the number incident on its face because of backscattering by the dead layer. Communication with the manufacturer of the detector revealed that the dead layer could have a thickness as large as 0.5 microns. A layer of this thickness is consistent with the observed difference between the pulse heights produced by equally-energetic protons and alpha particles as shown in Fig. 10. To check the effect of this scattering, a calculation was made of the number of 200-Kev deuterons which would be lost by Rutherford scattering from an 0.5 micron layer of silicon. For these conditions it was found that the number of detected particles is lowered only 0.07 percent by dead-layer scattering. This loss is smaller at higher energies and thus is completely negligible.

6. Some Effects Causing Deviation from Rutherford Scattering

As mentioned earlier, the interpretation of the observed scattering cross sections was facilitated by first removing the variation attributable to the ordinary Coulomb interaction. The possibility did remain that other well-understood, although more subtle, effects might be influencing the experimental scattering. The following describes two such effects.

(a) Screening by Atomic Electrons

A calculation by Wenzel[13] shows that the screening of the target nucleus by its electron cloud will lower the scattering cross section from the Rutherford value according to

$$\frac{d\sigma}{d\sigma_R} = 1 - \frac{\Delta}{E} \qquad (30)$$

where E is the center-of-mass energy of the incident particle and Δ is the absolute value of the potential at the nucleus due to the electron cloud. Foldy[14] has shown that Δ is well-represented by

$$\Delta = 34(Z_o)^{7/5} \text{ ev}$$

where Z_o is the atomic number of the nucleus.

This screening effect was negligible for the $Be^9(d,d)Be^9$ scattering. However, the cross sections measured for Cu(p,p)Cu to be used in determining the solid angle were altered by a small amount. The maximum correction to these data for screening was about 0.7 percent.

(b) Effects Resulting from the Structure of the Deuteron

The effect on the elastic scattering caused by the finite separation between the deuteron's instantaneous center-of-mass and center-of-charge has been investigated theoretically by French and Goldberger[15]. A computer program to evaluate their expression for the change in the cross section was written in this laboratory. A calculation using this program indicated that the scattering due to the Coulomb force should slowly fall below Rutherford as the incident energy is increased. However, at the highest energy used in this experiment, the predicted deviation from Rutherford was slightly less than two percent.

A second effect which can influence the Coulomb-interaction scattering is the induction of an electric dipole moment in the deuteron by the electric field of the scatterer. A Born-approximation estimate of the magnitude of this effect has been made by Morinigo[16]. This work indicates that the fractional deviation of the cross section from the Rutherford value should be roughly proportional to the polarizability and the momentum transferred from the incident particle to the scattering potential during the collision. Using a reasonable estimate of the deuteron polarizability, the predicted cross section for backward scattering of one-Mev deuterons is about two percent less than the Rutherford value.

7. The Atomic Stopping Cross Section

The variation of the atomic stopping cross section for protons passing through beryllium is given by Mozer[11]. In general the stopping cross section for a light particle in a given material is

related to that of a proton in the same material by

$$\epsilon_i(E) = \left(\frac{Z_i}{Z_p}\right)^2 \epsilon_p\left(\frac{M_p}{M_i} E\right) \qquad (31)$$

Thus the necessary values of the stopping cross section for deuterons in beryllium were obtained by using $\epsilon_d(E) = \epsilon_p(1/2\ E)$. This relation is considered to be accurate to within two percent.[17]

8. Results of the Cross Section Measurements

The results for this measurement of the $Be^9(d,d)Be^9$ elastic-scattering cross section are shown in Fig. 22. These data are expressed as the ratio of the observed cross section to the corresponding point-charge Rutherford cross section. For measurements made at the center-of-mass angles of 90° and $125^\circ 16'$, the maximum particle energy which the magnetic spectrometer could analyze fixed the upper limits for the bombarding energies.

9. Analysis of the Experimental Error

(a) Relative Uncertainty in $d\sigma/d\sigma_R$

The possible error in the quoted values of $d\sigma/d\sigma_R$ for $Be^9(d,d)Be^9$ scattering can be determined from the uncertainties in the experimental quantities from which this ratio is calculated. To determine the relative fractional standard deviation for $d\sigma/d\sigma_R$ the quantities whose uncertainties must be considered are

$$\frac{d\sigma}{d\sigma_R} \propto \frac{N_R}{V} \frac{\epsilon(E_{20})}{E_{20}} \left[\frac{\cos\Theta_1}{\cos\Theta_2} + \alpha \frac{\epsilon(E_1)}{\epsilon(E_2)}\right] E_1^2$$

where the symbols have their previously-defined meanings.

The reasons for the uncertainties in these terms are the following:

N_R: The error in this term results from the background subtraction and the inevitable statistical counting error.

$\epsilon(E)$: The stopping cross sections are assumed to have a relative fractional standard deviation of two percent.

$\cos \Theta_1/\cos \Theta_2 + \alpha [\epsilon(E_1)/\epsilon(E_2)]$: The errors in α and $\cos \Theta_1/\cos \Theta_2$ due to random errors in the various angle settings are very small compared with the error in the stopping cross section ratio. Thus the main source of error in this term is the uncertainty in the stopping cross sections.

E_{20} and E_1: The errors in these terms are due to the uncertainties in the appropriate calibration constants.

V: The uncertainty in this term results from fluctuations in the charging voltage for the condenser which is discharged by the beam current.

The relative fractional standard deviations for these sources of error are shown in Table II. Assuming these errors to be independent and normally distributed, their combined effect gives a relative fractional standard deviation for $d\sigma/d\sigma_R$ of about 2.9 percent.

At the lowest values of E_{20}, an additional source of uncertainty in N_R is the noise subtraction procedure. It is assumed that the greatest uncertainty due to this procedure is eight percent. It is further assumed that the charge equilibrium ratio makes no contribution to the relative uncertainty in $d\sigma/d\sigma_R$.

(b) Absolute Uncertainty in $d\sigma/d\sigma_R$

The values of $d\sigma/d\sigma_R$ measured in this experiment were normalized on the absolute scale by using the observed yield from Cu(p,p)Cu scattering. Thus the absolute uncertainty in $d\sigma/d\sigma_R$ is due to the uncertainties in the quantities

$$\frac{d\sigma}{d\sigma_R} \propto \frac{N_R^b}{N_R^c} \frac{V^c}{V^b} \frac{E_{20}^c}{E_{20}^b} \frac{\epsilon^b(E_{20})}{\epsilon^c(E_{20})} \frac{\left[\frac{\cos\Theta_1^b}{\cos\Theta_2^b} + \alpha^b \frac{\epsilon^b(E_1)}{\epsilon^b(E_2)}\right]}{\left[\frac{\cos\Theta_1^c}{\cos\Theta_2^c} + \alpha^c \frac{\epsilon^c(E_1)}{\epsilon^c(E_2)}\right]} \frac{(E_1^b)^2}{(E_1^c)^2} \left(\frac{\sin\frac{\Theta_C^b}{2}}{\sin\frac{\Theta_C^c}{2}}\right)^4$$

where the superscripts b and c signify that the particular quantity is determined for $Be^9(d,d)Be^9$ or Cu(p,p)Cu scattering respectively.

The error analysis based on the quantities shown above is complicated by the possibility of a systematic error in the angular settings of the magnetic spectrometer. As discussed by Ford[1], the protractor used to orient the spectrometer seems to be misaligned by about two-thirds of a degree. Although the angular settings used in this experiment were corrected by this amount, the possibility that a systematic error in the angle still exists cannot be overlooked. A systematic error of one-half of a degree would dominate any random error in the angle settings. For such a situation the errors in the square-bracket and $\sin\frac{1}{2}\Theta_C$ terms are not independent, and the usual technique for combining independent, normally-distributed errors in order to determine the probable error in an experimental result is not rigorously valid.

The effect on the experimental uncertainty due to a possible

systematic error in angle was investigated by finding the greatest possible error in $a = \cos \Theta_1 / \cos \Theta_2$ which could result from an error μ in the laboratory scattering angle. When the experimental procedure is to set Θ_1 as nearly equal to Θ_2 as possible, it can be shown that a fractional error $\delta a/a = \mu \cot(\frac{1}{2}\Theta_L)$ can result. Using this fact, the error arising from the two square brackets was calculated in two different ways: First, it was assumed that $\delta a/a$ could be treated as the fractional standard deviation σ_a/a and the error in the ratio of the square brackets was calculated as due to a term of the form $\Psi = (a+f)/(b+g)$ where a, b, f, and g are independent quantities. Second, as an attempt to assess the importance of the interdependence of the errors in $\cos \Theta_1^b / \cos \Theta_2^b$ and $\cos \Theta_1^c / \cos \Theta_2^c$, the error in the ratio of the square brackets was calculated as due to a term of the form $\Psi = (a+f)/(a+g)$ where a, f, and g are independent quantities. These two assumptions yielded approximately the same result for the fractional error resulting from the ratio of the square brackets. This suggested that the uncertainty in this ratio is only slightly dependent on the errors in the angle settings.

The third angle-dependent term which contributes to the uncertainty is $X = (\sin \frac{1}{2}\Theta_C^b / \sin \frac{1}{2}\Theta_C^c)^4$. If both center-of-mass angles have a systematic error ν, then the fractional error due to this term is $\delta X/X = 2\nu (\cot \frac{1}{2}\Theta_C^b - \cot \frac{1}{2}\Theta_C^c)$. Although there is no justification for combining this systematic error with the random errors in the other quantities, its relatively small size suggests that $\delta X/X$ can be treated as random without invalidating the estimate of the fractional standard deviation for $d\sigma/d\sigma_R$.

The uncertainties in the various terms which contribute to the absolute fractional standard deviation in $d\sigma/d\sigma_R$ are shown in Table II. The uncertainties in the angle-dependent terms were assumed to result from a one-half degree systematic error in the angular settings. The combined effect of these uncertainties gives an absolute fractional standard deviation for $d\sigma/d\sigma_R$ of about 6.7 percent.

At the lowest values of E_{20}, two additional sources of uncertainty are present. These are the uncertainty in the charge equilibrium ratio and the uncertainty in N_R^b resulting from the noise subtraction procedure.

IV. COMPARISON OF THE OBSERVED CROSS SECTIONS WITH THE SCATTERING DUE TO A CHARGED SPHERE

The most striking feature of the excitation functions shown in Fig. 22 is the lack of any pronounced variation of the ratio-to-Rutherford with energy. This suggests that the mechanism primarily responsible for the scattering is only slightly dependent upon the detailed internal structure of the interacting nuclei. The additional fact that the observed values of $d\sigma/d\sigma_R$ are approximately unity indicates that the Coulomb interaction is the dominant scattering mechanism. Since the values of $d\sigma/d\sigma_R$ do deviate from unity, however, some interaction in addition to the pure Coulomb field is present; a logical choice for the source of this additional interaction is the finite size of the nuclei.

1. Scattering by an Impenetrable Charged Sphere

The first attempt to calculate scattering cross sections which agreed with the experimental values was made after assuming the scattering nucleus was an impenetrable charged sphere. In this case, results of Blatt and Biedenharn[18] can be used to find that the ratio-to-Rutherford for the predicted cross section is given by

$$\frac{d\sigma}{d\sigma_R} = 1 - \frac{2}{kz}\sin^2\left(\frac{\Theta}{2}\right)\sum_{\ell=0}^{\infty}(2\ell+1)\sin\Phi_\ell\cos\left[2\eta\ \ell n\sin\left(\frac{\Theta}{2}\right)+2\Psi_\ell+\Phi_\ell\right]P_\ell(\cos\Theta)$$

$$+\frac{\sin^4\left(\frac{\Theta}{2}\right)}{k^2z^2}\sum_{L=0}^{\infty}\sum_{\ell=0}^{\infty}\sum_{\ell'=|\ell-L|}^{\ell+L}(2\ell+1)(2\ell'+1)\left[(\ell\ell'00\,|\,\ell\ell'L0)\right]^2\times$$

$$\sin\Phi_\ell\sin\Phi_{\ell'}\cos\left[(2\Psi_\ell+\Phi_\ell)-(2\Psi_{\ell'}+\Phi_{\ell'})\right]P_L(\cos\Theta) \qquad (32)$$

*It is assumed here and in what follows that the amplitudes of the various scattered partial waves depend only on the ℓ-values of the respective waves.

where Θ is the center-of-mass scattering angle and $(\ell\ell'00|\ell\ell'L0)$ is a Clebsch-Gordan coefficient. Other symbols in this expression are defined by the following:

$$\eta = \frac{Z_1 Z_0 e^2}{\hbar v} \tag{33}$$

where v is the relative velocity of the two particles;

$$z = \frac{Z_1 Z_0 e^2}{2Mv^2} \tag{34}$$

where M is the reduced mass of the system;

$$k = \frac{(2\,ME_{cm})^{\frac{1}{2}}}{\hbar} \tag{35}$$

where E_{cm} is the kinetic energy of the two particles in the center-of-mass system;

$$\Phi_\ell = -\tan^{-1}\,(F_\ell/G_\ell)_{r=R} \tag{36}$$

where F_ℓ and G_ℓ are the regular and irregular Coulomb wave functions, respectively, and R is the radius of the charged sphere representing the nucleus; and

$$\Psi_\ell = \sigma_\ell - \sigma_o$$

where the Rutherford scattering phase shifts σ_ℓ are given by

$$\exp\,(2i\sigma_\ell) = \frac{(\ell + i\eta)\,(\ell - 1 + i\eta)\,\ldots\,(1 + i\eta)}{(\ell - i\eta)\,(\ell - 1 - i\eta)\,\ldots\,(1 - i\eta)}\ \exp\,(2i\sigma_o) \tag{37}$$

so that

$$\Psi_\ell = \sum_{s=1}^{\ell} \tan^{-1}\,\frac{\eta}{s} \qquad \text{and} \qquad \Psi_o = 0 \tag{38}$$

Although the radius of the charged sphere is not precisely determined by the theory, the idea inherent in the derivation is that the charged sphere represents a region of space from which the projectile is excluded by virtue of the finite sizes of the particles. Therefore the radius of the sphere should be equal to the sum of the radii of the two interacting particles. Call this radius the interaction radius.

Equation (32) was evaluated for various deuteron energies and scattering angles by using a Burroughs 220 computer. The hard-sphere phase shifts given by Eq. (36) were obtained by using a computer program written by Dr. T. Tombrello. A portion of the calculated results is shown in Fig. 23. Despite the fact that the radius values used in this calculation were about one-half the estimated interaction radius for the Be^9 + d system, the calculation yielded larger cross sections than the experiment. A value of zero for the total reaction cross section is likewise an unsatisfactory result of the hard-sphere model. This is particularly unrealistic in the case of Be^9 + d because studies of the possible reactions indicate that a substantial total reaction cross section exists.

2. Scattering by a Charged Sphere with Arbitrary Boundary Conditions at the Surface

Since the results calculated with the hard-sphere model disagreed with experiment, the effect of changing the boundary condition at the nuclear surface was investigated. In order to get an expression similar to Eq. (32) for arbitrary conditions at the spherical surface, we follow the derivation of Blatt and Weisskopf[19]. In doing this, we first derive expressions for the reaction and differential

scattering cross sections as functions of the complex amplitudes of the various scattered partial waves. Then we relate these amplitudes to the logarithmic derivative of the wave function at the spherical surface. This allows us to write the cross sections as functions of the logarithmic derivative of the wave function at this surface.

The wave function representing the beam of incident particles is a plane wave $\exp(i\underline{k}\cdot\underline{r})$ where $\underline{r}$ is a vector from the center of the target to the incident particle and $\underline{k}$ is the wave vector whose magnitude is given by Eq. (35) and whose direction is that of the incoming beam. For simplicity we assume the z-axis of the coordinate system is parallel to $\underline{k}$. It is possible to expand the incident wave in terms of spherical harmonics; thus in the limit of large kr the plane wave is given by

$$\exp(i\,k\,z) = \frac{\pi^{\frac{1}{2}}}{kr} \sum_{\ell=0}^{\infty} (2\ell+1)^{\frac{1}{2}}\, i^{\ell+1} \left\{\exp\left[-i\left(kr - \frac{\ell\pi}{2}\right)\right] - \exp\left[i\left(kr - \frac{\ell\pi}{2}\right)\right]\right\} Y_{\ell,0}(\Theta) \tag{39}$$

Because of the presence of the scatterer, the actual wave function is not a plane wave. However, the distortion caused by the scatterer only affects the outgoing spherical waves which go asymptotically as $\exp(ikr)$. Thus in the asymptotic region we write the actual wave function as

$$\psi(\underline{r}) = \frac{\pi^{\frac{1}{2}}}{kr} \sum_{\ell=0}^{\infty} (2\ell+1)^{\frac{1}{2}}\, i^{\ell+1} \left\{\exp\left[-i\left(kr - \frac{\ell\pi}{2}\right)\right] - \gamma_\ell \exp\left[i\left(kr - \frac{\ell\pi}{2}\right)\right]\right\} Y_{\ell,0}(\Theta) \tag{40}$$

where γ_ℓ is a complex number that determines the amplitude and phase of the outgoing ℓ-th partial wave. The difference between the true wave function and a plane wave is the scattered wave ψ_{sc} given by

$$\psi_{sc} = \psi(\underline{r}) - \exp(ikz)$$

$$= \frac{\pi^{\frac{1}{2}}}{kr} \sum_{\ell=0}^{\infty} (2\ell + 1)^{\frac{1}{2}} i^{\ell+1}(1 - \gamma_\ell) \exp[i(kr - \frac{\ell\pi}{2})]Y_{\ell,0}(\Theta) \qquad (41)$$

The reaction cross section is given by N_a/N where N_a is the number of particles removed from the beam per second and N is the number of particles per unit area per second in the incoming beam. The value of N_a is given by the net flux into a large sphere of radius r_o centered about the scatterer. This flux is found by integrating the probability current density, as determined from the complete wave function, over the surface of the large sphere. In this way N_a is found to be

$$N_a = \frac{-\hbar}{2iM} \int \left(\frac{\partial\psi}{\partial r} \psi^* - \frac{\partial\psi^*}{\partial r} \psi \right) r_o^2 \sin\Theta d\Theta \, d\Phi \qquad (42)$$

The flux of particles in a plane wave exp(ikz) is equal to the particle velocity v. This fact combined with the result of Eq. (42) yields

$$\sigma_{r,\ell} = \frac{\pi}{k^2} (2\ell + 1)(1 - |\gamma_\ell|^2) \qquad (43)$$

for the contribution to the reaction cross section from the partial wave having angular-momentum quantum number ℓ. Since $\sigma_{r,\ell}$ must not be negative, this result can be used to show that $|\gamma_\ell| \leq 1$. The contributions from the waves having different ℓ values are incoherent, so the total reaction cross section is given by

$$\sigma_r = \sum_{\ell=0}^{\infty} \sigma_{r,\ell} \tag{44}$$

The differential scattering cross section is determined by finding the number of particles N_{sc} scattered per second into an element of solid angle $d\Omega$ about Θ and then dividing this by the incident flux v. Using ψ_{sc} in the expression for the probability current density, we can equate the result for the flux through an element of surface on the large sphere to the number of scattered particles to get

$$N_{sc}(\Theta) = \frac{\hbar}{2iM}\left(\frac{\partial\psi_{sc}}{\partial r}\psi_{sc}^{*} - \frac{\partial\psi_{sc}^{*}}{\partial r}\psi_{sc}\right) r_o^{\,2}\, d\Omega \tag{45}$$

From this we find the differential elastic scattering cross section to be

$$\frac{d\sigma}{d\Omega} = \frac{\pi}{k^2}\left|\sum_{\ell=0}^{\infty}(2\ell+1)^{\frac{1}{2}}(1-\gamma_\ell)\,Y_{\ell,0}(\Theta)\right|^2 \tag{46}$$

We wish to relate the scattering and reaction cross section values to the boundary condition on the wave function at the nuclear surface. Since only the asymptotic behavior of the complete wave function $\psi(\underline{r})$ is given by Eq. (40), we now determine an expression for $\psi(\underline{r})$ which is valid everywhere outside the nucleus. We know that the general solution of the Schrödinger equation may be written in the form

$$\psi(\underline{r}) = \psi(r,\Theta) = \sum_{\ell=0}^{\infty}\frac{u_\ell(r)}{r}\,Y_{\ell,0}(\Theta) \tag{47}$$

We must now determine the proper radial wave functions $u_\ell(r)$.

Let us define linear combinations of $F_\ell(r)$ and $G_\ell(r)$ which correspond to outgoing and ingoing spherical waves. By examining the behavior of $F_\ell(r)$ and $G_\ell(r)$ for large r, we see that the combination

$$u_\ell^{(+)}(r) = \exp(-i\sigma_\ell)[G_\ell(r) + iF_\ell(r)] \tag{48}$$

has the desired outgoing spherical-wave character $\exp[i(kr - \frac{1}{2}\ell\pi)]$ in the asymptotic region. Similarly the combination

$$u_\ell^{(-)}(r) = \exp(i\sigma_\ell)\,[G_\ell(r) - iF_\ell(r)] \tag{49}$$

behaves asymptotically as an ingoing spherical wave. Using the functions $u_\ell^{(+)}$ and $u_\ell^{(-)}$ we can now write the radial wave function as the linear combination

$$u_\ell(r) = Au_\ell^{(-)}(r) + Bu_\ell^{(+)}(r) \tag{50}$$

To find A and B we compare the large-distance behavior of Eq. (50) with Eq. (40). This shows that

$$A = i^{\ell+1}(2\ell + 1)^{\frac{1}{2}}\frac{\pi^{\frac{1}{2}}}{k} \qquad \text{and} \qquad B = -\gamma_\ell A \tag{51}$$

The logarithmic derivative of $u_\ell(r)$ at the nuclear surface is defined by

$$f_\ell \equiv R\left[\frac{du_\ell/dr}{u_\ell}\right]_{r=R} \tag{52}$$

In addition we define quantities Δ_ℓ and s_ℓ by

$$R\left[\frac{du_\ell^{(+)}/dr}{u_\ell^{(+)}}\right]_{r=R} = \Delta_\ell + i\,s_\ell \tag{53}$$

Using Eq. (48) we can express Δ_ℓ and s_ℓ in terms of F_ℓ, G_ℓ, and their derivatives by

$$\Delta_\ell = R\left[\frac{G_\ell(dG_\ell/dr) + F_\ell(dF_\ell/dr)}{G_\ell^2 + F_\ell^2}\right]_{r=R} \tag{54}$$

$$s_\ell = R\left[\frac{G_\ell(dF_\ell/dr) - F_\ell(dG_\ell/dr)}{G_\ell^2 + F_\ell^2}\right]_{r=R} \tag{55}$$

Finally, we define a phase factor ξ_ℓ by the expression

$$\exp(2i\xi_\ell) = \frac{G_\ell(R) - i\,F_\ell(R)}{G_\ell(R) + i\,F_\ell(R)} \exp(2i\sigma_\ell) \tag{56}$$

It should be noted that all of the quantities defined by Eqs. (53) to (56) are specified completely by the conditions outside the nucleus.

We can now express the cross sections in terms of f_ℓ by relating f_ℓ to γ_ℓ. When Eqs. (50) and (51) are substituted into Eq. (52) the desired result is

$$\gamma_\ell = \frac{f_\ell - \Delta_\ell + i\,s_\ell}{f_\ell - \Delta_\ell - i\,s_\ell} \exp(2i\xi_\ell) \tag{57}$$

In order to examine the effect on the scattering due to interactions within the nucleus and to the Coulomb field and finite size, it is helpful to define amplitudes for scattering processes which occur inside and outside the nucleus. We introduce

$$A_{in}^\ell = \frac{-2i\,s_\ell}{(\mathrm{Re}\,f_\ell - \Delta_\ell) + i(\mathrm{Im}\,f_\ell - s_\ell)} \tag{58}$$

$$A_o^\ell = \exp(-2i\xi_\ell) - 1 \qquad (59)$$

where, to within a phase, A_{in}^ℓ and A_o^ℓ are the amplitudes for internal and external scattering processes, respectively. We note that when the wave function vanishes at the nuclear surface, i.e., $f_\ell = \infty$, A_{in}^ℓ vanishes as would be expected. Using Eqs. (58) and (59) the quantity $(1 - \gamma_\ell)$ may be written as $\exp(2i\xi_\ell)\,(A_o^\ell + A_{in}^\ell)$. Thus the differential scattering cross section becomes

$$\frac{d\sigma}{d\Omega} = \frac{\pi}{k^2}\left|\sum_{\ell=0}^{\infty}(2\ell+1)^{\frac{1}{2}}\exp(2i\xi_\ell)\,(A_o^\ell + A_{in}^\ell)\,Y_{\ell,0}(\Theta)\right|^2 \qquad (60)$$

Equation (60) is not suitable for computational purposes because the long range of the Coulomb interaction causes the sum to converge very slowly. In order to overcome this difficulty, we can replace the partial-wave form of the amplitude for Rutherford scattering by an equivalent expression. Manipulation of Eq. (60) yields

$$\frac{d\sigma}{d\Omega} = \left| -i\frac{\pi^{\frac{1}{2}}}{k}\sum_{\ell=0}^{\infty}(2\ell+1)^{\frac{1}{2}}\left[\exp(2i\sigma_\ell) - 1\right]Y_{\ell,0}\right.$$

$$+ i\frac{\pi^{\frac{1}{2}}}{k}\sum_{\ell=0}^{\infty}(2\ell+1)^{\frac{1}{2}}\exp(2i\sigma_\ell)\times$$

$$\left.\left\{1 - \exp(2i\xi_\ell - 2i\sigma_\ell)\left[1 - A_{in}^\ell\right]\right\}Y_{\ell,0}\right|^2 \qquad (60a)$$

Now $Y_{\ell,0}(\Theta) = [(2\ell+1)/4\pi]^{\frac{1}{2}} P_\ell(\cos\Theta)$, so the slowly-converging term in the sum becomes

$$\frac{1}{2\,ik}\sum_{\ell=0}^{\infty}(2\ell+1)\,[\exp(2i\sigma_\ell)-1]\,P_\ell(\cos\Theta)$$

This may be replaced by the equivalent expression for the Rutherford scattering amplitude

$$-z\,\csc^2(\tfrac{1}{2}\Theta)\exp[-2i\eta\,\ell n\sin(\tfrac{1}{2}\Theta)+2i\sigma_o]$$

After factoring out the constant factor $\exp(2i\sigma_o)$, the expression for the cross section becomes*

$$\frac{d\sigma}{d\Omega}=\Bigg|\, z\,\csc^2(\tfrac{1}{2}\Theta)\exp[-2i\eta\,\ell n\sin(\tfrac{1}{2}\Theta)]$$
$$-i\frac{\pi^{\frac{1}{2}}}{k}\sum_{\ell=0}^{\infty}(2\ell+1)^{\frac{1}{2}}\exp(2i\sigma_\ell-2i\sigma_o)\times$$
$$\left\{1-\exp(2i\xi_\ell-2i\sigma_\ell)\left[1-A_{in}^{\ell}\right]\right\}Y_{\ell,0}\Bigg|^2 \qquad (61)$$

Before squaring Eq. (61) we note that $\sigma_\ell-\sigma_o=\psi_\ell$ and the quantities z, k, η, and Θ are again defined by the expressions following Eq. (32). In addition, Eq. (56) shows that

$$\exp(2i\xi_\ell-2i\sigma_\ell)=\frac{G_\ell(R)-iF_\ell(R)}{G_\ell(R)+iF_\ell(R)}$$

Now using $\Phi_\ell=-\tan^{-1}(F_\ell/G_\ell)_{r=R}$, we can find that

$$\exp(2i\Phi_\ell)=\frac{G_\ell(R)-iF_\ell(R)}{G_\ell(R)+iF_\ell(R)}$$

---

* The equivalent expression on p. 336 of Blatt and Weisskopf contains an error in the sign of A_{res}^{ℓ}.

Thus

$$\xi_\ell - \sigma_\ell = \Phi_\ell$$

In Eq. (61) the expression to be squared has the form $|T|^2 = |T_1 + T_2|^2$; this can be expanded to yield $|T|^2 = |T_1|^2 + |T_2|^2 + 2\mathrm{Re}(T_1 T_2^*)$ where Re means the real part of the bracket. Using this and the expansion for writing the product of two spherical harmonics as a linear combination of spherical harmonics, the final result, after dividing by the Rutherford cross section, becomes

$$\frac{d\sigma}{d\sigma_R} = 1 - \mathrm{Re}\left[\frac{i \sin^2(\frac{1}{2}\Theta)}{kz} \exp[2i\eta\, \ell n \sin(\tfrac{1}{2}\Theta)] \sum_{\ell=0}^{\infty} (2\ell + 1) \exp(2i\psi_\ell) \times \left\{1 - \exp(2i\Phi_\ell)\left[1 - A_{in}^{\ell}\right]\right\} P_\ell (\cos\Theta)\right]$$

$$+ \frac{\sin^4(\frac{1}{2}\Theta)}{4k^2 z^2} \sum_{L=0}^{\infty} \sum_{\ell=0}^{\infty} \sum_{\ell' = |\ell - L|}^{\ell+L} (2\ell+1)(2\ell'+1) \exp(2i\psi_{\ell'} - 2i\psi_\ell) \times$$

$$[(\ell\ell' 00 | \ell\ell' L0)]^2 \left\{1-\exp(2i\Phi_\ell)\left[1-A_{in}^{\ell}\right]\right\}^* \left\{1-\exp(2i\Phi_{\ell'})\left[1-A_{in}^{\ell'}\right]\right\} P_L (\cos\Theta) \tag{62}$$

Equation (62) has been derived without considering the spins of the interacting particles. It can be shown that when no resonances in the scattering are present, the effect of the particle spins does not alter the expression for the scattering cross section which this model predicts. Although more sophisticated models can be used to describe the scattering interaction, the simplicity of the charged-sphere model is a virtue which cannot be overlooked. In view of the satisfactory results obtained with this simple model, little additional physical insight can be gained by analyzing these data with a more complicated

model.

3. Determining the Parameters Required to Fit the Experimental Data

The expression which has been derived for the scattering cross section depends upon the parameters A_{in}^{ℓ} and the interaction radius. Aside from the value of zero for the A_{in}^{ℓ} when the wave function vanishes at the nuclear surface, it is difficult to decide what constitutes "reasonable" values of A_{in}^{ℓ} under more general conditions. The scattered-wave amplitudes γ_{ℓ}, however, do have a more apparent physical interpretation. A program to evaluate Eq. (62) was written for a Burroughs 220 computer. By using several reasonable values of γ_{ℓ}, the values that gave the best agreement between theory and experiment were found by trial and error.

The relatively low incident energies used in this experiment suggest that only modification of the s- and p-waves by the internal region of the nucleus should be considered. Thus the γ_{ℓ} for the d-waves and higher were assumed to be the hard charged sphere result $\gamma_{\ell} = \exp(2i\xi_{\ell})$.

We see from Eq. (43) that the reaction cross section is determined by the magnitudes of the γ_{ℓ}. In order to find these magnitudes, the variation of the total reaction cross section with energy was estimated from data available in the literature and is shown in Fig. 24. The data used in constructing this figure were taken from references 20 through 23. Because of the large number of possible reactions, these data are incomplete. Therefore, this composite total reaction cross section curve is probably only a lower estimate.

The first attempt to fit the experimental results was made for the incident energy of 0.500 Mev. Here it was assumed that only the s-wave would contribute to the reaction cross section; this determined $|\gamma_0|$ uniquely. The variation in the cross section due to changes in the phase of γ_0 and the interaction radius was examined and the best fit to the experimental results was determined by minimizing

$$E = \sum_{\Theta} \frac{[\sigma_e(\Theta) - \sigma_c(\Theta)]^2}{\sigma_c(\Theta)} \tag{63}$$

where the subscripts refer to experimental and calculated values. The interaction radius which gave the best fit was 3.7 fermis, although the minimum in Eq. (63) was rather broad. For comparison, the expression

$$r = 1.20\ (A_0^{1/3} + A_1^{1/3})\ \text{fermis}$$

gives a rough estimate of 4.0 fermis for the sum of the radii of the two particles.

Using an interaction radius of 3.7 fermis, the values of γ_0 and γ_1 required to fit the experimental numbers were determined for higher incident energies. At 0.700 Mev a slight amount of p-wave contribution to the reaction cross section was introduced. This required that the relative magnitudes of γ_0 and γ_1 also be determined by trial and error. Figures 25 through 28 show the effect on the calculated cross sections due to the variations in the various quantities.

The values for the coefficients γ_0 and γ_1 which produce the best fit to the experimental data are listed in Table III and plotted in Fig. 29. It must be remembered that for bombarding energies of 0.700 Mev

and higher, the availability of four parameters, the magnitude and argument of both γ_0 and γ_1, should permit an exact fit of four cross sections having almost any values. Thus the significant fact learned from the charged sphere calculations is not that a fit is possible, but rather that the parameters which give a fit vary in a reasonable way as the bombarding energy is changed. Undoubtedly the unevenness in the variation of the parameters shown in Table III can be attributed to uncertainties in the scattering and reaction cross sections and the relative crudeness of the trial-and-error fitting procedure. Although it may be possible to interpret the elastic scattering of deuterons in terms of a more sophisticated model than that used here, it appears that the cross sections measured in this experiment are compatible with the assumption of scattering by a slightly-absorbing charged sphere.

V. DISCUSSION OF RESULTS

A comparison of the present results with those given by Jurić and Ćirilov[2] reveals that the two measurements are in disagreement concerning the existence of two states in B^{11} formed at incident-deuteron energies of 1.16 Mev and 1.34 Mev and having widths of 70 Kev and 120 Kev, respectively. To aid in evaluating the relative trustworthiness of these two experiments, a few comments concerning the earlier experiment seem pertinent.

Jurić and Ćirilov used photographic plates to detect the scattered deuterons. The tracks due to these deuterons were distinguished from those due to the reaction products by examining the lengths of the tracks. However, at certain angles of observation, one or more of the reaction products had the same range in the emulsion as the scattered deuterons. This difficulty was supposedly overcome by determining the number of each type of particle in an angular region where no range overlap occurred and then extrapolating to the region where the different types of particles had the same range. An error of four percent which they attributed to this extrapolation procedure seems rather optimistic.

Another factor which tends to cast doubt upon Jurić and Ćirilov's results is the target they claim to have used. They quote a value of 0.9 mg/cm^2 for the approximate thickness of their beryllium target. It is possible that this thickness was misprinted. However, if the stated thickness is correct, such a target would have a thickness of over 300 Kev for a one-Mev deuteron. The reaction products created at

various depths in the target would have a wide range of energies; this would complicate their identification according to the length of the emulsion tracks which they produced. In addition, a target of the stated thickness would make it very difficult to determine accurate values for the energies of the deuterons when they actually underwent scattering. In view of such difficulties, it is hard to understand how these authors could have obtained yield curves which vary with energy as rapidly as their results indicate.

A possible explanation for the 1.34-Mev anomaly which Juric and Cirilov observed is the elastic scattering of deuterons by a carbon contaminant layer on the face of their target. No mention of this possibility was made by the authors. Recent data for $C^{12}(d,d)C^{12}$ scattering[24] indicate that a peak in the cross section occurs at about E_d = 1.30 Mev. Although the deuterons scattered by carbon would have more energy when detected than those scattered by beryllium, the energies of these two groups of deuterons could differ, depending upon the scattering angle, at most by 20 percent. Whether the resulting differences in track length for the yields from $Be^9(d,d)Be^9$ and $C^{12}(d,d)C^{12}$ could be reliably resolved is open to question.

Judging from the variation of the $C^{12}(d,d)C^{12}$ cross section with energy, it seems unlikely that the anomaly at 1.16 Mev can also be attributed to scattering by a carbon contaminant layer. However, the presence of some other contaminant, such as oxygen, is very possible. Unfortunately, the $O^{16}(d,d)O^{16}$ cross section at low energies has not been measured, so no comparison can be made with the results of Juric and Cirilov.

Since these earlier data were available at the time of the present experiment, the procedures used in making the present measurements were examined closely for any possible sources of error. None was found. In view of the results obtained in this experiment, it must be concluded that the anomalies in the $Be^9(d,d)Be^9$ elastic scattering cross section reported by Jurić and Ćirilov are spurious.

An unusual feature of the excitation functions shown in Fig. 22 is the occurrence of cross sections which fall below the Rutherford values at low bombarding energies. This sub-Rutherford effect is interesting because similar results were observed for a recent measurement of the $Li^7(d,d)Li^7$ scattering cross section.(1) One might expect that as the bombarding energy is decreased the projectile approaches less and less closely to the nucleus and the point-charge assumption of the Rutherford theory is increasingly well satisfied. Thus the fact that the measured cross sections dip below Rutherford is not trivial.

There are two possible ways to account for the observed cross section being less than the Rutherford value. It is possible that the scattering cross section really is less than Rutherford at low energies because of absorption or some obscure effect peculiar to the structure of the deuteron. In fact the previously-described charged sphere calculations shown in Fig. 25 indicate that a sub-Rutherford cross section can result when the phase of the outgoing partial wave is shifted somewhat from the hard-sphere value.

A second possible explanation for the observed sub-Rutherford cross sections is that the cross section really has the Rutherford

value, but the measured values are low because of some instrumental or other experimental difficulty for which an adequate correction has not been made. For example, it is possible that the charge equilibrium ratios are not yet accurately known. In view of the great care taken by Phillips in his experiment, this is not considered likely. Another possibility is that some contaminant, say oxygen, in the surface layers of the target increased the effective atomic stopping cross section from the pure-beryllium value. Then when the cross sections are calculated with Eq. (21), the use of beryllium stopping cross sections gives scattering cross sections which are lower than the true values. This effect is possibly important at low energies because the thickness of the target layer from which the magnetic spectrometer selects scattered particles is smaller at low energies than at high energies. This means that the thickness of the comtaminated region constitutes an appreciable fraction of the entire thickness of the target layer. Although this reasoning seems to account for the sub-Rutherford behavior of the $Li^7(d,d)Li^7$ scattering, the amount of contaminant present in this experiment is not sufficient to explain the observed results. Ford[1] has measured the scattering cross section for Cu(d,d)Cu with incident energies such that the energies of the scattered deuterons were comparable to the lowest scattered-deuteron energies in this experiment. This measurement was performed with the same equipment used in this experiment, and the cross section was found to be within three percent of the Rutherford value. This appears to rule out gross instrumental effects and anomalous effects due to the deuteron's structure as possible causes of the sub-Rutherford cross section.

After examining possible reasons for the observed below-Rutherford values of the cross section at low energies, the most reasonable explanation seems to be that the true cross section is below Rutherford. However, small contributions to the observed lowering from the other causes which were mentioned cannot be ruled out completely.

An important point to be considered is the possible failure to observe a bona fide resonant-level anomaly in the cross section. The data shown in Fig. 22 were measured at 20-Kev intervals, so it seems reasonable to assume that any appreciable anomaly having a spread greater than 30 Kev would certainly have been observed. In view of the high excitation energy of the $Be^9 + d \rightarrow B^{11*}$ compound nucleus, the occurrence of an anomaly in this region with a spread less than 30 Kev, although possible, is not likely. Thus there is little reason to suspect that in this experiment an isolated resonance may have been overlooked. It should be noted, however, that the gradual rise in the scattering cross sections with increasing bombarding energy may be due to the presence of many broad, overlapping levels. A rough estimate of the expected level density can be made by assuming the nucleus is a degenerate Fermi gas of eleven particles confined within the nuclear volume. Under these conditions, it can be shown that for an excitation energy of 17 Mev the level density in B^{11} should be about 25 levels per Mev.

The existence of one or two states in B^{11} having about 17 Mev excitation is suggested by some of the $Be^9 + d$ reaction data. It is of interest to consider whether the absence of structure in the $Be^9(d,d)Be^9$ cross section can be explained in terms of the relative magnitudes of the probabilities for decay of the compound nucleus by various channels.

From barrier penetration considerations the decay of a B^{11} compound-nucleus state by emission of a particle other than a deuteron is favored because of the large Q values for many of these reaction channels. The decay by neutron emission is further enhanced by the absence of any Coulomb barrier. For example, if a state in B^{11} with spin and parity $3/2^+$ is formed in the excitation region under consideration, then the conservation laws require p-wave deuterons for its formation. But this state can decay by one of more than a dozen reaction channels for which ℓ-values less than or equal to two are allowed. An estimate of the probability of deuteron re-emission can be made by assuming that the probability of decay by a channel c is proportional to $k_c r_c P_\ell(k_c r_c)$ where k_c, r_c, and $P_\ell(k_c r_c)$ are the wave number, interaction radius, and penetration factor, respectively, which are appropriate to channel c. In this way it is found that the probability of deuteron re-emission by a $3/2^+$ state formed at a bombarding energy of one Mev is about 0.004.

The consequence of a small probability for the emission of a deuteron during the decay of the compound nucleus is a small value for the ratio of the deuteron-emission width to the total decay width, Γ_d/Γ. Since the amplitude for scattering by compound nucleus formation near a resonance is roughly proportional to Γ_d/Γ, it is necessary that Γ_d/Γ be large enough to produce a noticeable interference with the Coulomb scattering if an anomaly is to appear in the scattering cross section.

The effect on the scattering cross section caused by a state having a very small value of Γ_d/Γ can be estimated. Suppose that a resonant state in B^{11} is formed when the incident deuteron energy is

one Mev, that its total decay width is 500 Kev, and that $\Gamma_d/\Gamma = 0.01$. Then a simplified calculation, neglecting spins and finite nuclear size effects, shows that under these conditions the scattering cross section varies only about two percent from the Rutherford value. Since other effects, such as the finite nuclear sizes, also cause deviation from pure Rutherford scattering, an anomaly of this order of magnitude would be difficult to identify.

It is interesting to note that the excitation function measured at 163° 30' indicates a slight dip in the cross section near a bombarding energy of one Mev. This may be due to the formation of a compound-nucleus state with a very small value of Γ_d/Γ. A rough estimate indicates that the cross section deviates from the smooth trend by about two percent. Such a deviation is consistent with the previous estimate for the value of Γ_d/Γ which would be expected for this reaction. However, the small size of this anomaly means that its presence can hardly be considered proof of the existence of a state in B^{11}.

VI. SUMMARY

The results obtained in this experiment offer no support for the existence of levels in B^{11} with excitations near 17 Mev. It has been argued that the absence of anomalies in the $Be^9(d,d)Be^9$ cross section does not rule out the presence of such levels. The lack of structure in the scattering cross section does require that Γ_d/Γ for any levels in the excitation region of interest be very small. That this is a reasonable possibility follows from the properties of the Be^9 + d system.

The present extent of the information concerning the B^{11} excitation region of interest is as follows: Some of the Be^9 + d reactions suggest the presence of levels in this region. The data from which these inferences are drawn are by no means sufficiently clear-cut to yield any information about spins and parities. Recent B^{10} + n data [25], [26] show two small maxima which are about the size of the experimental uncertainty at incident neutron energies which correspond to a B^{11} excitation just below 17 Mev. However, the $B^{10}(n,t\ 2\alpha)$ cross section is in serious disagreement with earlier measurements[27], [28] which showed a single, pronounced maximum in the cross section. Again the sizes of the anomalies preclude any analysis to determine spins and parities. Perhaps the most conclusive evidence for a level in this region comes from a study[29] of the reaction $Li^7(\alpha,n)B^{10}$. In this case the neutron yield at zero degrees shows a pronounced maximum at a position where levels have been suggested previously.

The fact that the $Li^7(\alpha,n)B^{10}$ experiment indicates an appreciable

probability for compound nucleus formation by the $Li^7 + \alpha$ channel immediately suggests that the scattering experiment $Li^7(\alpha,\alpha)Li^7$ might help to clarify the level spectrum in B^{11}. Although a laboratory energy of 14 Mev for the alpha particles is required to reach the B^{11} excitation considered here, this is not unreasonable for a doubly-charged alpha-particle beam from a tandem accelerator. Furthermore, if analyzable results are obtained, the zero spin of the alpha particle will simplify considerably the interpretation of the experimental data.

APPENDIX I

Sample Calculation of the Differential Scattering Cross Section From the Experimental Yield

The differential scattering cross section is calculated from the experimental yield by using

$$\left(\frac{d\sigma}{d\Omega}\right)_L = \frac{Ze\ N_R}{2V\ E_{20}} \frac{n_s}{n_d} \frac{R}{C\Omega_L} \epsilon_2(E_{20}) \left[\frac{\cos \Theta_1}{\cos \Theta_2} + \frac{\epsilon_1(E_1)}{\epsilon_2(E_2)} \left(\frac{\partial E_2}{\partial E_1}\right)_\Theta\right] \tag{21}$$

As an example of this calculation, consider the thick-target profile shown in Fig. 17. The pertinent experimental quantities are

$$E_{1B} = 1.005 \text{ Mev}$$
$$\Theta_L = 113^\circ 26'$$
$$C = 1.00 \times 10^{-6} \text{ farads}$$
$$V = 9.452 \text{ volts}$$
$$\Theta_1 = \Theta_2$$

Assume that the yield is measured at $V_m = 609$ mv. Then Eq. (2) is used to find $E_m = E_{20} = 0.5139$ Mev. From the data given by Mozer,[11] the stopping cross sections

$$\epsilon_1(E_{1B}) = 5.23 \times 10^{-15} \text{ ev - cm}^2$$
$$\epsilon_2(E_{20}) = 7.64 \times 10^{-15} \text{ ev - cm}^2$$

are obtained. For elastic scattering with $\Theta_L = 113^\circ 26'$ and

$$M_1 = M_2 = 2.015 \text{ amu}$$
$$M_0 = M_3 = 9.015 \text{ amu}$$

it follows that

$$\left(\frac{\partial E_2}{\partial E_1}\right)_\Theta = \alpha = 0.5290$$

By substituting into Eq. (22), it is found that $E_1 = 0.9960$ Mev and $E_2 = \alpha E_1 = 0.5269$ Mev. The stopping cross sections appropriate to these energies are

$$\epsilon_1(E_1) = 5.25 \times 10^{-15} \text{ ev - cm}^2$$

$$\epsilon_2(E_2) = 7.53 \times 10^{-15} \text{ ev - cm}^2$$

Thus

$$\epsilon_2(E_{20})\left[\frac{\cos\Theta_1}{\cos\Theta_2} + \frac{\epsilon_1(E_1)}{\epsilon_2(E_2)}\left(\frac{\partial E_1}{\partial E_2}\right)_\Theta\right] = 1.05 \times 10^{-14} \text{ ev - cm}^2$$

$$= 1.05 \times 10^{7} \text{ Mev - mb} \qquad \text{(A1)}$$

Using the previously-discussed values of $R = 302$ and $\Omega_L = 1.47 \times 10^{-3}$ steradians, it follows that

$$\frac{R}{C\Omega_L} = 2.05 \times 10^{11} \text{ farads}^{-1} \text{ - steradian}^{-1} \qquad \text{(A2)}$$

From Fig. 17 the net yield at $V_m = 609$ mv is found to be

$$N_R = 1350 - 52 = 1298$$

For the particular bombarding energy and scattering angle being considered here, the charge-neutralization and dead-time corrections are negligible. Thus

$$\frac{Ze\ N_R}{2V\ E_{20}} = \frac{(1)\ (1.602 \times 10^{-19})\ (1298)}{(2)\ (9.452)\ (0.5139)} = 2.141 \times 10^{-17}\ \frac{\text{farads}}{\text{Mev}} \qquad \text{(A3)}$$

For a pure beryllium target $n_s/n_d = 1$. Finally, by combining (A1),

(A2), and (A3) the laboratory differential scattering cross section is found to be

$$\left(\frac{d\sigma}{d\Omega}\right)_L = (2.14 \times 10^{-17})\ (2.05 \times 10^{11})\ (1.05 \times 10^{7}) = 46.1 \ \frac{mb}{sterad.}$$

The center-of-mass scattering angle is found from Eq. (27b) to be $\Theta_C = 125^{\circ}16'$, and the factor for converting the value of the cross section from the laboratory to the center-of-mass system is found from Eq. (25b) to be

$$\frac{d\Omega_L}{d\Omega_C} = 1.236$$

Thus

$$\left(\frac{d\sigma}{d\Omega}\right)_C = (1.236)\ (46.1) = 57.0 \ \frac{mb}{sterad.}$$

The appropriate Rutherford cross section is calculated from Eq. (24) and found to be

$$\left(\frac{d\sigma_R}{d\Omega}\right)_C = 50.21 \ \frac{mb}{sterad.}$$

Thus the ratio of the observed cross section to the Rutherford value is

$$\frac{d\sigma}{d\sigma_R} = 1.13$$

References

1. J. L. C. Ford, Jr., Ph.D. Thesis, California Institute of Technology, (1962)
2. Juric´ and Cirilov, Bull. Inst. N. Sciences "Boris Kidrich" 6: 45 (1956)
3. Shpetnyi, Zh. Eksp. Teor. Fiz. ("Soviet Physics") 5: 357 (1957)
4. Neilson, Dawson and Sample, Bull. Amer. Phys. Soc. 3: 323 (1958)
5. Lauritsen, Lauritsen and Fowler, Phys. Rev. 59: 241 (1941)
6. E. A. Milne, Ph.D. Thesis, California Institute of Technology (1953)
7. Snyder, Rubin, Fowler and Lauritsen, R. S. I. 21: 852 (1950)
8. Friedland, Mayer and Wiggins, Nucleonics 18: 54 (1960)
9. R. E. Brown, Ph.D. Thesis, California Institute of Technology (1962)
10. Brown, Snyder, Fowler and Lauritsen, Phys. Rev. 82: 159 (1950)
11. F. S. Mozer, Ph.D. Thesis, California Institute of Technology (1955)
12. Phillips, Phys. Rev. 97: 404 (1955)
13. W. A. Wenzel, Ph.D. Thesis, California Institute of Technology (1952)
14. Foldy, Phys. Rev. 83: 397 (1951)
15. French and Goldberger, Phys. Rev. 87: 899 (1952)
16. F. B. Morinigo, Private Communication
17. W. Whaling, Class Lecture
18. Blatt and Biedenharn, Revs. Mod. Phys. 24: 258 (1952)
19. Blatt and Weisskopf, Theoretical Nuclear Physics, John Wiley, New York, 1952, p. 311
20. De Jong, Endt and Simons, Physica 18: 676 (1952)

References

21. J. A. Biggerstaff, Ph.D. Thesis, University of Kentucky (1961)

22. Neilson, Dawson, Johnson and Sample, Suffield Technical Paper No. 176, Suffield Experiment Station, Ralston, Alberta

23. Bardes and Owen, Phys. Rev. 120: 1369 (1960)

24. Kashy, Perry and Risser, Phys. Rev. 117: 1289 (1960)

25. Fossan, Walter, Wilson and Barschall, Phys. Rev. 123: 209 (1961)

26. Davis, Gabbard, Bonner and Bass, Nuc. Phys. 27: 448 (1961)

27. Frye and Gammel, Phys. Rev. 103: 328 (1956)

28. Wyman, Bull. Amer. Phys. Soc. 3: 187 (1958)

29. Mehta, Hunt, Plendl and Davis, Bull. Amer. Phys. Soc. 6: 226 (1961); and Tandem Accelerator Laboratory Annual Progress Report for 1961, Florida State University p. 12

30. R. K. Bardin, Ph.D. thesis, California Institute of Technology (1961).

TABLE I

Values of the Magnetic Spectrometer Acceptance Solid Angle Measured at Various Proton Energies and Laboratory Scattering Angles (in millisteradians)

E_1 in Mev	Θ_L $158^\circ 53'$	$113^\circ 26'$	$77^\circ 24'$
0.6028	1.469 ± 0.011		
0.7033	1.466 ± 0.012		
0.9042	1.458 ± 0.014	1.472 ± 0.006	1.466 ± 0.009
1.206	1.486 ± 0.012		

TABLE II

A. The Relative Uncertainty in $d\sigma/d\sigma_R$

Uncertainty Due to:	Contribution to the Relative Fractional Standard Deviation in $d\sigma/d\sigma_R$ Θ_L $158^\circ 53'$	$113^\circ 26'$	$77^\circ 24'$
1. N_R	2.0 %	2.0 %	0.92 %
2. V	0.50	0.50	0.50
3. E_{20}	0.30	0.30	0.30
4. $\epsilon(E_{20})$	2.0	2.0	2.0
5. $\cos \Theta_1/\cos \Theta_2 + \alpha [\epsilon(E_1)/\epsilon(E_2)]$	0.24	0.40	0.73
6. E_1^2	0.40	0.40	0.40
Resulting Relative Fractional Standard Deviation for $d\sigma/d\sigma_R$	2.9 %	2.9 %	2.4 %
At the Lowest Values of E_{20}, Additional Uncertainty is Due to:			
Noise Subtraction When Determining N_R	8.0	8.0	0
At the Lowest Values of E_{20}, Resulting Fractional Standard Deviation for $d\sigma/d\sigma_R$	8.3 %	8.3 %	2.4 %

TABLE II (Continued)

B. The Absolute Uncertainty in $d\sigma/d\sigma_R$

Uncertainty Due to:	Contribution to the Absolute Fractional Standard Deviation in $d\sigma/d\sigma_R$ Θ_L $158^\circ 53'$	$113^\circ 26'$	$77^\circ 24'$
1. N_R^b	2.0 %	2.0 %	0.92%
2. N_R^c	0.35	0.35	0.35
3. V^b	0.50	0.50	0.50
4. V^c	0.50	0.50	0.50
5. E_{20}^b	0.30	0.30	0.30
6. E_{20}^c	0.30	0.30	0.30
7. $\epsilon^b(E_{20})$	4.40	4.40	4.40
8. $\epsilon^c(E_{20})$	3.70	3.70	3.70
9. $\left[\frac{\cos\Theta_1^b}{\cos\Theta_2^b}+\alpha^b\frac{\epsilon^b(E_1)}{\epsilon^b(E_2)}\right]\left[\frac{\cos\Theta_1^c}{\cos\Theta_2^c}+\alpha^c\frac{\epsilon^c(E_1)}{\epsilon^c(E_2)}\right]^{-1}$	2.39	2.47	2.74
10. $(E_1^b)^2$	0.40	0.40	0.40
11. $(E_2^b)^2$	0.40	0.40	0.40
12. $(\sin\frac{1}{2}\Theta_C^b/\sin\frac{1}{2}\Theta_C^c)^4$	0.07	0.58	1.42
Resulting Absolute Fractional Standard Deviation for $d\sigma/d\sigma_R$	6.6 %	6.7 %	6.7 %
At the Lowest Values of E_{20}^b, Additional Uncertainty is Due to:			
1. Noise Subtraction When Determining N_R^b	8.0	8.0	0

TABLE II (Continued)

	Contribution to the Absolute Fractional Standard Deviation in $d\sigma/d\sigma_R$		
	Θ_L		
	$158^\circ 53'$	$113^\circ 26'$	$77^\circ 24'$
2. Charge Equilibrium Ratio	3.0 %	3.0 %	3.0 %
At the Lowest Values of E^b_{20}, Resulting Absolute Fractional Standard Deviation for $d\sigma/d\sigma_R$	10.6 %	10.7 %	7.3 %

TABLE III

Charged-Sphere Parameters Which Produce the Best Fit to the Experimental Cross Sections

E_1 in Mev	σ_r in mb	γ_o	γ_1	arg γ_o	arg γ_1	E
0.500	74.3	0.9613	1.0000	$2\xi_o + 6.5^o$	$2\xi_1$	3.8×10^{-3}
0.600	129.3	0.9163	1.0000	$2\xi_o + 4.3^o$	$2\xi_1$	2.8×10^{-3}
0.700	166.4	0.9049	0.9900	$2\xi_o + 2.5^o$	$2\xi_1 + 3^o$	25×10^{-6}
0.800	215.0	0.9064	0.9700	$2\xi_o + 1.5^o$	$2\xi_1$	28×10^{-6}
0.900	258.4	0.9100	0.9471	$2\xi_o + 1.0^o$	$2\xi_1$	61×10^{-6}
1.000	289.2	0.8800	0.9323	$2\xi_o + 1.1^o$	$2\xi_1 + 2^o$	105×10^{-6}
1.100	328.5	0.9000	0.9062	$2\xi_o + 0.5^o$	$2\xi_1$	82×10^{-6}
1.200	354.7	0.8700	0.8874	$2\xi_o - 0.7^o$	$2\xi_1$	105×10^{-6}

TABLE IV

$\theta_c = 90^\circ$

E_1 in kev	$(d\sigma/d\Omega)_c$ in mb-ster^{-1}	$(d\sigma/d\sigma_R)$	E_1 in kev	$(d\sigma/d\Omega)_c$ in mb-ster^{-1}	$(d\sigma/d\sigma_R)$
357.4	911	0.937	794.1	203	1.03
378.1	821	0.947	815.5	196	1.05
397.4	755	0.960	834.4	189	1.06
417.4	688	0.965	854.4	184	1.08
436.9	623	0.957	874.7	179	1.10
457.8	574	0.968	894.8	166	1.07
476.2	529	0.966	911.4	159	1.06
496.9	492	0.976	931.6	156	1.09
516.9	454	0.977	951.5	151	1.10
537.7	414	0.963	970.5	148	1.13
556.6	380	0.948	992.8	141	1.12
577.0	358	0.959	1013	139	1.15
595.4	340	0.972	1032	137	1.17
615.8	311	0.947	1052	132	1.18
636.2	290	0.945	1071	129	1.19
657.4	275	0.956	1091	127	1.22
676.7	259	0.954	1111	125	1.24
694.1	248	0.961	1129	121	1.24
714.9	243	0.999	1150	119	1.27
735.4	228	0.992	1170	117	1.29
755.3	217	0.992	1190	112	1.28
770.1	215	1.03			

TABLE IV (continued)

$\theta_c = 125^\circ\ 16'$

E_1 in kev	$(d\sigma/d\Omega)_c$ in mb-ster^{-1}	$(d\sigma/d\sigma_R)$	E_1 in kev	$(d\sigma/d\Omega)_c$ in mb-ster^{-1}	$(d\sigma/d\sigma_R)$
399.8	269	0.862	1017	54.8	1.14
420.1	235	0.831	1036	53.3	1.15
440.0	225	0.871	1057	51.4	1.15
458.9	208	0.880	1077	49.9	1.16
479.8	196	0.904	1099	47.2	1.14
499.4	176	0.878	1117	47.2	1.18
520.1	173	0.941	1136	45.6	1.18
539.4	159	0.926	1156	44.2	1.18
560.3	153	0.959	1177	42.7	1.19
579.8	141	0.953	1196	42.2	1.21
598.8	137	0.980	1215	40.9	1.21
618.6	128	0.983	1236	39.8	1.22
639.6	121	0.991	1256	39.4	1.25
659.9	117	1.02	1276	36.9	1.20
680.0	108	0.999	1296	36.4	1.22
699.0	106	1.04	1315	35.0	1.22
719.3	100	1.04	1335	34.0	1.22
739.2	96.2	1.05	1355	33.8	1.24
759.8	93.3	1.08	1376	33.2	1.26
779.9	88.6	1.08	1396	32.3	1.26
799.3	81.4	1.04	1416	32.8	1.32
818.9	80.5	1.08	1434	31.6	1.30
838.7	77.3	1.09	1454	31.1	1.32
859.1	73.0	1.08	1473	30.6	1.33
879.0	70.2	1.09	1494	30.4	1.36
899.5	65.7	1.07	1515	29.0	1.34
918.3	65.2	1.10	1534	28.6	1.35
937.3	61.7	1.09	1552	26.1	1.26
956.6	59.9	1.10	1572	27.1	1.34
975.4	58.7	1.12	1592	27.8	1.41
997.5	56.9	1.14	1612	28.2	1.47

TABLE IV (continued)

$\Theta_c = 163^\circ\ 30'$

E_1 in kev	$(d\sigma/d\Omega)_c$ in mb-ster^{-1}	$(d\sigma/d\sigma_R)$	E_1 in kev	$(d\sigma/d\Omega)_c$ in mb-ster^{-1}	$(d\sigma/d\sigma_R)$
480.1	120	0.857	1142	25.2	1.02
499.7	109	0.840	1162	25.2	1.05
521.0	101	0.851	1182	25.1	1.08
540.8	98.4	0.891	1.201	23.8	1.06
560.1	91.6	0.889	1.220	22.7	1.04
580.8	88.0	0.916	1.240	22.4	1.06
601.5	84.5	0.945	1.260	22.2	1.09
619.3	81.4	0.963	1.281	22.0	1.12
639.8	77.4	0.976	1.300	21.3	1.11
659.8	74.6	1.00	1.320	20.9	1.12
680.9	73.4	1.05	1.341	20.7	1.15
701.6	67.7	1.03	1.360	20.4	1.16
718.8	64.5	1.03	1.381	20.2	1.19
740.9	61.3	1.04	1.400	20.1	1.22
760.0	58.5	1.04	1.420	19.9	1.23
781.3	58.4	1.10	1.440	19.4	1.24
800.1	52.6	1.04	1.460	18.9	1.24
820.8	51.5	1.07	1.479	18.5	1.25
839.2	48.9	1.06	1.498	18.6	1.29
860.2	47.1	1.08	1.519	17.8	1.27
880.6	42.9	1.03	1.539	18.0	1.31
900.1	41.8	1.05	1.560	17.5	1.31
903.7	41.7	1.05	1.579	17.5	1.35
921.9	39.7	1.04	1.600	16.9	1.34
941.8	37.7	1.03	1.620	17.0	1.38
960.8	35.5	1.01	1.639	16.7	1.39
981.0	34.1	1.01	1.658	17.0	1.44
1002	33.4	1.04	1.679	16.9	1.47
1022	32.2	1.04	1.698	16.1	1.44
1042	30.7	1.03	1.718	15.9	1.45
1061	30.0	1.04	1.738	15.6	1.46
1081	28.8	1.04	1.758	15.2	1.45
1102	27.3	1.02	1.778	15.1	1.49
1122	26.8	1.04	1.798	15.1	1.51

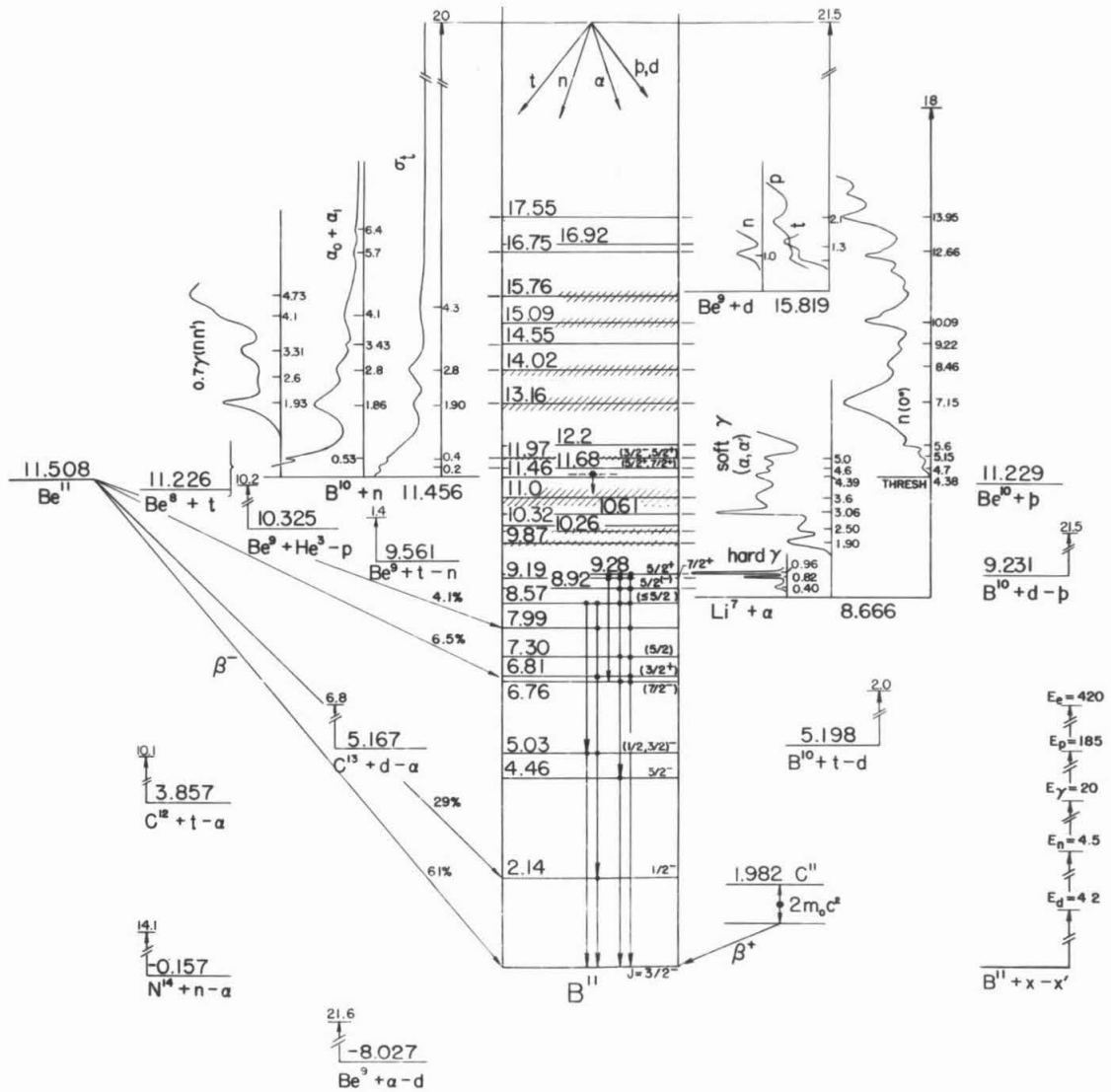
B11
11.508
Be11
11.226
Be8 + t
10.325
Be9 + He3 - p
9.561
Be9 + t - n
B10 + n 11.456
Be9 + d 15.819
Li7 + α 8.666
11.229
Be10 + p
9.231
B10 + d - p
5.198
B10 + t - d
5.167
C13 + d - α
3.857
C12 + t - α
-0.157
N14 + n - α
-8.027
Be9 + α - d
1.982 C11
2mec2
β−
β+
4.1%
6.5%
29%
61%
17.55
16.92
16.75
15.76
15.09
14.55
14.02
13.16
12.2
11.97
11.68
11.46
11.0
10.61
10.32
10.26
9.87
9.28
9.19
8.92
8.57
7.99
7.30
6.81
6.76
5.03
4.46
2.14
J=3/2−
hard γ
soft γ
(α, αʹ)
n (0°)
THRESH
Ee=420
Ep=185
Eγ=20
En=4.5
Ed=4.2
B11 + x - xʹ

Figure 1

Energy Levels of B^{11}

The bombardment of Be^{9} by deuterons forms B^{11} as a compound nucleus. The energy levels of this nucleus are shown on the opposite page. The excitation region above 15.819 Mev was investigated in this experiment. Note that the deuteron binding energy in B^{11} is considerably higher than the binding energies for other light particles.

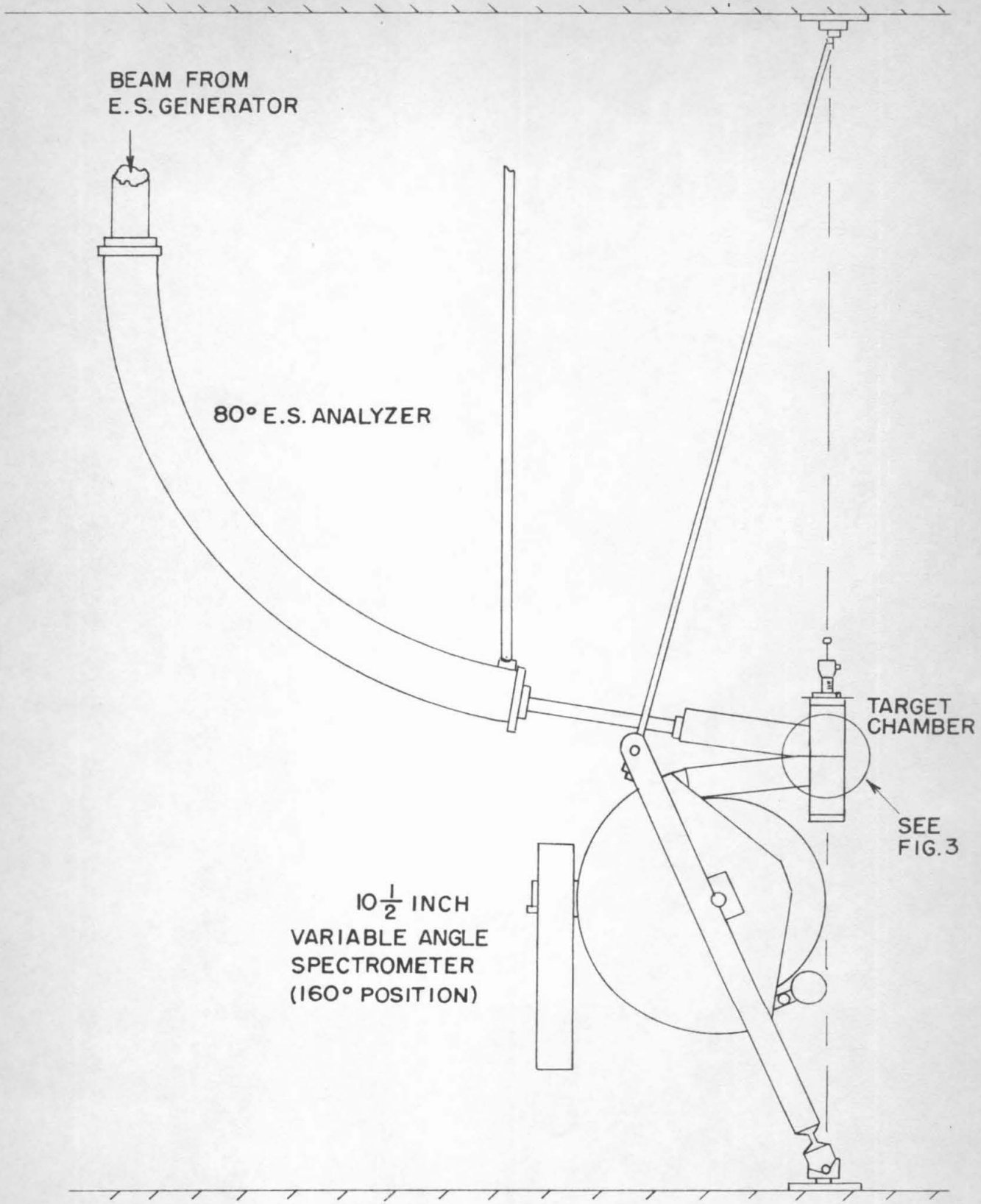
BEAM FROM
E.S. GENERATOR
80° E.S. ANALYZER
TARGET
CHAMBER
SEE
FIG. 3
10 1/2 INCH
VARIABLE ANGLE
SPECTROMETER
(160° POSITION)

Figure 2

Layout of the Experimental Equipment

The layout of the equipment used in this experiment is shown in this figure. Descriptions of the various components may be found in Part II of the text.

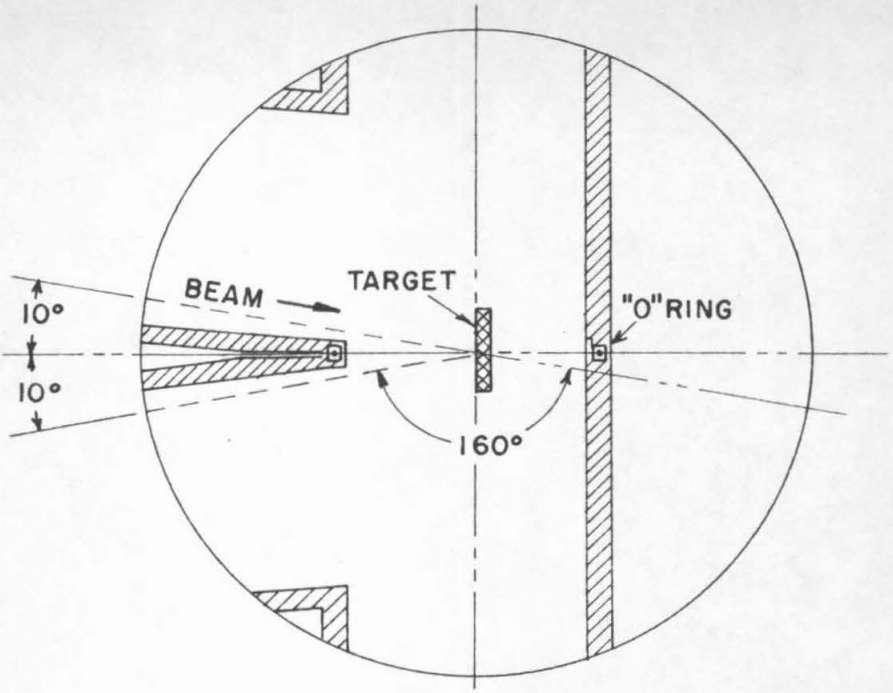

160° POSITION

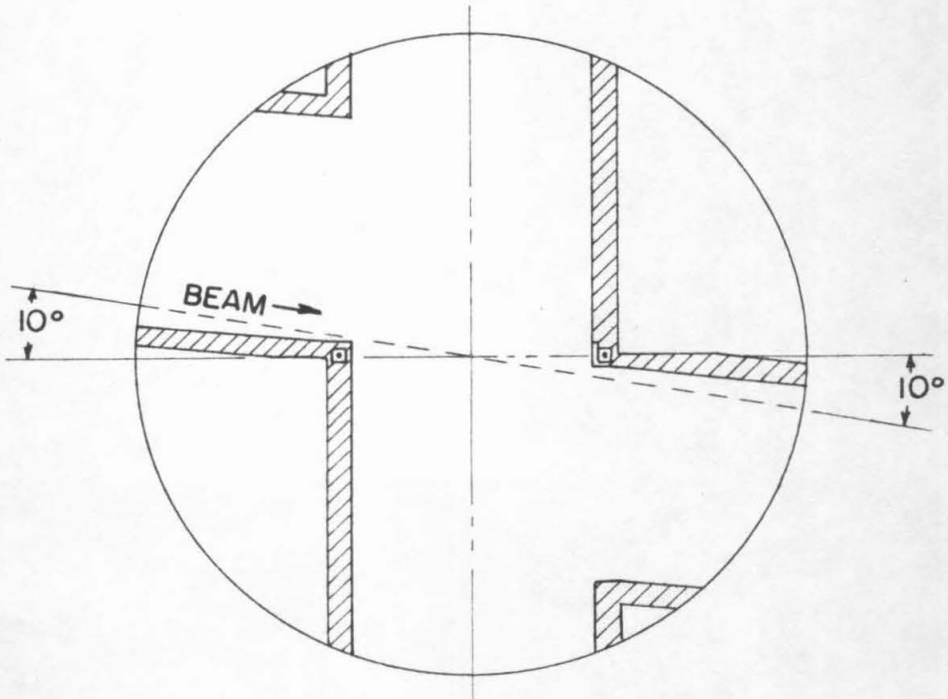

0° POSITION

Figure 3

Target Chamber Detail

This figure shows the geometry of the target chamber and the paths of the incoming and scattered particles relative to the scattering target. See p. 4 of the text.

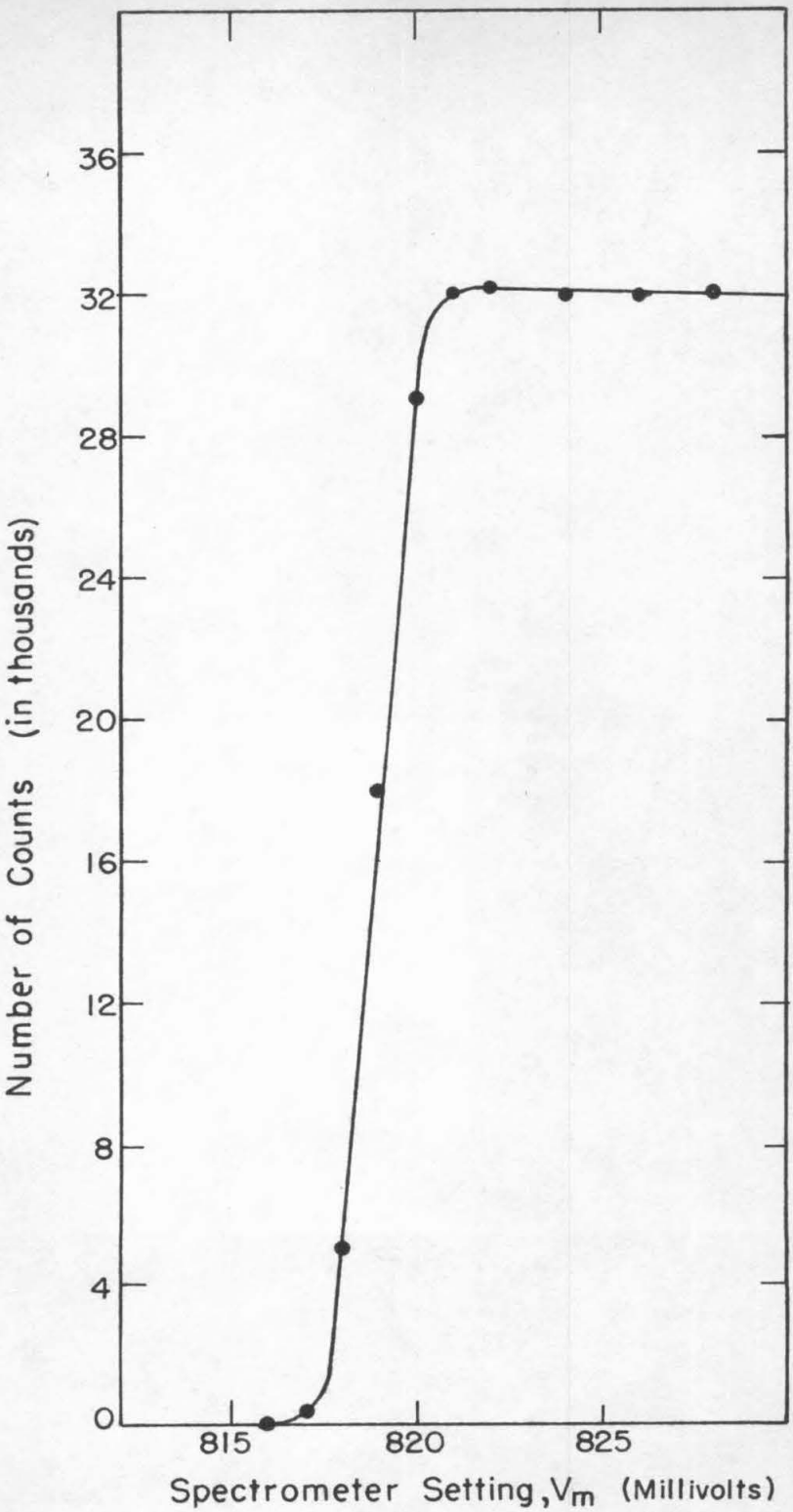
36
32
28
24
20
16
12
8
4
0
Number of Counts (in thousands)
815
820
825
Spectrometer Setting, V_m (Millivolts)

Figure 4

Cu(p,p)Cu Target Profile

This target profile is typical of the profiles obtained from thick copper targets. It was taken with E_{lB} = 0.6028 Mev and $\Theta_L = 158^{\circ}\ 53$. Since the momentum of the analyzed particles varies inversely with V_m, the abscissa energy scale increases to the left. The use of profiles such as this to determine the solid angle and calibration constant for the magnetic spectrometer is discussed on p. 7 and p. 16 of the text.

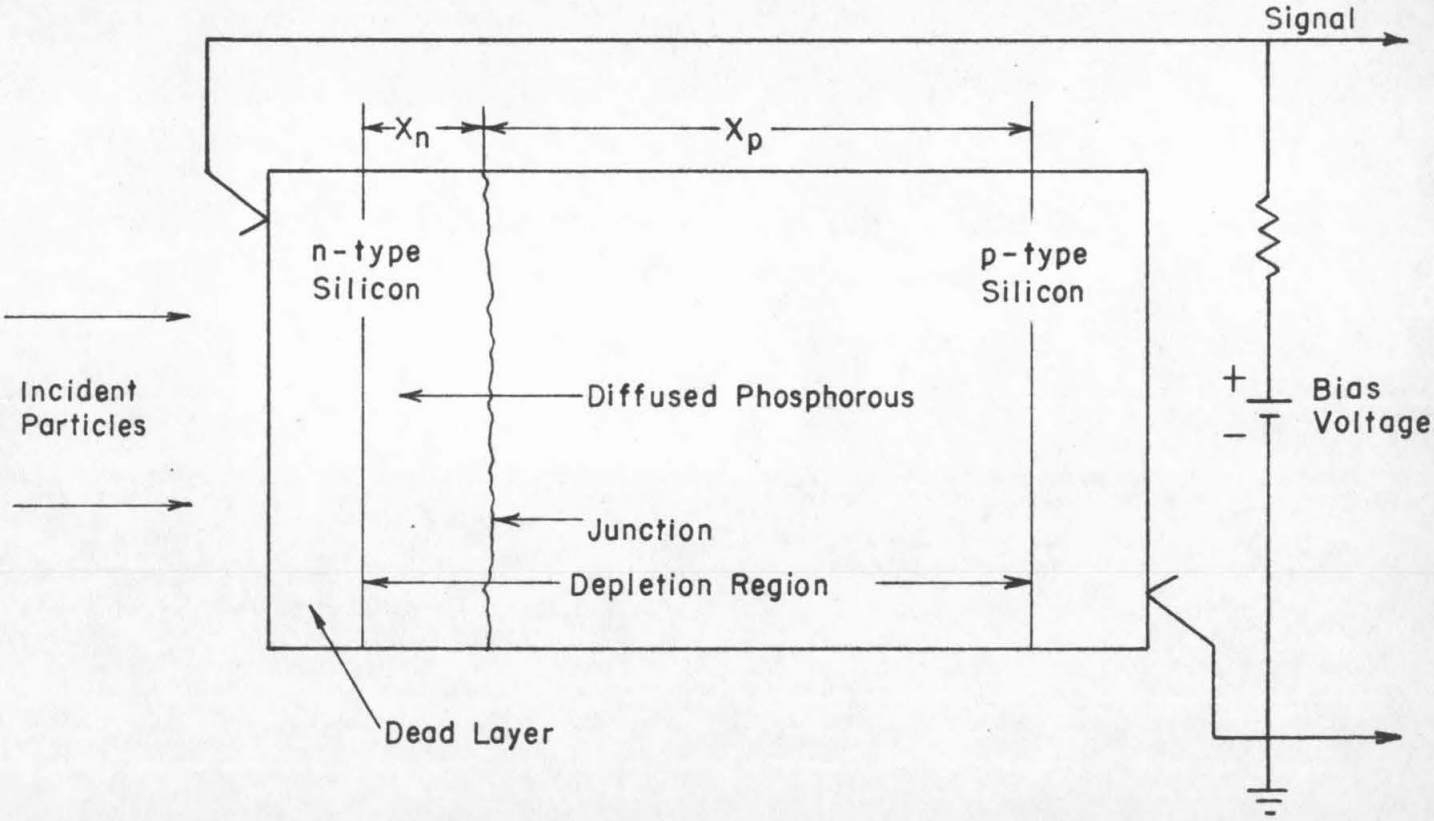
Signal
X_n
X_p
n-type
Silicon
p-type
Silicon
Incident
Particles
Diffused Phosphorous
+
−
Bias
Voltage
Junction
Depletion Region
Dead Layer

Figure 5

Essential Features of the p-n Junction Detector

The physical processes which occur within the detector when incident charged particles are being observed are described on p. 8 of the text.

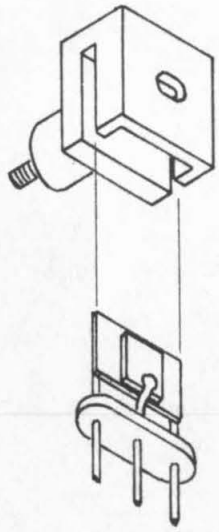

Detector Holder

Detector

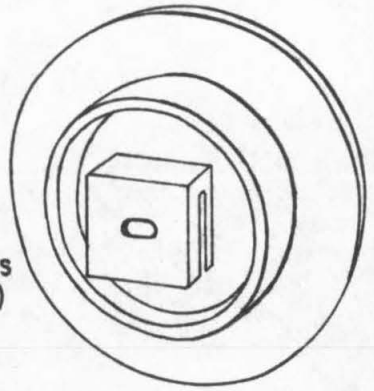

Assembly
(Signal leads
not shown)

Figure 6

Detector Holder

The holder to which the detector was attached and the flange which was placed in the output port of the magnetic spectrometer are shown here. The detector was attached first to the holder, and the holder was then joined to the flange as shown in the assembly. The connector for the detector-output lead is on the back side of the flange.

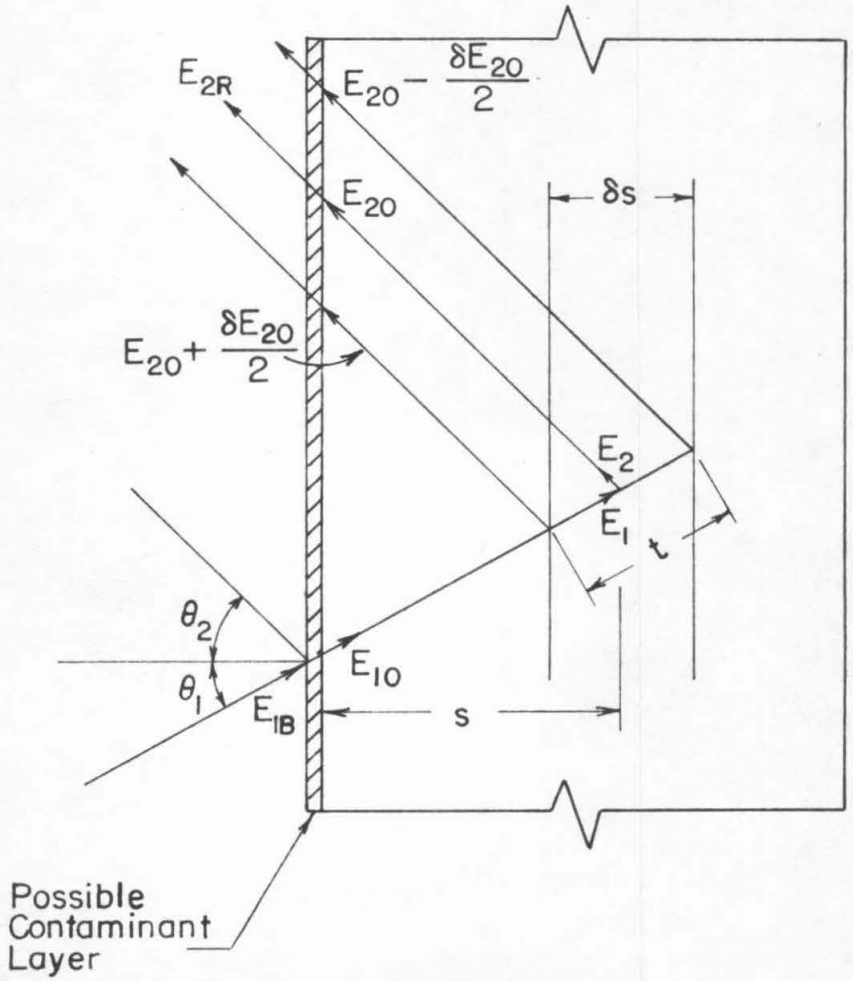
E_{2R}
$E_{20} - \frac{\delta E_{20}}{2}$
E_{20}
δs
$E_{20} + \frac{\delta E_{20}}{2}$
E_2
E_1
t
θ_2
θ_1
E_{10}
E_{1B}
s
Possible
Contaminant
Layer

Figure 7

Thick-Target Reaction Geometry

The various energies and angles necessary for a detailed description of the reaction process are shown in this figure. For given values of E_{1B} and Θ_L, the magnetic spectrometer determines the depth of the lamina from which the observed reaction products originate. For the sake of clarity, the width of the reaction lamina relative to the width of the target is exaggerated. See pp. 9 and 10 of the text for an explanation of the quantities shown in this illustration.

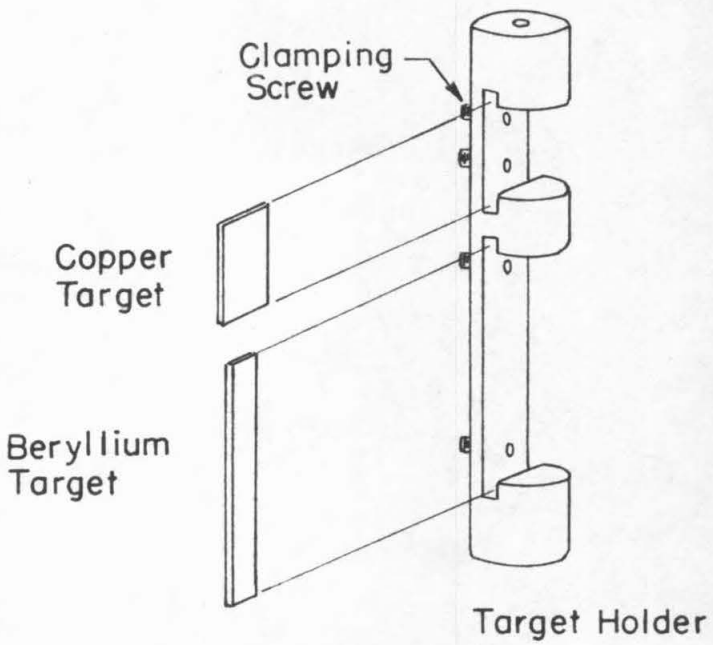
Clamping
Screw
Copper
Target
Beryllium
Target
Target Holder

Figure 8

Target Holder

The target holder which permitted simultaneous mounting of two targets is pictured here. The targets are held in place by pressure applied to their back sides by the clamping screws. The target holder is positioned in the target chamber by attaching the upper end of the holder to the orientation rod which extends through the top of the target chamber. See p. 17 of the text.

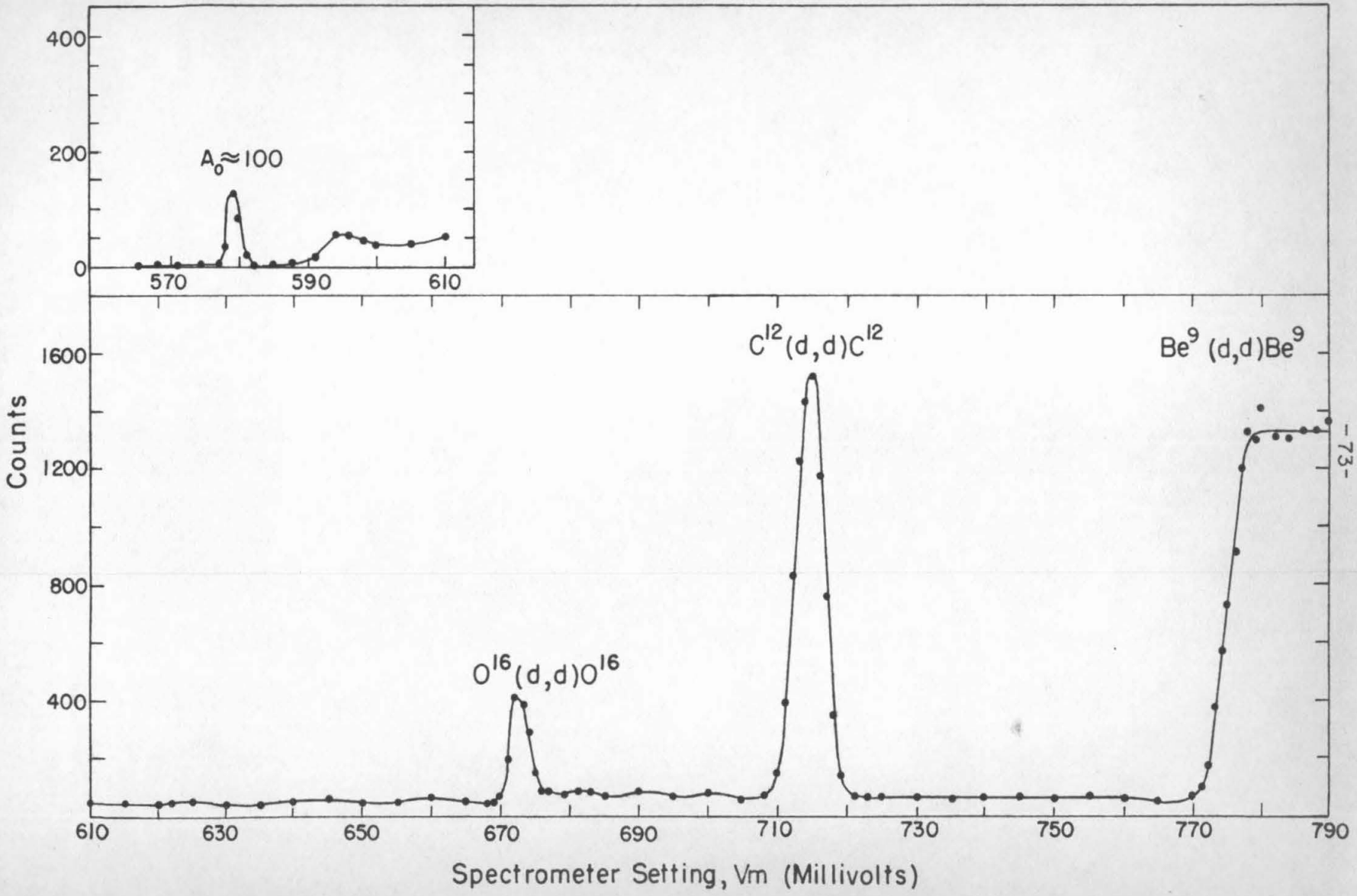
400
200
0
$A_0 \approx 100$
570
590
610
1600
1200
800
400
Counts
$C^{12}(d,d)C^{12}$
Be^9 (d,d)Be^9
$O^{16}(d,d)O^{16}$
610
630
650
670
690
710
730
750
770
790
Spectrometer Setting, Vm (Millivolts)

Figure 9

Profile of the Scattering Target

This figure shows the scattering profile produced by the beryllium target and the associated contaminants. For this particular profile, E_{1B} = 0.6028 Mev and $\Theta_L = 113^\circ\ 26'$. Scattering by carbon and oxygen is clearly apparent. The constant background beginning at V_m = 592 may be due to an impurity distributed within the target which has a mass number of about 57. See p. 18 of the text.

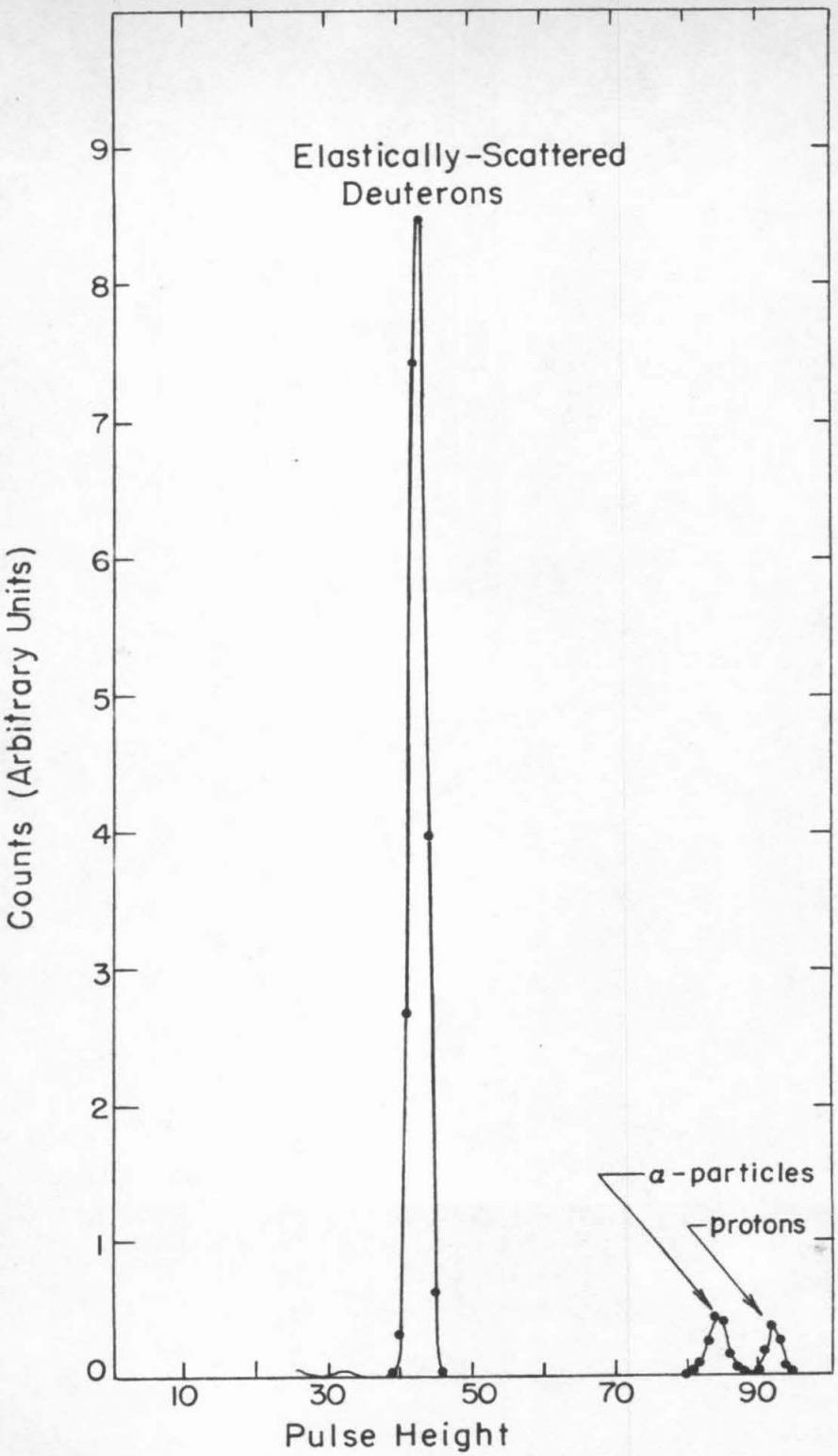
Elastically-Scattered
Deuterons
α-particles
protons
Counts (Arbitrary Units)
Pulse Height
0
1
2
3
4
5
6
7
8
9
10
30
50
70
90

Figure 10

Pulse-Height Spectrum of the Detector Output

Shown in this figure is the detector output spectrum produced by the particles resulting from Be^9 + d which pass through the magnetic spectrometer. This spectrum was recorded when E_{1B} = 1.206 Mev, $\Theta_L = 77^\circ\ 24'$, and E_{20} = 0.8104 Mev for the deuterons. Although the protons and doubly-charged alpha particles which pass through the spectrometer both have the same energy, the alpha particles lose more energy in passing through the detector dead layer than do the protons. This means that the alpha particles produce slightly smaller pulses than do the protons. In order to decrease the amount of multichannel analyzer dead time, the low-energy noise pulses were biased out by suitably adjusting the low-energy detection level of the analyzer. See pp. 19 and 20 of the text.

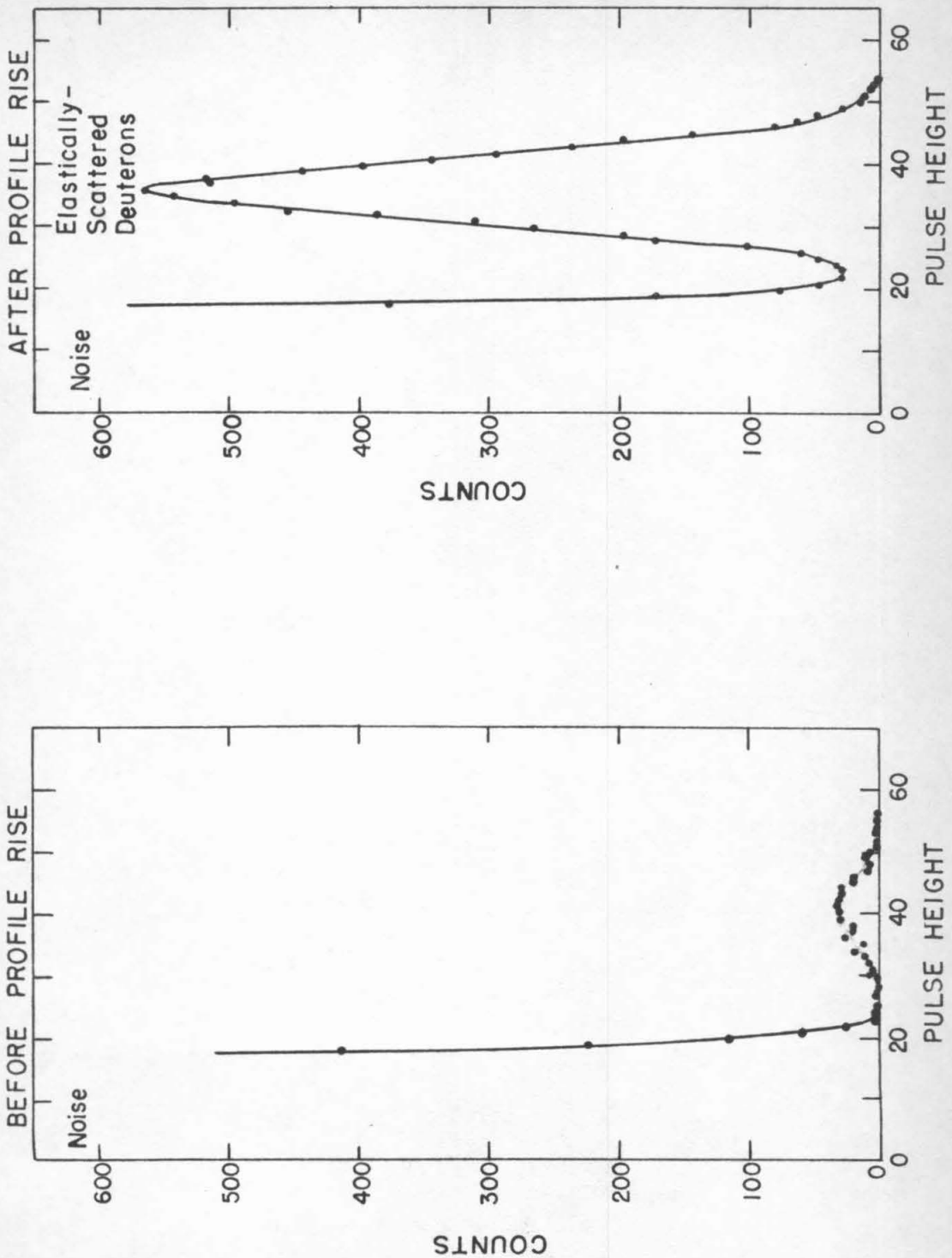
BEFORE PROFILE RISE
Noise
AFTER PROFILE RISE
Elastically-
Scattered
Deuterons
Noise
COUNTS
PULSE HEIGHT
0
100
200
300
400
500
600
20
40
60

Figure 11

Output Spectrum Produced by Low-Energy Deuterons

This figure shows a detector-output spectrum typical of the kind used to determine the scattering yields at low bombarding energies. In this case E_{1B} = 0.3617 Mev, $\Theta_L = 77^\circ\ 24'$, and E_{20} = 0.2456 Mev. The spectrum taken with V_m set before the profile rise shows the noise spectrum and the spectrum of background deuterons scattered by impurities within the target. Under the conditions existing here, the noise subtraction is easily accomplished. See p. 20 of the text.

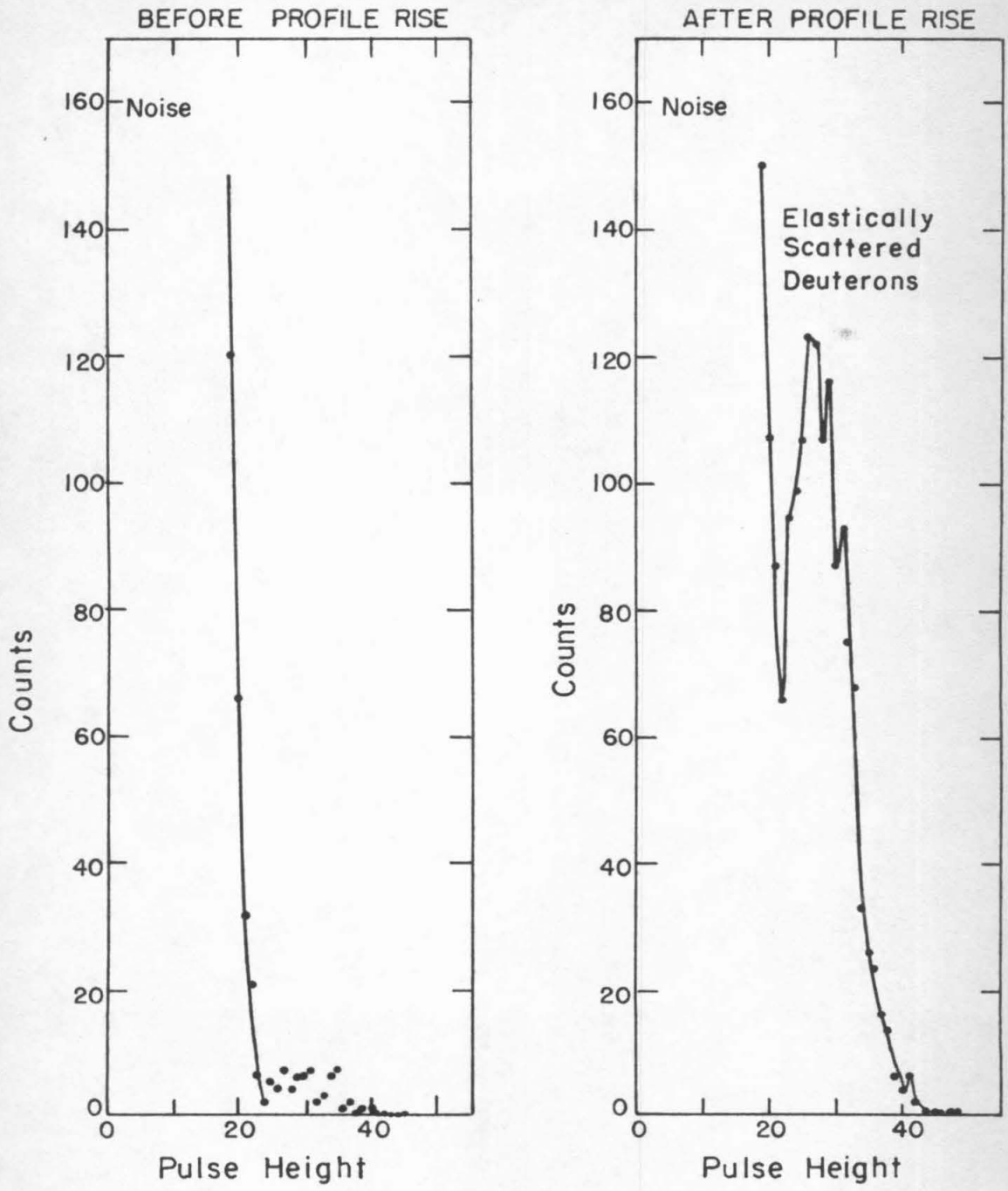
BEFORE PROFILE RISE
Noise
160
140
120
100
80
60
40
20
0
Counts
0
20
40
Pulse Height
AFTER PROFILE RISE
Noise
Elastically
Scattered
Deuterons
160
140
120
100
80
60
40
20
0
Counts
0
20
40
Pulse Height

Figure 12

Output Spectrum Produced by Low-Energy Deuterons

This is a detector-output spectrum obtained at low bombarding energy. The relevant experimental quantities were E_{1B} = 0.4019 Mev, $\Theta_L = 113^\circ\ 26'$, and E_{20} = 0.2090 Mev. In this case the noise subtraction is complicated by the substantial overlap of signal and noise. A maximum uncertainty in the yield of eight percent was attributed to the signal-noise unfolding procedure. See pp. 20 and 28 of the text.

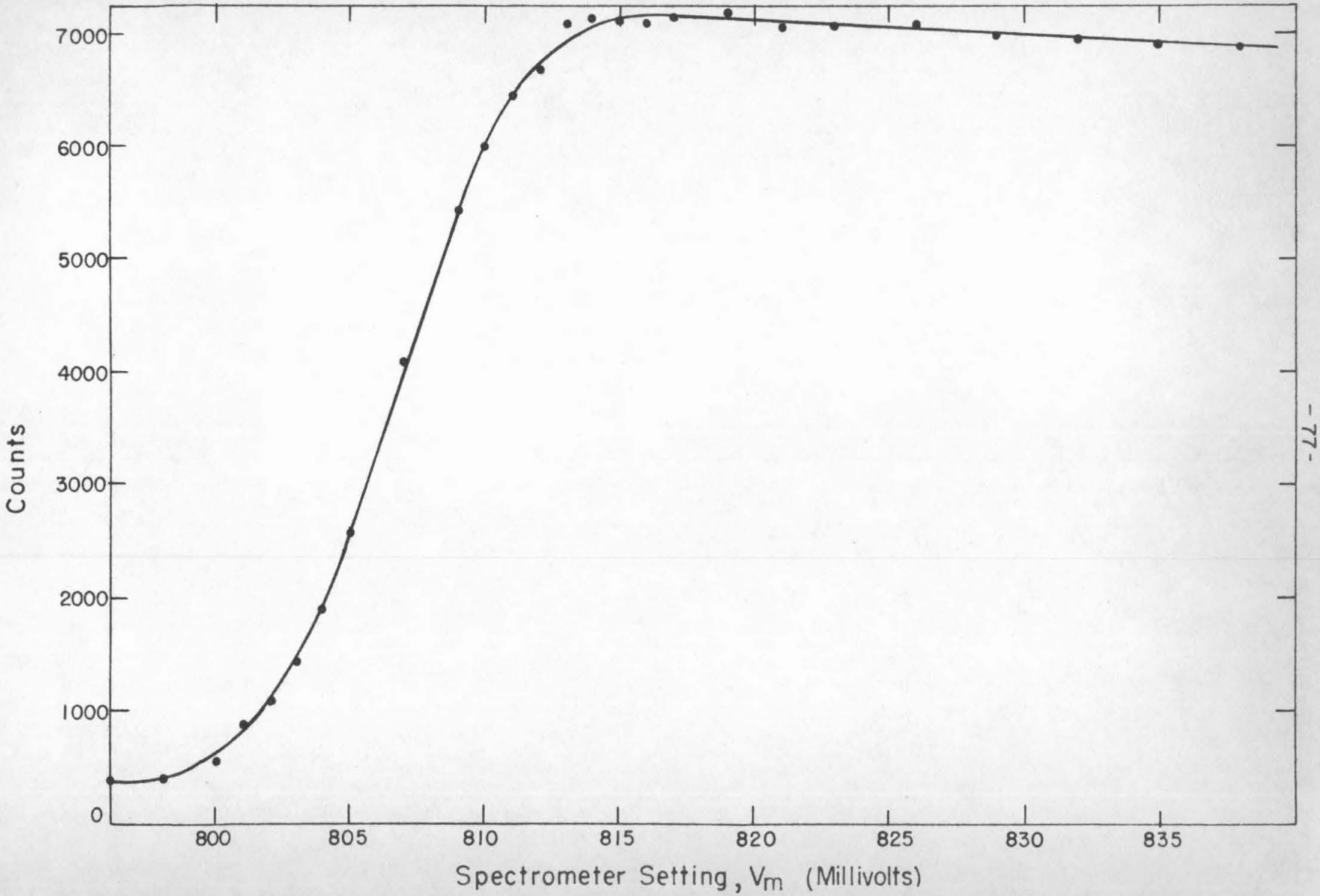
Counts
7000
6000
5000
4000
3000
2000
1000
0
800
805
810
815
820
825
830
835
Spectrometer Setting, V_m (Millivolts)

Figure 13

$Be^9(d,d)Be^9$ Target Profile

This profile was obtained with E_{1B} = 0.4220 Mev and $\Theta_L = 77^\circ\ 24'$. The counts observed at each setting of V_m have not been corrected for dead-time or charge-neutralization effects. See p. 21 of the text.

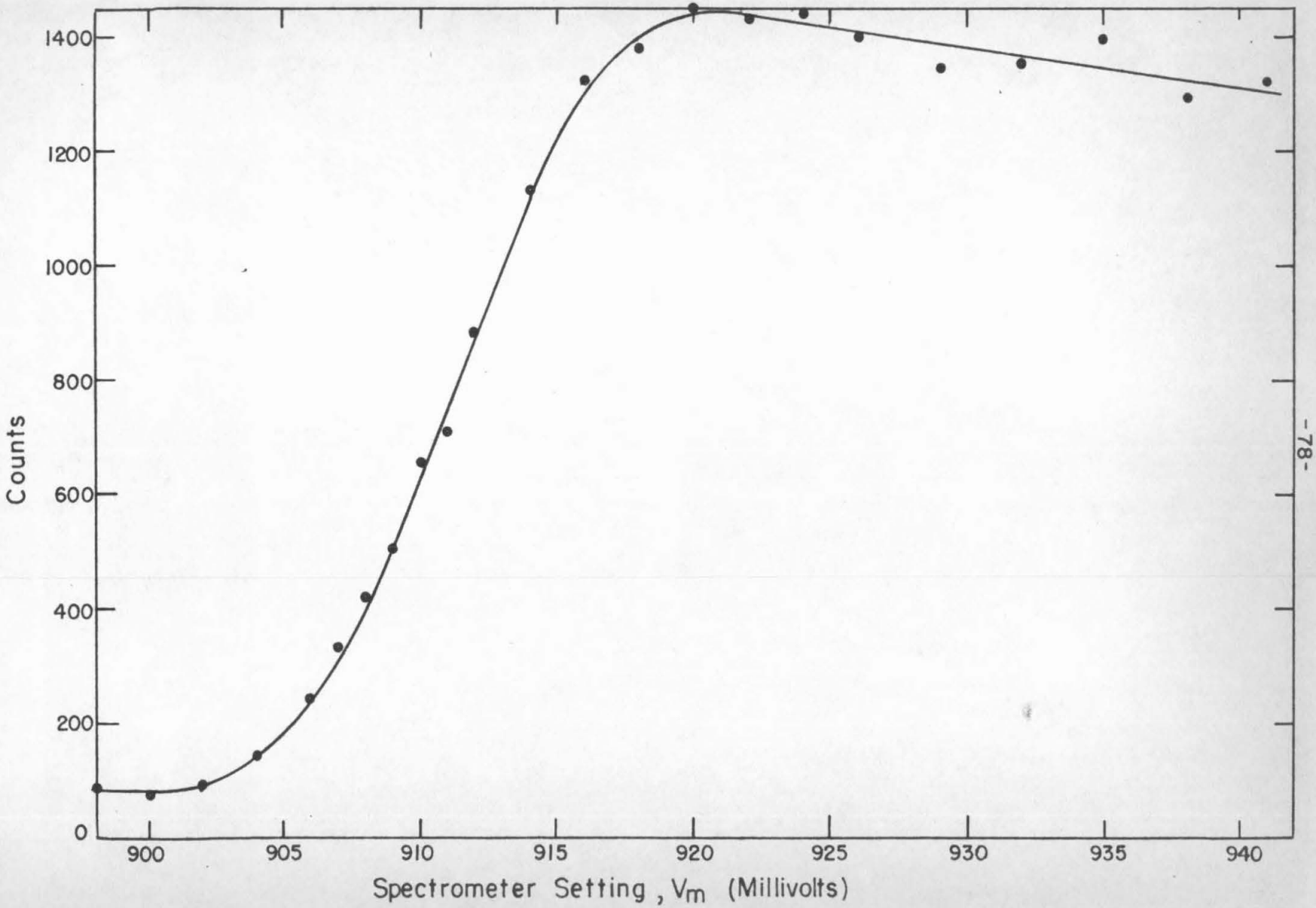
Counts
0
200
400
600
800
1000
1200
1400
900
905
910
915
920
925
930
935
940
Spectrometer Setting , V_m (Millivolts)

Figure 14

$Be^9(d,d)Be^9$ Target Profile

This profile was obtained with E_{lB} = 0.4421 Mev, and $\Theta_L = 113^\circ\ 26'$. The counts observed at each setting of V_m have not been corrected for dead-time or charge-neutralization effects. See p. 21 of the text.

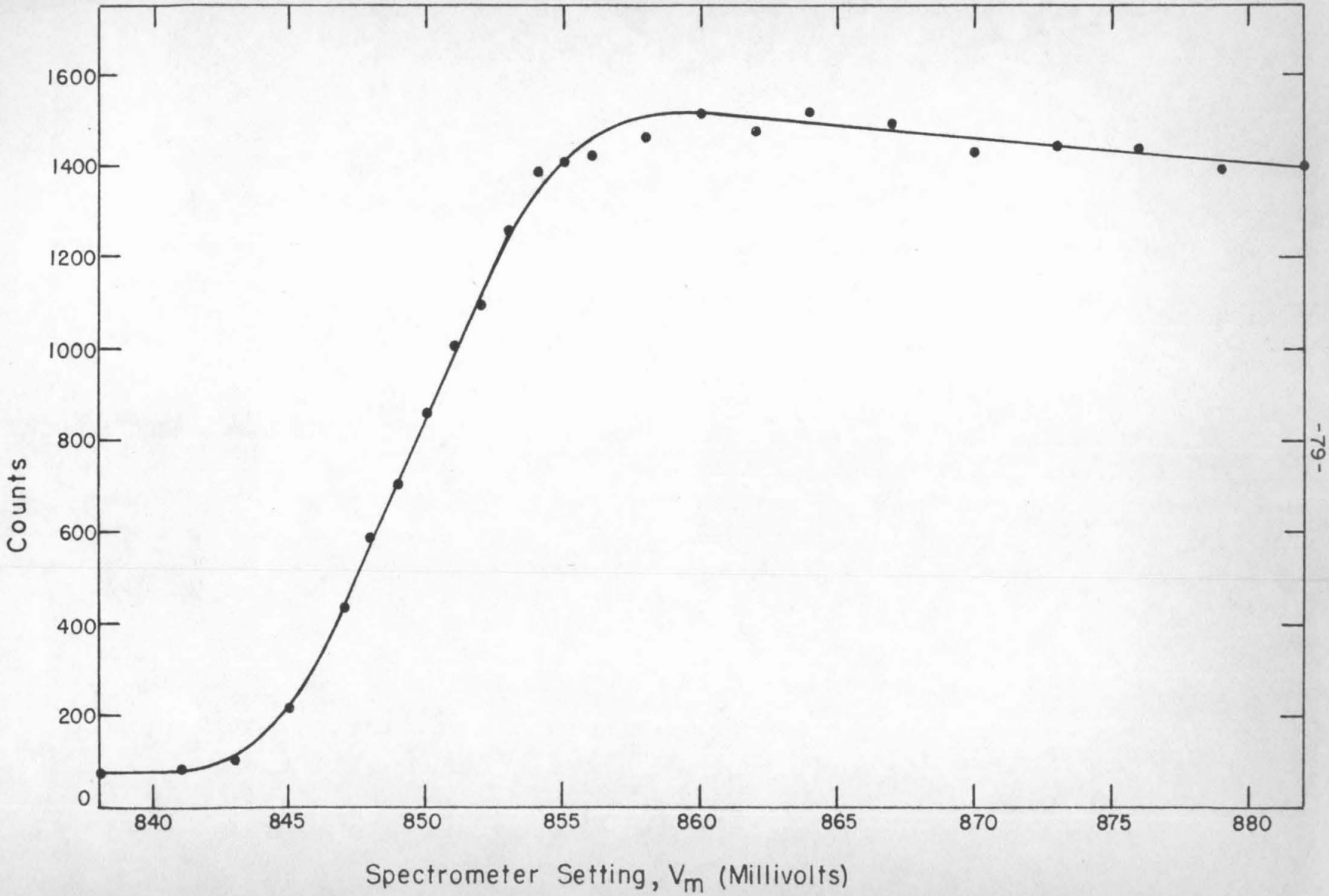
1600
1400
1200
1000
800
600
400
200
0
Counts
840
845
850
855
860
865
870
875
880
Spectrometer Setting, V_m (Millivolts)

Figure 15

$Be^9(d,d)Be^9$ Target Profile

This profile was obtained with E_{1B} = 0.5024 Mev, and $\Theta_L = 113^\circ 26'$. The counts observed at each setting of V_m have not been corrected for dead-time or charge-neutralization effects. See p. 21 of the text.

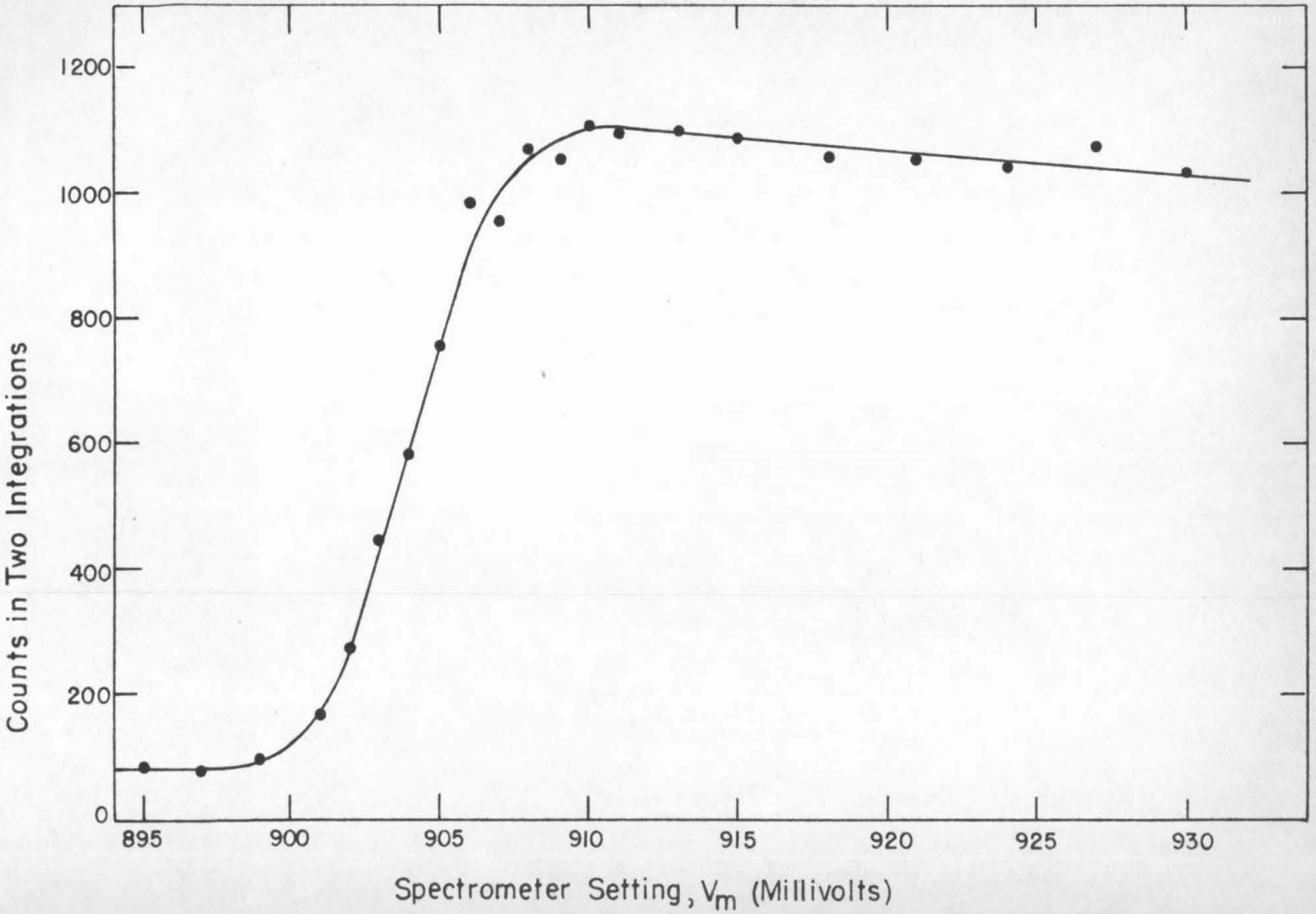
Counts in Two Integrations
0
200
400
600
800
1000
1200
895
900
905
910
915
920
925
930
Spectrometer Setting, V_m (Millivolts)

Figure 16

$Be^9(d,d)Be^9$ Target Profile

This profile was obtained with $E_{lB} = 0.5626$ Mev and $\Theta_L = 158^\circ 53'$. The counts observed at each setting of V_m have not been corrected for dead-time or charge-neutralization effects. See p. 21 of the text.

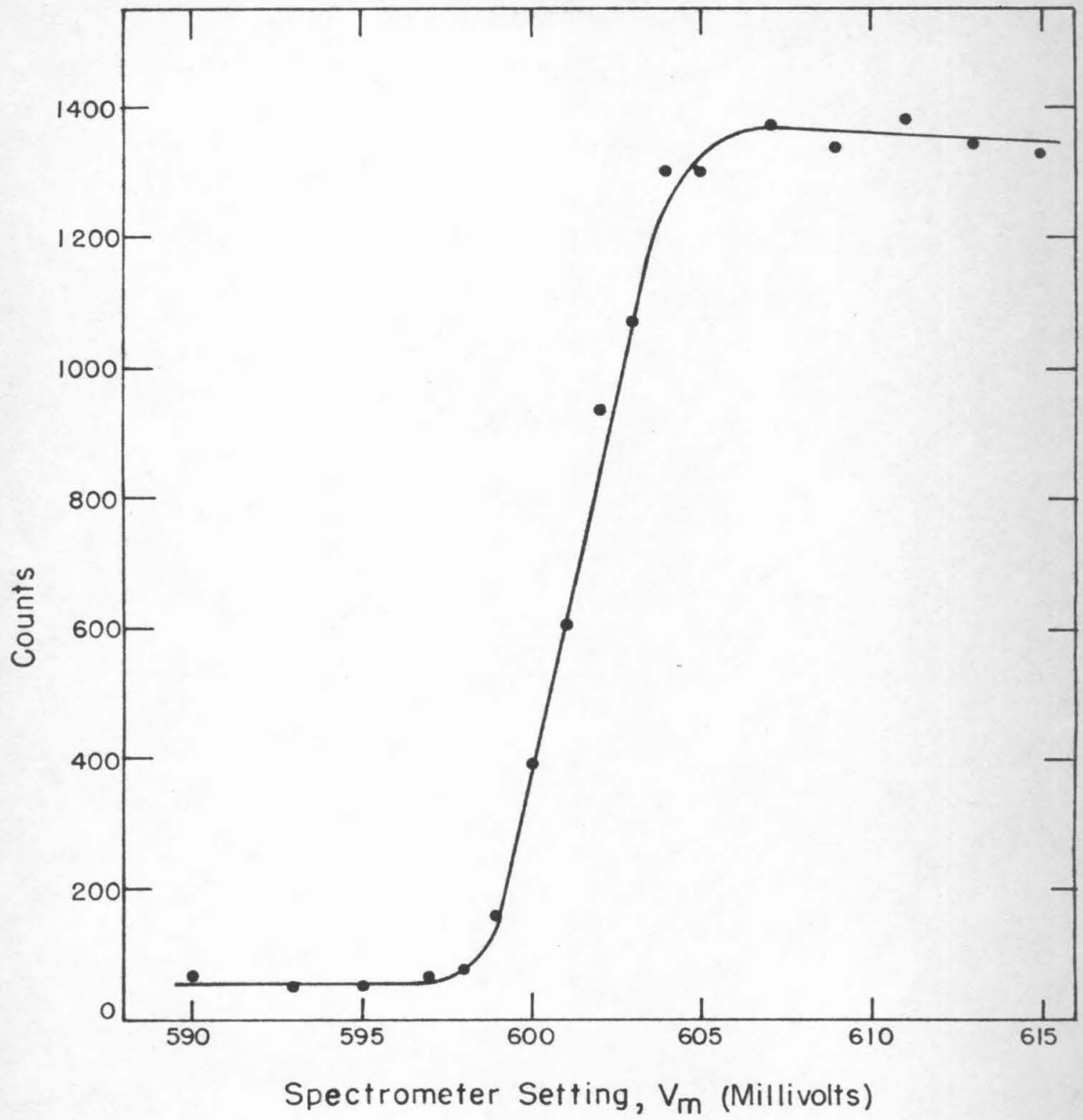
1400
1200
1000
800
600
400
200
0
Counts
590
595
600
605
610
615
Spectrometer Setting, V_m (Millivolts)

Figure 17

$Be^9(d,d)Be^9$ Target Profile

This profile was obtained with E_{1B} = 1.005 Mev and Θ_L = 113° 26'. The deuteron yield obtained from this profile is used in the sample calculation shown in Appendix I. In this case the dead-time and charge-neutralization corrections are negligible. See p. 21 of the text and Appendix I.

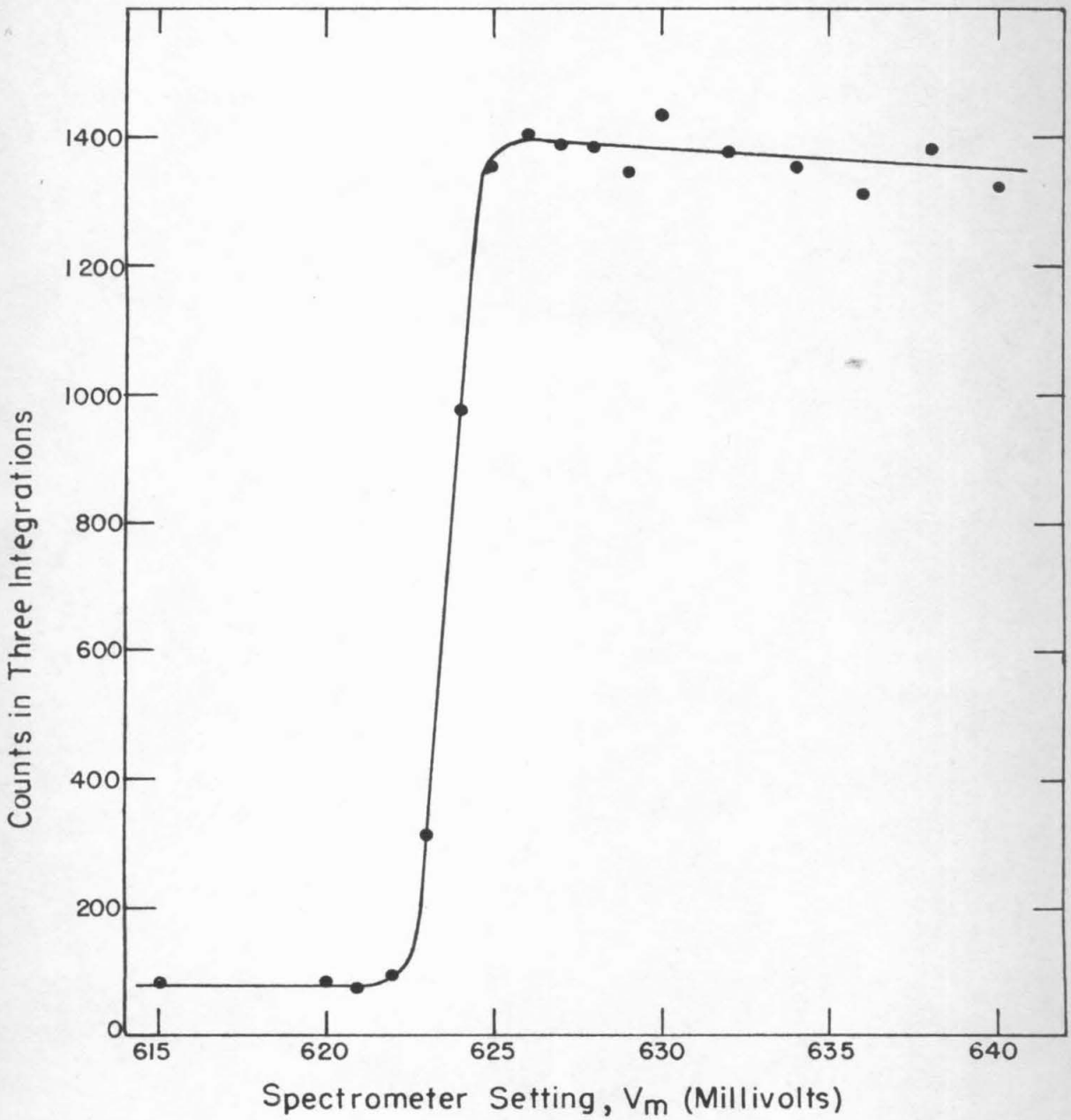
1400
1200
1000
800
600
400
200
0
Counts in Three Integrations
615
620
625
630
635
640
Spectrometer Setting, V_m (Millivolts)

Figure 18

$Be^9(d,d)Be^9$ Target Profile

This profile was obtained with E_{1B} = 1.186 Mev and $\Theta_L = 158^\circ\ 53'$. Dead-time and charge-neutralization corrections are negligible. See p. 21 of the text.

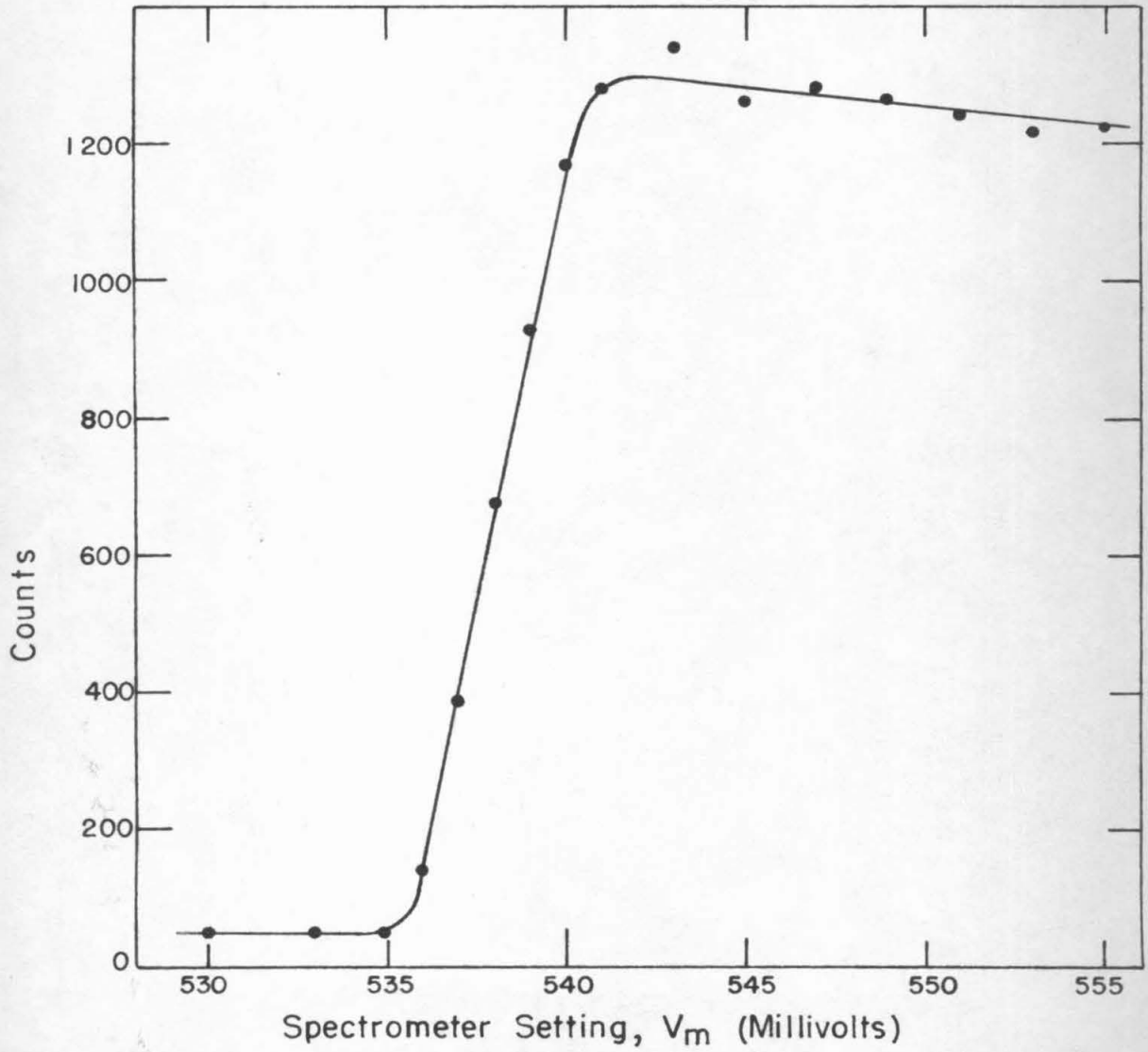
Counts
1200
1000
800
600
400
200
0
530
535
540
545
550
555
Spectrometer Setting, V_m (Millivolts)

Figure 19

$Be^9(d,d)Be^9$ Target Profile

This profile was obtained with E_{1B} = 1.256 Mev and $\Theta_L = 113^\circ\ 26'$. Dead-time and charge-neutralization corrections are negligible. See p. 21 of the text.

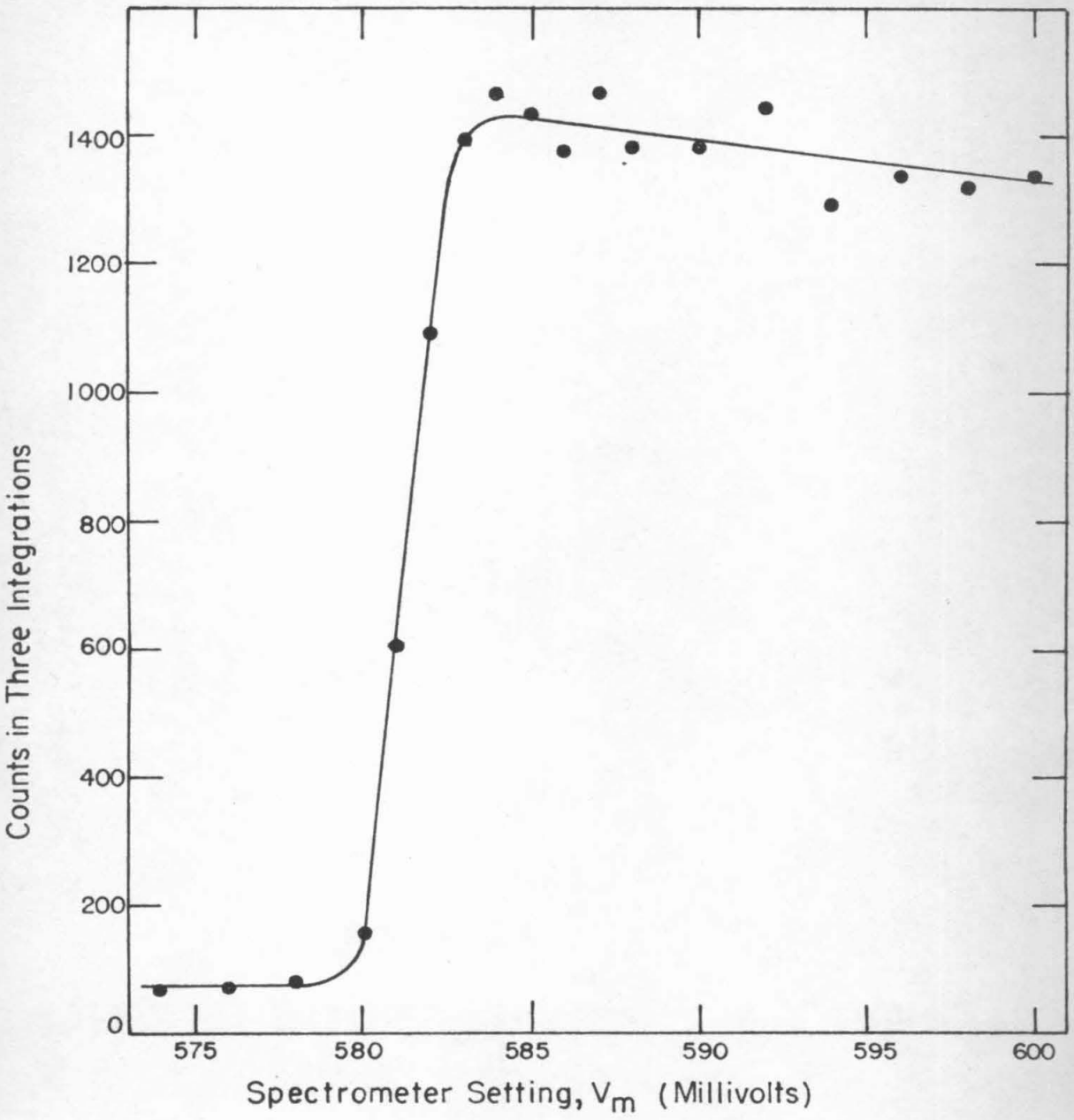
Counts in Three Integrations
0
200
400
600
800
1000
1200
1400
575
580
585
590
595
600
Spectrometer Setting, V_m (Millivolts)

Figure 20

$Be^9(d,d)Be^9$ Target Profile

This profile was obtained with E_{lB} = 1.366 Mev and Θ_L = 158° 53'. Dead-time and charge-neutralization corrections are negligible. See p. 21 of the text.

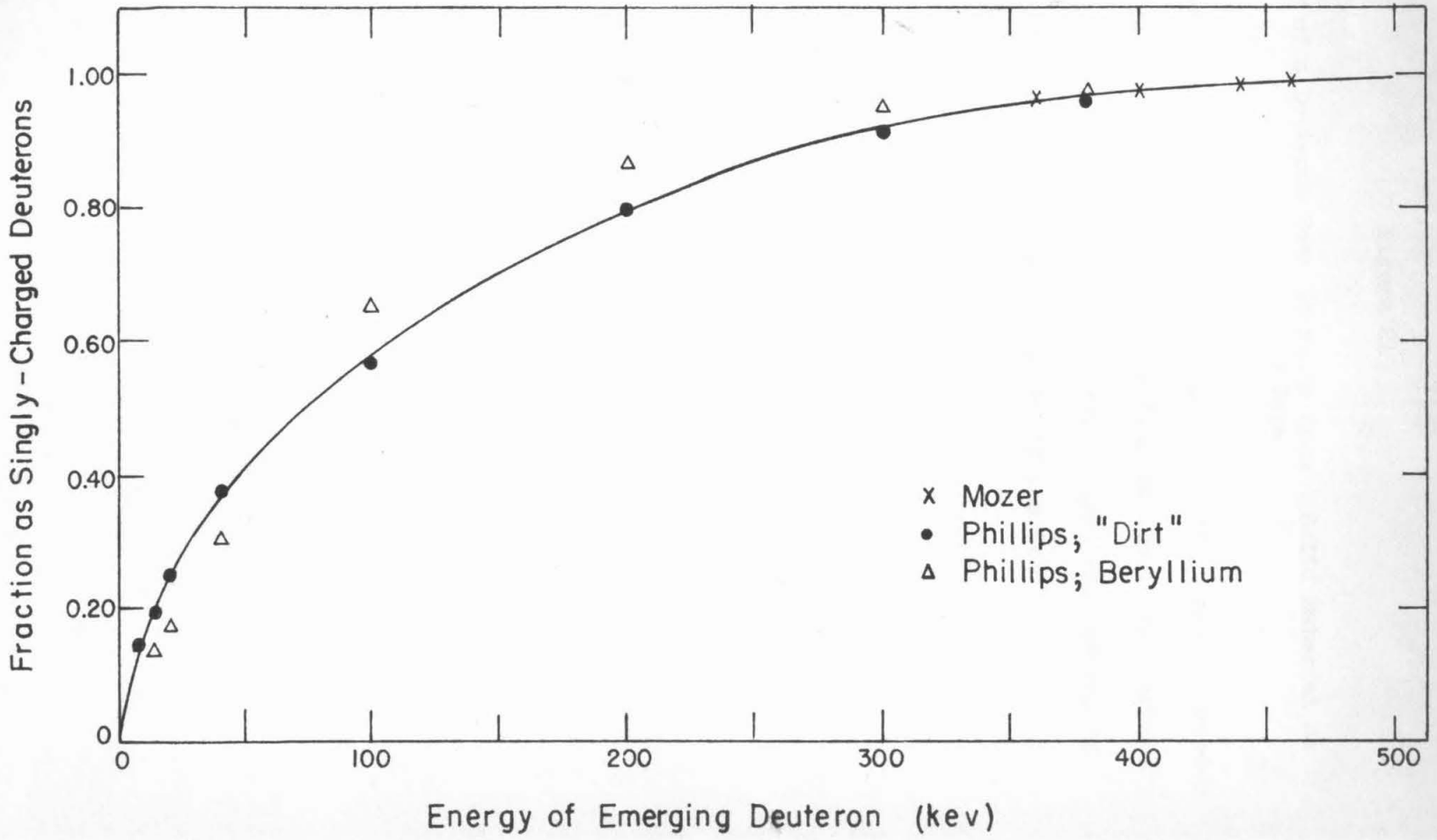
Fraction as Singly-Charged Deuterons
1.00
0.80
0.60
0.40
0.20
0
0
100
200
300
400
500
Energy of Emerging Deuteron (kev)
x Mozer
• Phillips; "Dirt"
Δ Phillips; Beryllium

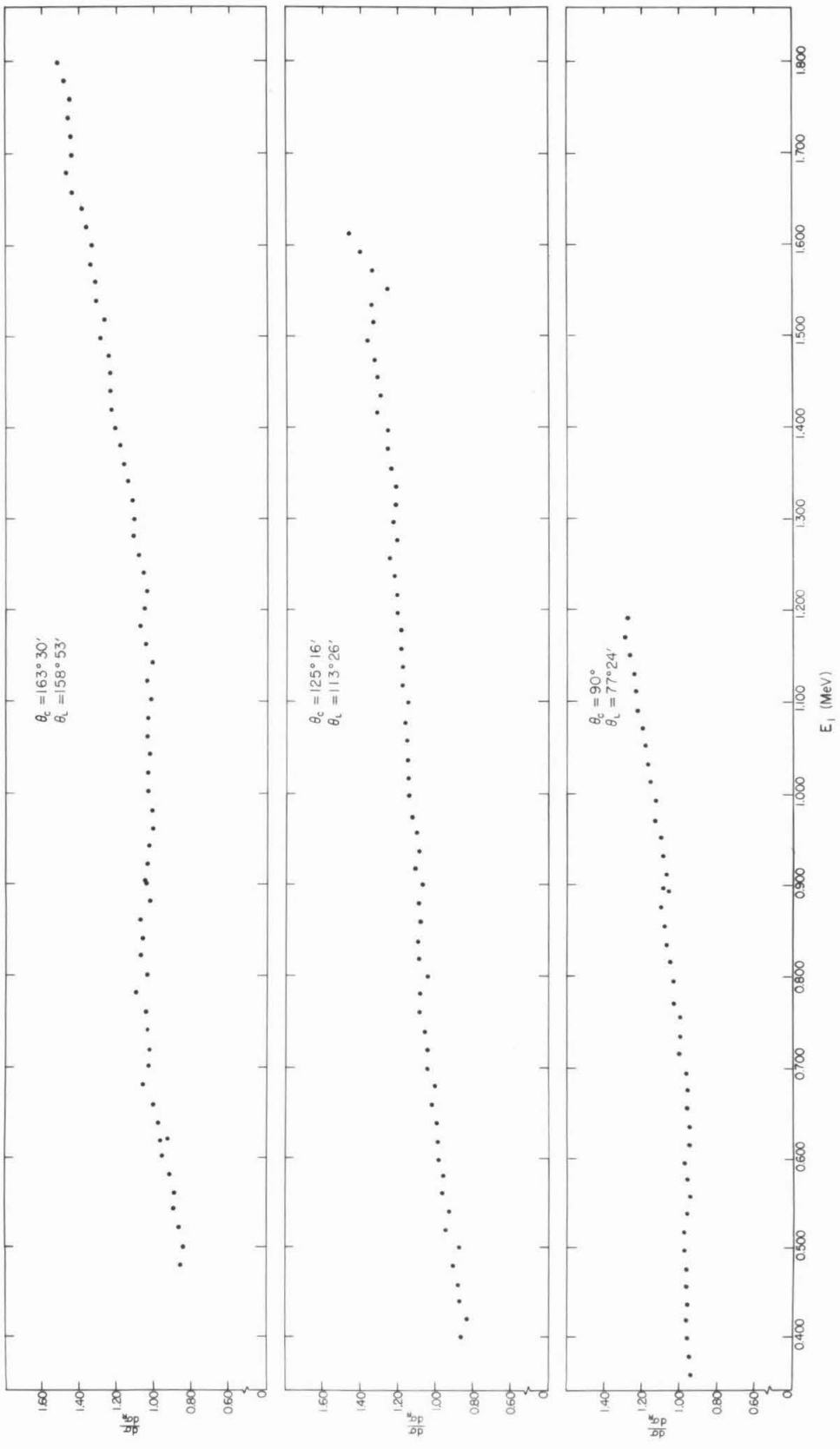
$\theta_c = 163° 30'$
$\theta_L = 158° 53'$
$\theta_c = 125° 16'$
$\theta_L = 113° 26'$
$\theta_c = 90°$
$\theta_L = 77° 24'$
$\frac{d\sigma}{d\sigma_R}$
$\frac{d\sigma}{d\sigma_R/q}$
$\frac{d\sigma}{d\sigma_R/q}$
0.60
0.80
1.00
1.20
1.40
1.60
0
0.400
0.500
0.600
0.700
0.800
0.900
1.000
1.100
1.200
1.300
1.400
1.500
1.600
1.700
1.800
E_1 (MeV)

Figure 22

The Ratio of the Experimental $Be^9(d,d)Be^9$ Differential Cross Section to the Rutherford Cross Section

The result of dividing the experimentally-observed cross sections by the Rutherford values is shown here. The relative and absolute fractional standard deviations in $d\sigma/d\sigma_R$ are about 2.9 and 6.7 percent, respectively, over most of the range of bombarding energies. See pp. 27, 64a, 64b, and 64c of the text.

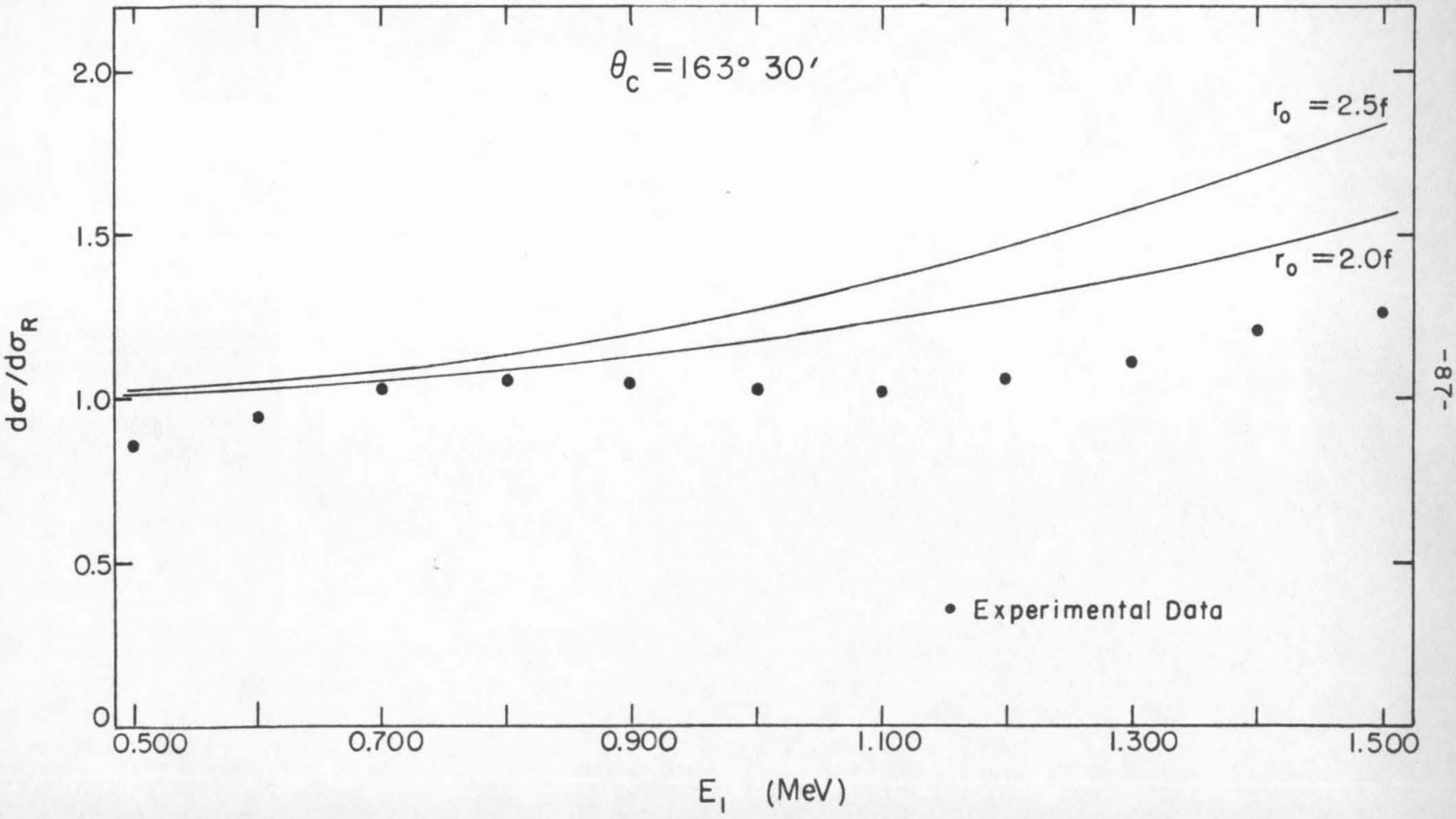
$\theta_c = 163° 30'$
$r_o = 2.5f$
$r_o = 2.0f$
• Experimental Data
$d\sigma/d\sigma_R$
E_1 (MeV)
2.0
1.5
1.0
0.5
0
0.500
0.700
0.900
1.100
1.300
1.500

Figure 23

Comparison of the Observed Cross Section with the Scattering Resulting from an Impenetrable Charged Sphere

This figure shows the scattering cross section calculated by assuming the target nuclei to be impenetrable charged spheres. The calculated result obviously is increasing with energy faster than the experimental cross section. See pp. 32 to 34 of the text.

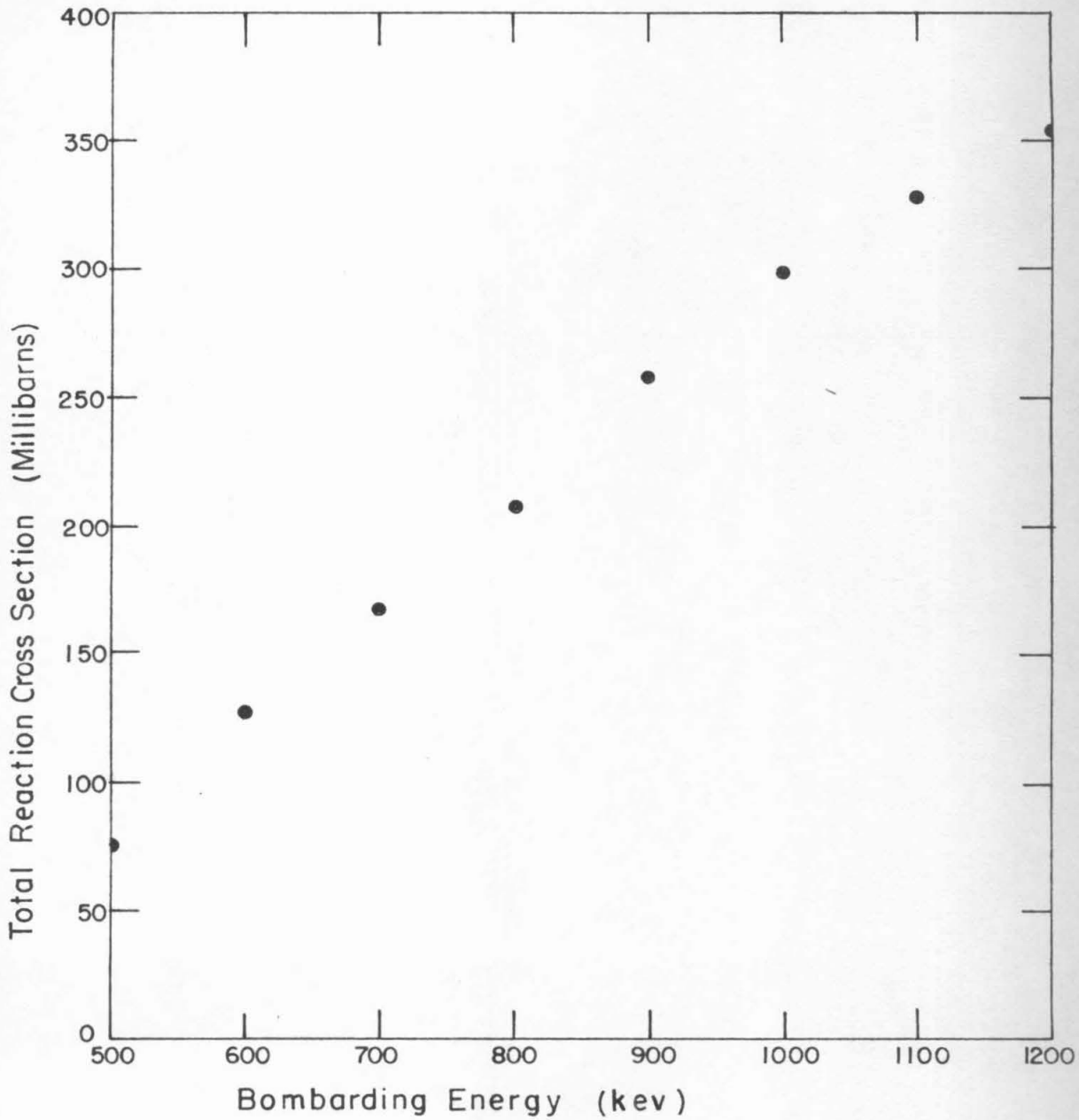
400
350
300
250
200
150
100
50
0
500
600
700
800
900
1000
1100
1200
Total Reaction Cross Section (Millibarns)
Bombarding Energy (kev)

Figure 24

Estimated Total Reaction Cross Section for Be^9 + d

These data were constructed from information found in the literature. The cross sections for several of the reaction channels have not been measured, so no contributions were included for these channels. Hence the composite result shown here must be considered a lower limit for the total reaction cross section. The uncertainty can only be guessed, but +50 percent and -20 percent seem to be reasonable limits. See p. 43 of the text.

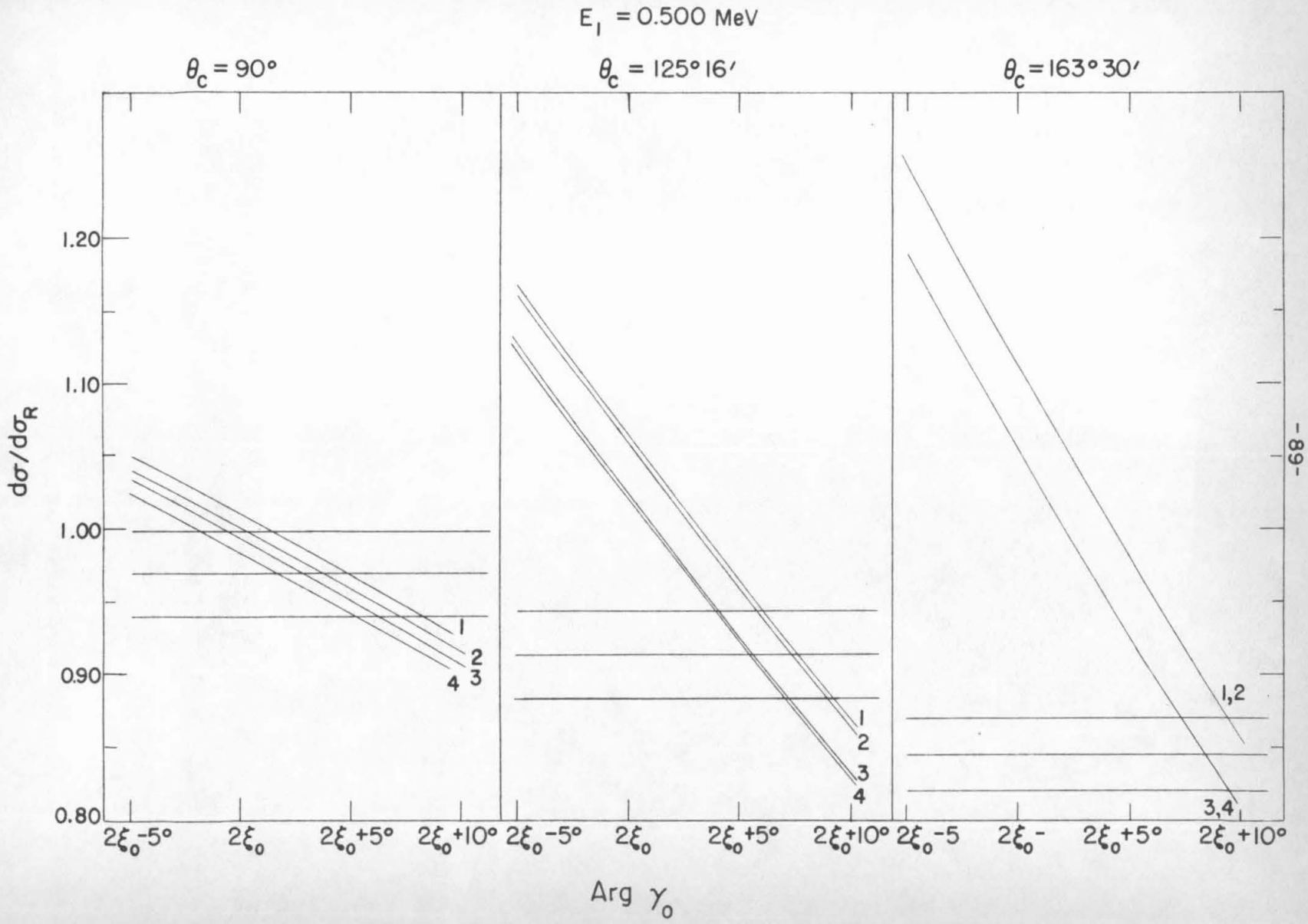
E1 = 0.500 MeV
θc = 90°
θc = 125° 16′
θc = 163° 30′
dσ/dσR
1.20
1.10
1.00
0.90
0.80
1
2
3
4
1,2
3,4
2ξ0-5°
2ξ0
2ξ0+5°
2ξ0+10°
2ξ0-
2ξ0-5
Arg γ0

Figure 25

Calculated Values of $d\sigma/d\sigma_R$
$E_1 = 0.500$ Mev

The effect on $d\sigma/d\sigma_R$ produced by varying the amplitude and phase of γ_0 is shown here. The interaction radius and reaction cross section used in calculating each curve are specified by the numerical labels. The values to which these labels correspond are

1: R = 4.90 f, σ_r = 73.4 mb
2: R = 4.90 f, σ_r = 99.6 mb
3: R = 3.70 f, σ_r = 73.6 mb
4: R = 3.70 f, σ_r = 99.6 mb

The three horizontal lines show the value of the experimental cross section and limits which lie three percent above and below it, respectively. See pp. 43 to 45 of the text.

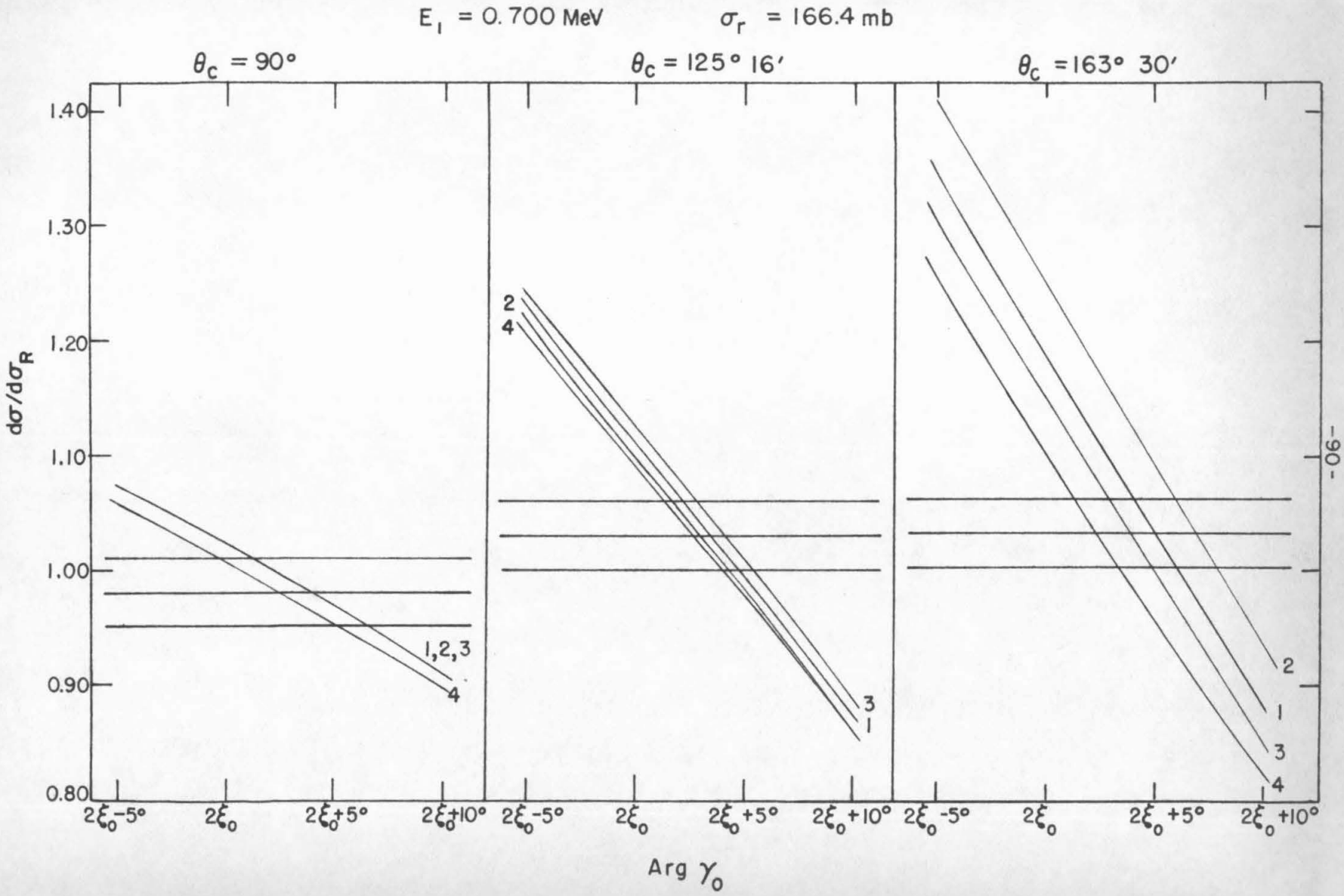
E1 = 0.700 MeV
σr = 166.4 mb
θc = 90°
θc = 125° 16′
θc = 163° 30′
dσ/dσR
1.40
1.30
1.20
1.10
1.00
0.90
0.80
1,2,3
4
2
4
3
1
2
1
3
4
2ξ0-5°
2ξ0
2ξ0+5°
2ξ0+10°
Arg γ0

Figure 26

Calculated Values of $d\sigma/d\sigma_R$
$E_1 = 0.700$ Mev, $\sigma_r = 166.4$ mb

The effect on $d\sigma/d\sigma_R$ produced by varying the phase of γ_1 and the interaction radius is shown here. The phase and interaction radius used in calculating each curve are specified by the numerical labels. The values to which these labels correspond are

1: $R = 4.10$ f, $\arg \gamma_1 = 2\xi_1$
2: $R = 4.10$ f, $\arg \gamma_1 = 2\xi_1 - 3^\circ$
3: $R = 4.10$ f, $\arg \gamma_1 = 2\xi_1 + 3^\circ$
4: $R = 3.70$ f, $\arg \gamma_1 = 2\xi_1 + 3^\circ$

The three horizontal lines show the value of the experimental cross section and limits which lie three percent above and below it, respectively. See pp. 43 to 45 of the text.

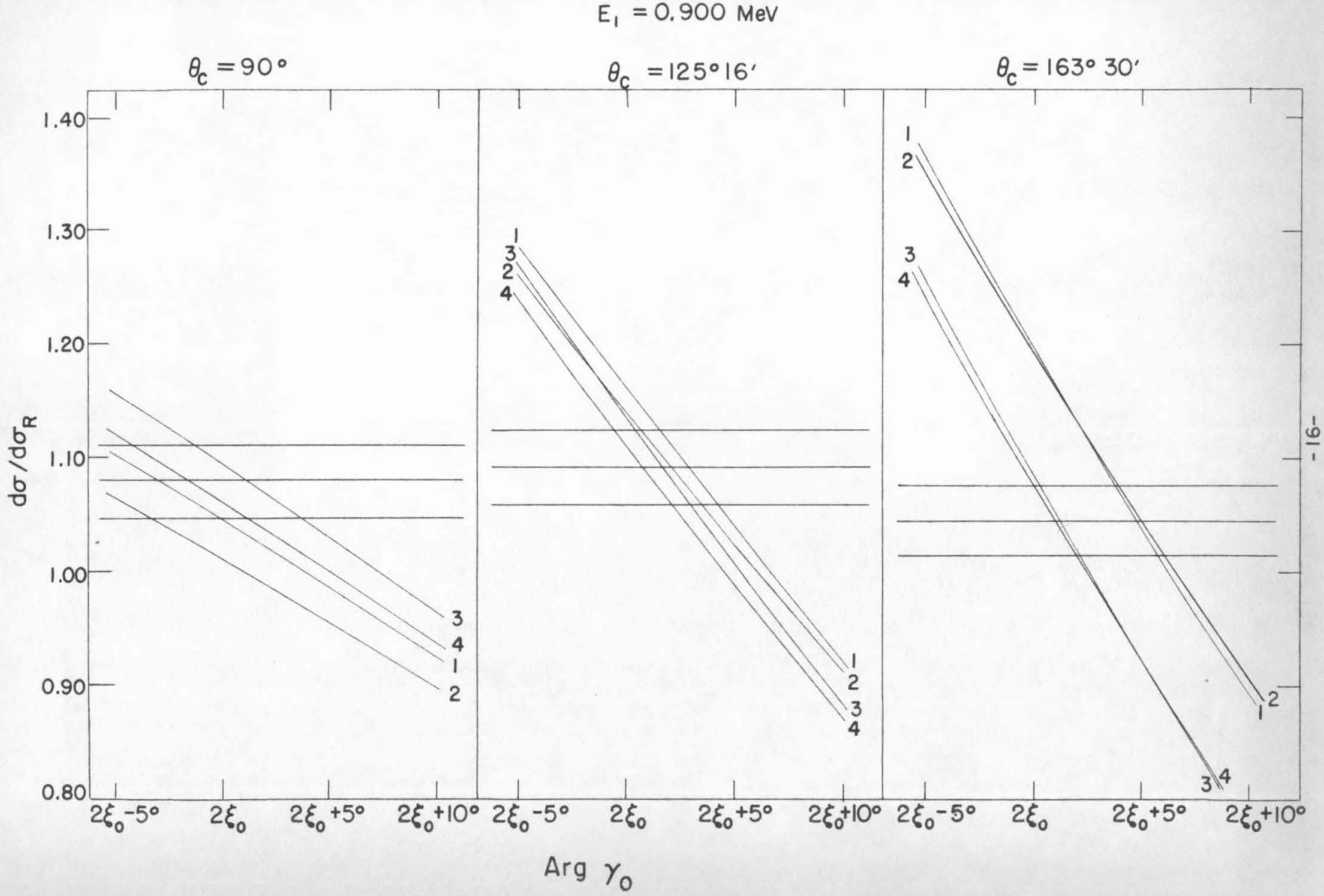
$E_1 = 0.900$ MeV
$\theta_c = 90°$
$\theta_c = 125°16'$
$\theta_c = 163°30'$
$d\sigma/d\sigma_R$
1.40
1.30
1.20
1.10
1.00
0.90
0.80
$2\xi_0 - 5°$
$2\xi_0$
$2\xi_0 + 5°$
$2\xi_0 + 10°$
Arg γ_0

Figure 27

Calculated Values of $d\sigma/d\sigma_R$
$E_1 = 0.900$ Mev, $\arg\hat{\gamma}_1 = 2\xi_1 + 2^\circ$

The effect on $d\sigma/d\sigma_R$ produced by varying the magnitudes of γ_0 and γ_1 is shown here. The magnitudes used in calculating each curve are specified by the numerical labels. The values to which these labels correspond are

1: $|\gamma_0| = 0.8343$, $|\gamma_1| = 0.97$, $\sigma_r = 258.8$ mb
2: $|\gamma_0| = 0.7856$, $|\gamma_1| = 0.97$, $\sigma_r = 300.7$ mb
3: $|\gamma_0| = 0.9008$, $|\gamma_1| = 0.95$, $\sigma_r = 258.8$ mb
4: $|\gamma_0| = 0.8562$, $|\gamma_1| = 0.95$, $\sigma_r = 300.7$ mb

The three horizontal lines show the value of the experimental cross section and limits which lie three percent above and below it, respectively.

See pp. 43 to 45 of the text.

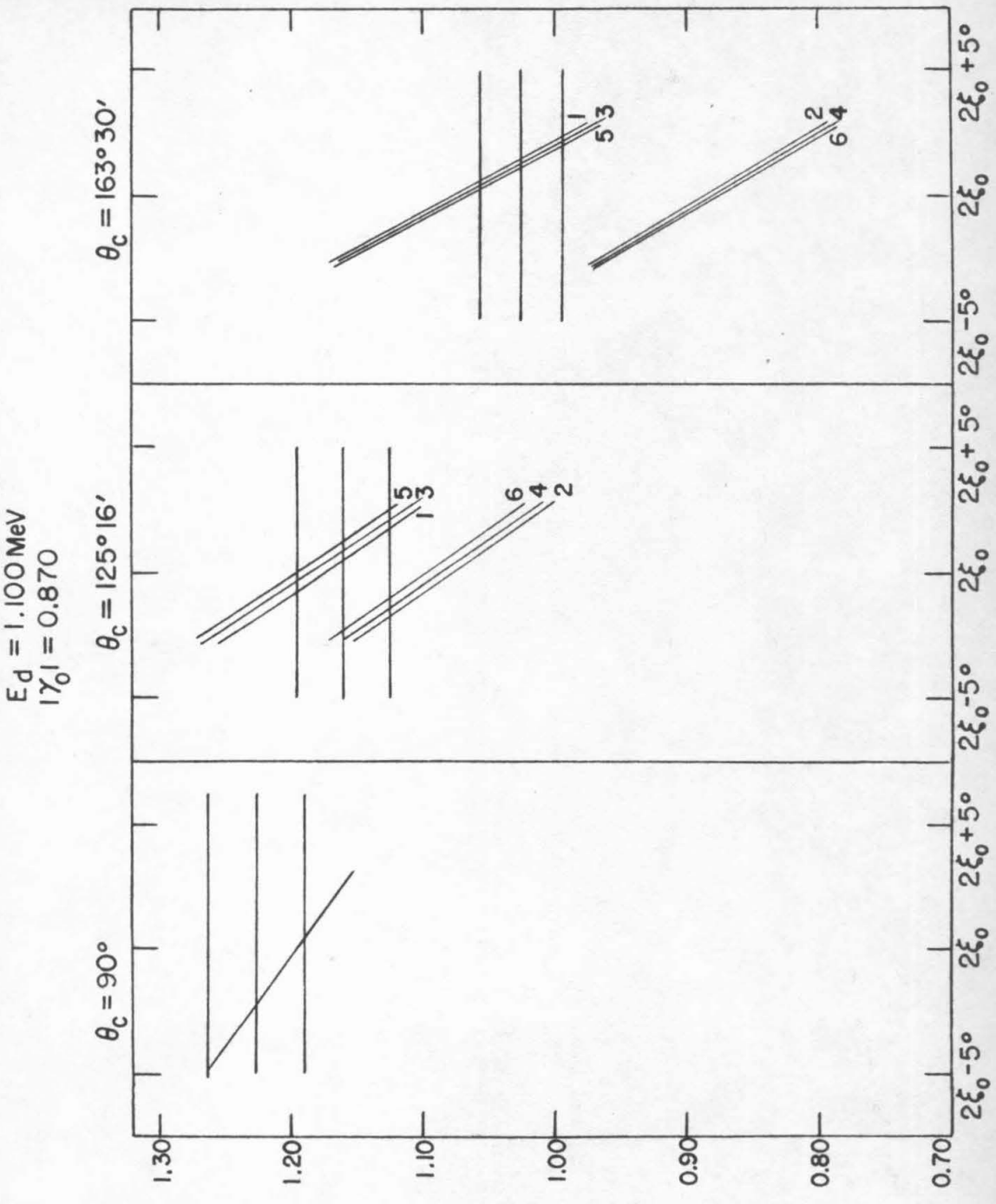
$E_d = 1.100$ MeV
$|\gamma_0| = 0.870$
$\theta_c = 90°$
$\theta_c = 125°16'$
$\theta_c = 163°30'$
$d\sigma/d\sigma_R$
1.30
1.20
1.10
1.00
0.90
0.80
0.70
$2\xi_0 - 5°$
$2\xi_0$
$2\xi_0 + 5°$
Arg γ_0
1
2
3
4
5
6

Figure 28

Calculated Values of $d\sigma/d\sigma_R$
$E_1 = 1.100$ Mev, $|\gamma_0| = 0.870$

The effect on $d\sigma/d\sigma_R$ produced by varying the amplitude and phase of γ_1 is shown here. The values of γ_1 used in calculating each curve are specified by the numerical labels. The values to which these labels correspond are

1, 3, 5: $|\gamma_1| = 0.9121$, $\sigma_r = 328.5$ mb
2, 4, 6: $|\gamma_1| = 0.8826$, $\sigma_r = 398.3$ mb

1, 2: $\arg \gamma_1 = 2\xi_1$
3, 4; $\arg \gamma_1 = 2\xi_1 + 1^\circ$
5, 6; $\arg \gamma_1 = 2\xi_1 + 2^\circ$

The three horizontal lines show the value of the experimental cross section and limits which lie three percent above and below it, respectively.

See pp. 43 to 45 of the text.

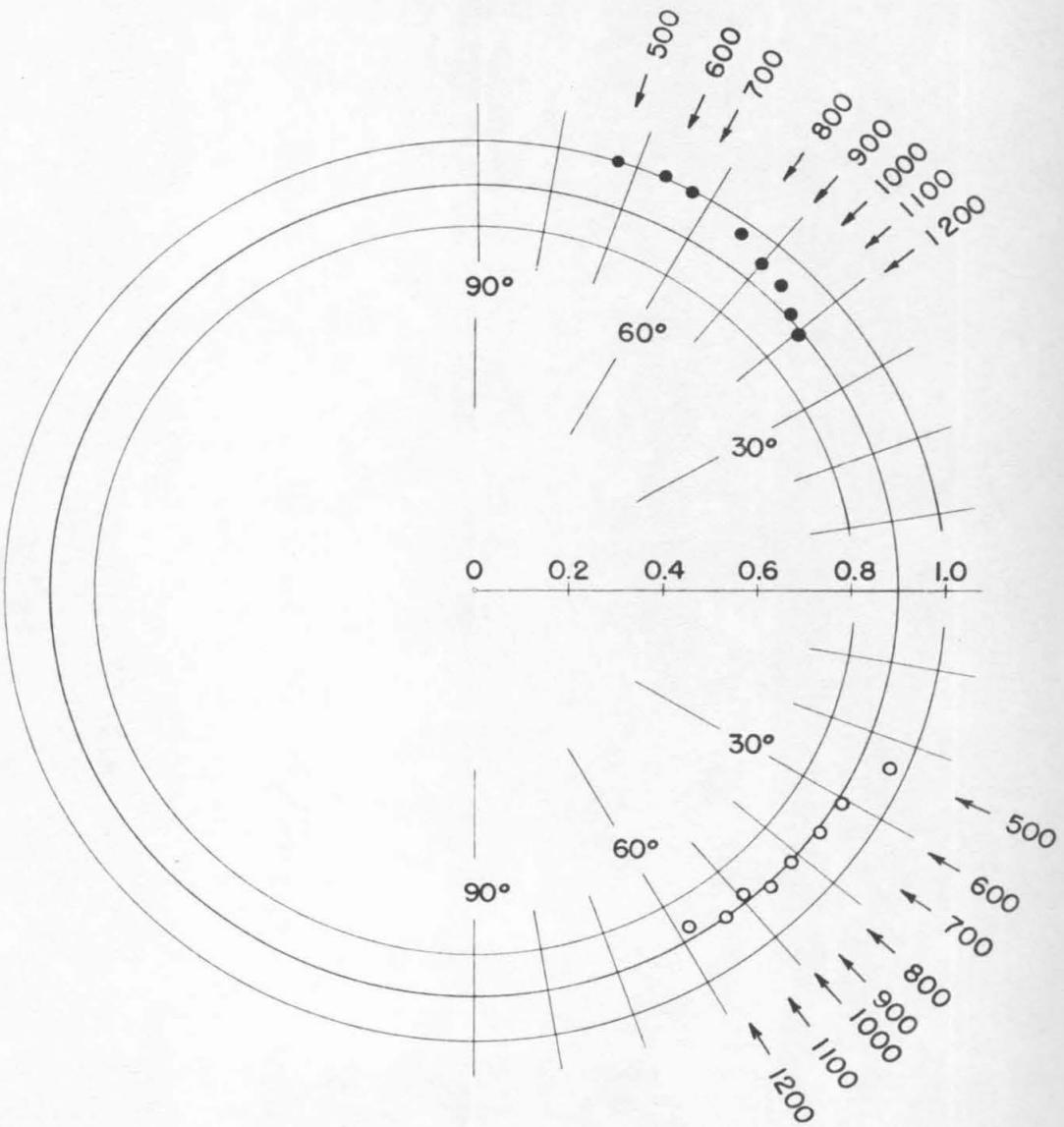
500
600
700
800
900
1000
1100
1200
90°
60°
30°
0
0.2
0.4
0.6
0.8
1.0
30°
60°
90°
500
600
700
800
900
1000
1100
1200
° γ_0
• γ_1

Figure 29

Values of γ_0 and γ_1 which Produce the Best Fit to the Experimental Cross Sections

This figure shows how the best-fit values of γ_0 and γ_1 vary as the incident-deuteron energy is changed. The numbers placed adjacent to the arrows denote the deuteron energy to which the indicated values of γ_ℓ correspond. See Table III and p. 44 of the text.